Dynamic Coronal Mass Ejection Processes and Magnetic Reconnection

---

Alshaimaa Saad Hassanin

Dissertation
zur Erlangung des akademischen Grades
"doctor rerum naturalium"
(Dr. rer. nat.)
in der Wissenschaftsdisziplin Wissenschafsdisziplin Astrophysik

eingereicht an der
Mathematisch-Naturwissenschaftlichen Fakultät
Institut für Physik und Astronomie
der Universität Potsdam

Potsam, den 08. Mai 2018

1. Hauptbetreuer: Prof. Dr. Norbert Seehafer
2. Gutachter: Prof. Dr. Gottfried Mann
3. Gutachter: Prof. Dr. Terry Forbes

Published online at the
Institutional Repository of the University of Potsdam:
URN urn:nbn:de:kobv:517-opus4-419626
http://nbn-resolving.de/urn:nbn:de:kobv:517-opus4-419626

To my coming daughter ...Hayat.

Acknowledgments

This project would not have been possible without the support of many people. Many thanks to my advisers, my husband, Reinaldo and Maria del Valle, who read my numerous revisions and helped make some sense of the confusion. Also thanks to my supervisors, who offered guidance and support. Thanks to DAAD for awarding me a Dissertation Scholarship, providing me with the financial means to commence and complete this project. And finally, thanks to my parents, my sister and numerous friends, Mona, Samah, Sergei and Franziska, who endured this long process with me, always offering support and love.

Abstract

The Sun is the nearest star to the Earth. It consists of an interior and an atmosphere. The convection zone is the outermost layer of the solar interior. A flux rope may emerge as a coherent structure from the convection zone into the solar atmosphere or be formed by magnetic reconnection in the atmosphere. A flux rope is a bundle of magnetic field lines twisting around an axis field line, creating a helical shape by which dense filament material can be supported against gravity. The flux rope is also considered as the key structure of the most energetic phenomena in the solar system, such as coronal mass ejections (CMEs) and flares. These magnetic flux ropes can produce severe geomagnetic storms. In particular, to improve the ability to forecast space weather, it is important to enrich our knowledge about the dynamic formation of flux ropes and the underlying physical mechanisms that initiate their eruption, such as a CME.

A confined eruption consists of a filament eruption and usually an associated flare, but does not evolve into a CME; rather, the moving plasma is halted in the solar corona and usually seen to fall back. The first detailed observations of a confined filament eruption were obtained on 2002 May 27 by the *TRACE* satellite in the 195 Å band. So, in the *chapter 3*, we focus on a flux rope instability model. A twisted flux rope can become unstable by entering the kink instability regime. We show that the kink instability, which occurs if the twist of a flux rope exceeds a critical value, is capable of initiating of an eruption. This model is tested against the well observed confined eruption on 2002 May 27 in a parametric magnetohydrodynamic (MHD) simulation study that comprises all phases of the event. Very good agreement with the essential observed properties is obtained, only except for a relatively poor matching of the initial filament height.

Therefore, in *chapter 4*, we submerge the center point of the flux rope deeper below the photosphere to obtain a flatter coronal rope section and a better matching with the initial height profile of the erupting

filament. This implies a more realistic inclusion of the photospheric line tying. All basic assumptions and the other parameter settings are kept the same as in *chapter 3*. This complement of the parametric study shows that the flux rope instability model can yield an even better match with the observational data. We also focus in *chapters 3* and *4* on the magnetic reconnection during the confined eruption, demonstrating that it occurs in two distinct locations and phases that correspond to the observed brightenings and changes of topology, and consider the fate of the erupting flux, which can reform a (less twisted) flux rope.

The Sun also produces series of homologous eruptions, i.e. eruptions which occur repetitively in the same active region and are of similar morphology. Therefore, in *chapter 5*, we employ the reformed flux rope as a new initial condition, to investigate the possibility of subsequent homologous eruptions. Free magnetic energy is built up by imposing motions in the bottom boundary, such as converging motions, leading to flux cancellation. We apply converging motions in the sunspot area, such that a small part of the flux from the sunspots with different polarities is transported toward the polarity inversion line (PIL) and cancels with each other. The reconnection associated with the cancellation process forms more helical magnetic flux around the reformed flux rope, which leads to a second and a third eruption. In this study, we obtain the first MHD simulation results of a homologous sequence of eruptions that show a transition from a confined to two ejective eruptions, based on the reformation of a flux rope after each eruption.

Zusammenfassung

Die Sonne ist der uns am nächsten benachbarte Stern. Sie besteht aus einem Inneren und einer Atmosphäre. Die Konvektionszone ist die äußerste Schicht des Inneren. Eine magnetische Flussröhre kann als kohärente Struktur aus der Konvektionszone in die Atmosphäre aufsteigen oder durch magnetische Rekonnexion in der Atmosphäre gebildet werden. Unter magnetischer Flussröhre wird hier ein Bündel magnetischer Feldlinien verstanden, die um eine zentrale Feldlinie herum verdrillt sind. In der entstehenden helikalen Form der Feldlinien kann dichtes Filamentmaterial gegen die Gravitation magnetisch gestützt werden. Diese Flussröhren werden auch als ein Schlüsselelement der energetischsten Erscheinungen in unserem Sonnensystem, nämlich koronaler Massenauswürfe (CMEs) und Flares, angesehen. Auf diesem Wege können solare magnetische Flussröhren starke geomagnetische Stürme erzeugen. Für Voraussagen des Raumwetters ist es von entscheidender Bedeutung, sowohl die dynamischen Prozesse der Flussröhrenbildung zu verstehen als auch die physikalischen Mechanismen, die ihrer Eruption, z.B. einem CME, zugrunde liegen.

Eine beschränkte Filamenteruption besteht aus einer Filamentaktivierung und üblicherweise einem mit ihr verbundenen Flare, wobei die Entwicklung zu einem CME jedoch ausbleibt; vielmehr wird aufsteigendes Plasma in der Korona gehalten und meist kann sein Rückfall beobachtet werden. Die ersten detaillierten Beobachtungen einer beschränkten Filamenteruption wurden am 27. Mai 2002 vom *TRACE*-Satelliten im 195Å-Band gewonnen. Zu ihrer Analyse wird in *Kapitel 3* die Instabilität einer Flussröhre untersucht. Eine verdrillte Flussröhre kann instabil gegenüber der Knick-(Kink-)Instabilität werden. Wir zeigen, dass die Knick-Instabilität, die auftritt, wenn die Verdrillung einen kritischen Wert überschreitet, eine Eruption auslösen kann. Eine parametrische magnetohydrodynamischen (MHD-) Simulation, die alle Phasen des Ereignisses umfasst, wird mit den Beobachtungen vom 27. Mai 2002 verglichen. Hinsichtlich der wesentlichen

Eigenschaften wird eine sehr gute Übereinstimmung der Simulationsergebnisse mit den Beobachtungen festgestellt, allerdings mit Ausnahme der Anfangshöhe des Filamentes.

Deshalb wird in *Kapitel 4* das Zentrum der Flussröhre tiefer unterhalb das Niveau der Photosphäre gelegt. Das führt zu einem flacheren koronalen Flussröhren-Abschnitt und einer realistischeren Modellierung der Feldlinienverankerung in der Photosphäre. Diese komplementäre parametrische Untersuchung zeigt eine noch bessere Übereinstimmung mit den Beobachtungen.

In den *Kapiteln 3* und *4* liegt ein spezielles Augenmerk auch auf der magnetischen Rekonnexion im Verlaufe der beschränkten Eruption. Es stellt sich heraus, dass die Rekonnexion an zwei unterschiedlichen Orten und in zwei unterschiedlichen Phasen stattfindet, die durch verstärkte Strahlungsemission und Änderung der magnetischen Topologie charakterisiert sind. In den späten Stadien der Entwicklung kommt es zur Neubildung einer (weniger verdrillten) Flussröhre.

Die Sonne produziert auch Serien homologer Eruptionen, die wiederholt mit ähnlicher Morphologie in derselben aktiven Region auftreten. In *Kapitel 5* wird die neu gebildete Flussröhre als neue Anfangsbedingung verwendet, um die Möglichkeit nachfolgender homologer Eruptionen zu untersuchen. Photosphärische Bewegungen speisen Energie in das Magnetfeld ein. Wir verwenden konvergierende Bewegungen, die die Flüsse von Flecken unterschiedlicher Polarität zur Inversionslinie der Polarität transportieren und dort teilweise neutralisieren. Die damit verbundene Rekonnexion erzeugt helikalen magnetischen Fluss um die neu gebildete Flussröhre herum, was zu einer zweiten und einer dritten Eruption führt. Unsere Simulationen einer Serie homologer Eruptionen zeigen erstmals einen Übergang von einer beschränkten Eruption zu zwei ejektiven Eruptionen.

Contents

List of Tables

List of Figures

List of Abbreviations

3D	Three-Dimensional
AR	Active Region.
CFL	Courant-Friedrichs-Levy criterion
CME	Coronal Mass Ejection.
HK16	Hassanin & Kliem 2016
HKS16	Hassanin et al. 2016
MHD	Magnetohydrodynamics
PIL	Polarity Inversion Line = Neutral Line
TD99	Titov & Démoulin 1999
TK03	Török & Kliem 2003
TK05	Török & Kliem 2005

CHAPTER 1

Introduction to the Solar Structure, Activity, Magnetic Field and Modelling

1.1 The Sun

The Sun has mostly been envisioned as tremendous source of power and strength. Following the history from the dawn of the humankind, the Sun has being worshiped across many cultures such as Egyptian, Indo-European, and Meso-American. As direct acknowledgement of its importance, the Sun took a great significance in the religion in ancient Egypt, especially in the status of Pharaoh. Many of the temples on the Karnak site in Egypt, depict Pharaoh with the sun on his head, Ra, the Sun God.

Even in the modern times, our mother star still has some spiritual significance; indeed we consider sunny days as "good weather" and other days when it is cloudy as "bad weather" Furthermore, solar activity has many influences on the shape of our environment of space weather, such as global communication, navigation networks, satellites and commercial power systems.

The Sun is the nearest star to the Earth. This enables us to study comprehensively the different solar eruptive phenomena. In this chapter, we introduce an essential information about the solar structure which is followed by a brief description of the solar activity with all its resulting phenomena.

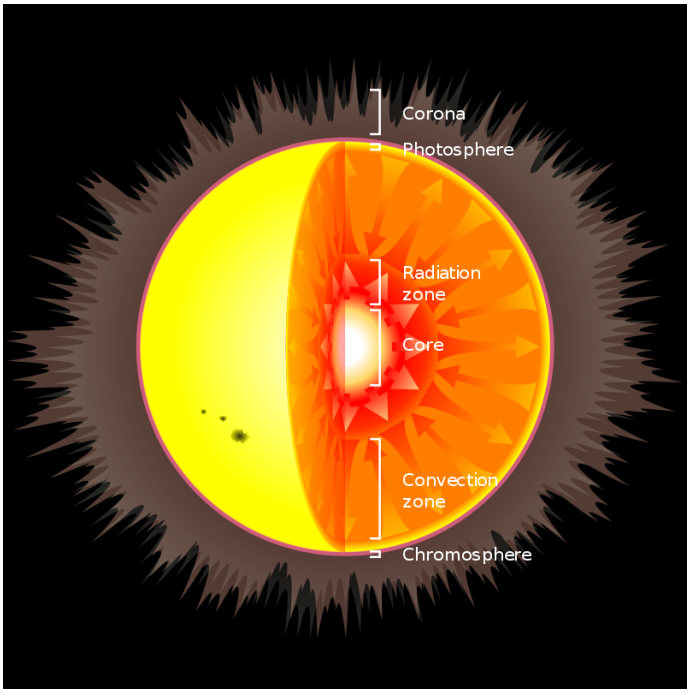

Figure 1.1: A cartoon image of the solar structure. Image credit: www.wikibooks.org

1.2 Solar Interior

The Sun is in the middle stage of a main sequence star with an age of 4.6 billion years (Houdek and Gough, 2011) . It is a G2V spectral type star with an absolute magnitude of 4.8. The mass of the Sun is 2×10^{30} kg and it is composited of 75% hydrogen, 24% helium and 1% heavier elements. The Sun does not have a tangible boundaries, however the dominant energy transfer process characterizes the different layers in the Sun. The solar interior consists of the core, radiative zone and the convection zone. Within the innermost part of the Sun, the solar core, the energy is generated via nuclear fusion by conversion of Hydrogen to Helium. About 9.2×10^{37} times per second, the proton-proton chain dominates in the Sun and generates 3.8×10^{26} Js^{-1}. The core has a density of ~ 150 g cm^{-3} and a temperature of 1.5×10^7 K. From the solar center to roughly 0.25 of the solar radius, $R_\odot$, extends the solar core.

The radiative zone locates above the solar core, extends out to ~ 0.7 $R_\odot$ and has temperature of $2 - 7 \times 10^6$ K and a density of $0.2 - 20$ g cm^{-3}. As it is indicated from the name of the zone, the radiative transfer is the dominate energy transfer mechanism in this zone. The energy released in the core travels extremely slowly through the radiative zone. Photons can take long periods of time as 50×10^6 years to travel through the radiative zone. At the outer edge of the radiative zone, the temperature gradient becomes sufficiently high to allow convection to set in in the next zone.

The convection zone is the outermost layer of the solar interior, which surrounds the radiative zone. The convection mechanism is the dominant heat-transfer process in this zone. The radiative zone heats the higher-lying material and causes this material to be less dense than its surrounding, rising up, moving horizontally, cooling at the surface, becoming more dense and sinking. These bulk fluid motions create circular convection currents and cause the granulations and the super-granulations of the solar surface. Between the radiative and convection zone, there is a transitional region with a strong radial shear known as the tachocline. This large shear occurs due to the sudden change in the rotation rate between these two zones, as the solar rotational rate in the radiative zone is higher than that of the convection zone. The Sun rotates with a differential rotation which depends on the solar latitude and depth. The solar rotation varies between about 25 days at the equatorial regions and 35 days at the polar regions. (For more detailed information, see Howe (2009)). These first three layers represent the Solar Interior. The next three layers represent the Sun's atmosphere. These solar layers can be divided like the shells of an onion as illustrated in Figure 1.1.

1.3 Solar Atmosphere

Approaching the top of the convection zone, the density quickly falls to about 0.016 g cm^{-3} with effective temperature $T_{eff} = 5777$ K. At this layer, which is called the photosphere and the solar surface, the light can escape by radiation out into space. The photosphere is defined visually to us, although it measures only a few hundred km, ~ 500 km. The temperature first declines further to reach its minimum of ~ 4000 K in the lower chromosphere and then starts to increase again by reaching the top of the chromosphere and the thin transition zone between the chromosphere and the corona.

The temperature rises from ~ 4000 K to reach ~ 20000 K at the top of the chromosphere. The density varies from 10^{-10} g cm^{-3} at the bottom of the chromosphere to 10^{-13} g cm^{-3} at the top. The chromosphere is a diffuse region that can be seen as red flashes during a total solar eclipse. In addition, the $H\alpha$ filter reveals easily the structure of the chromosphere.

Above the chromosphere and further outward, we approach the corona where the temperature rises drastically to reach more than $\sim 10^6$ K. The corona is characterized by very low density of 10^{-15} g cm^{-3}. Therefore it is only visible at the time of a solar eclipse. It is still not totally understood why the temperature increases so much in the corona, especially as it is far from the core, the heat producer. Researchers assume that the ever-changing solar magnetic field is the key which provides many clues about this dramatic increase in temperature. The material making up the solar atmosphere streams out in the form of energetic and

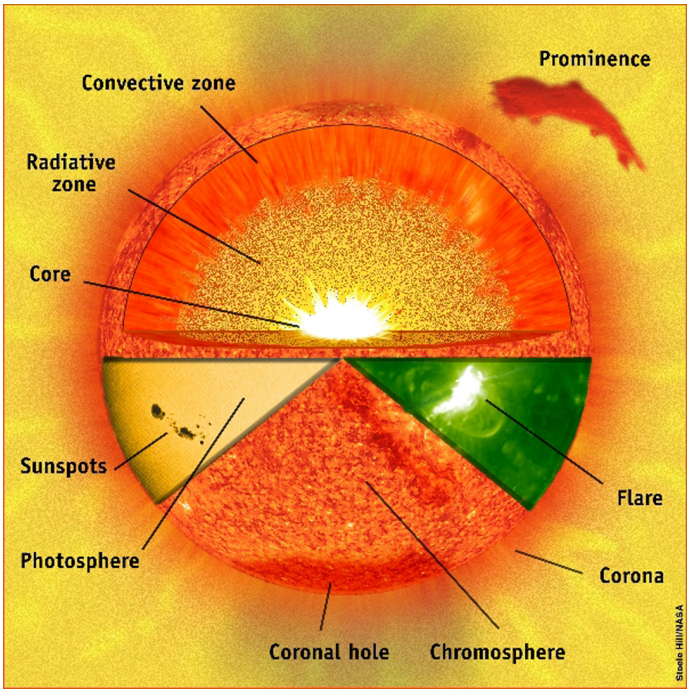

Figure 1.2: The image gives a basic overview of the solar structure with the solar activity features. The surface features (flare, sunspots and photosphere, chromosphere, and the prominence) are all taken from actual SOHO images of the Sun. Image Credit: ESA & NASA/ SOHO

magnetized particles, escaping from the Sun as a solar wind. The solar wind reaches beyond all planets of the solar system, until it creates a shock with the interstellar medium and defines the outer boundary to the solar system. The region which is dominated by the solar wind, is called the heliosphere.

For more detailed introduction about the Solar Structure, we refer to Priest (1984); Stix (2002); Mullan (2010).

1.4 Solar Activity

Solar activity rises and falls with a cyclical behavior that has an influence on our modern life in many ways. The most spectacular phenomena forming (collectively) the solar activity, which are driven by the solar magnetic field, are the sunspots, the filaments/prominences, the flares, the coronal holes, the solar wind and the coronal mass ejections (CMEs).

1.4.1 Sunspots and Active Regions

The most obvious evidence of the existence of solar magnetic field is the sunspots. Sunspots are temporary phenomena. They locate on the surface of the Sun (the photosphere) as a result of magnetic activity. The

sunspot consists of a dark spot "umbra" surrounded by "penumbra", a less dark region. The darker the umbra, the lower the temperature, and the stronger the solar magnetic field. Sunspots often appear as a pair, or in a group. The sunspot numbers decrease and increase in a nearly cyclical behavior. When the number of the spots is small (or zero), the Sun is said to be in a stage of "minimum" activity. The Sun is at "maximum" activity, when there are large numbers of spots in its surface. Sunspot activity cycles are about every eleven years. The interval can be as short as nine years, and as long as twelve years.

At the solar minimum, the Sun may be almost spotless. Then spots start to appear at latitudes around 30 deg. Early in the cycle, sunspots emerge at relativity high latitudes and then move towards the equator (Spörer's law). Sunspot mostly comes in a pair with opposite magnetic polarity. The first spot to be seen is a leader spot and will be followed by a follower spot. The leader is situated closer to the equator and has the same polarity as the hemisphere it appeared in, while the follower is situated at higher latitude with an opposite polarity (Hale's polarity law). From cycle to cycle, the polarities of the leader and the follower sunspots (with respect to the solar rotation) change from north/south to south/north and back. The distinguishing feature of the bipolar structure of a sunspot pair with opposite magnetic polarities is due to the source freeness of the magnetic field. This leads the magnetic flux to appear in the form of loops as shown in Figure 1.2. However, such a structure is not always required, and if the flux of only one polarity is sufficiently concentrated, then a single "unipolar" spot can be seen.

The lifetime is roughly proportional to the area of the spot. Most spots break up into smaller units at some points, and will then decay. The sunspot lifetime ranges from less than an hour to many days. In the chromosphere, sunspots are found to be surrounded by plages. Plages are regions of enhanced emission. Now, an active region (AR) can be defined as a region that has sunspots and plages. The systematic behavior of bipolar sunspot groups can be explained in terms of a toroidal magnetic field $\mathbf{B}_t$. "Toroidal" refers to the magnetic field lines that form loops around the solar rotation axis. This toroidal field forms concentrated flux tubes and these tubes may be driven through the photosphere from the tachocline by the convection that results from magnetic buoyancy. In the photosphere they form bipolar sunspot groups.

1.4.2 Quiet Sun

Quiet Sun is the remaining atmosphere other than active regions and coronal holes. It consists of the parts of the corona that had low activity and no sunspots. Filaments/Prominences exist there and may also be erupted. However, the eruptions there are typically slower, and less energetic but are due to the same physical processes as in active regions.

1.4.3 Solar Wind

The large-scale corona is governed by magnetohydrodynamics. The expansion of the coronal material occurs as a process of motion from the high pressure (at the base of the corona) to the low pressure (in the interplanetary medium). The expansion ejects this bulk coronal material outward from the Sun. This outflow forms what is known as the Solar Wind. A constant stream of plasma (electrons, ions, and protons) flows from the solar corona, with a temperature of about a million degrees and with a velocity exceeding 450 Kms^{-1} .

1.4.4 Filaments/Prominences

Filaments are large structures which contain cool and dense chromospheric plasma and are suspended above the solar surface against solar gravity in magnetic loops. Kippenhahn and Schlüter (1957) gave the first theoretical description with details about the filaments. The filament is aligned along the neutral line. The magnetic field appears to play a significant role in the filament's existence as well as its stability. The filament is supported by magnetic arcs connecting opposite polarities in the solar photosphere. The magnetic field lines do not form perfect arcades. Magnetic tension pulls down the filaments which in turn pull down the frozen-in magnetic field lines. The Magnetic pressure causes a force in the opposite direction of the magnetic tension, thus the filament is being at a certain height by the equilibrium between the magnetic pressure and the magnetic tension. The filaments can be "quiescent" i.e., stationary for hours or days (Martin, 1998). Filaments appear dark when are observed on the solar disk, as they are cooler than the hot photosphere below. But if they appear on the solar edge, they appear brighter against the dark empty space background, and then we call them "prominences". Prominences/Filaments material can burst upward rapidly, after experiences a kind of instability.

1.4.5 Solar Flares

One of the most spectacular phenomena on the Sun that is associated with explosive events is called solar flare as shown in Figure 1.2. Despite sunspots are indirect clues about underlying dynamic physics, flares are actual events with definite timing which can be observed in all active regions, at often every wavelength of the electromagnetic spectrum. This process takes place especially in regions where sunspots with opposite polarities are in close spatial contact. As a result of the rooted magnetic field lines in the photosphere where convective motions are ubiquitous, flares will be found in these active regions. At the footpoints of a magnetic loop, the field lines can be pushed by the convection process in complicated ways, with twisting and stretching. These complex motions cause stresses to build up on the field lines. The stressed magnetic

field attempts to find an equilibrium configuration which serves as a reservoir in which free magnetic energy is stored. As long as this equilibrium does not pass over the threshold of an instability, the buildup of free energy can continue. At certain times and places, a trigger comes into an operation, and this leads to instability, where the stored free energy quickly appears as a flare phenomenon. Based on a logarithmic classification system, solar flares are categorized as X-class, the strongest, and in decreasing order M- , C-, B-, A-class. In the larger context of the Sun as a whole, flares represent only a small significant disruption. The energy released in even the largest flares contributes only small portion to the solar energy budget.

1.4.6 Coronal Mass Ejections

Coronal mass ejections (CMEs) are violent phenomena. They are considered as the primary cause of the largest and most damaging space weather disturbances (Gosling, 1993; Webb et al., 2000). "A CME" term is used as an indication of the process that leads to the ejection of mass and magnetic flux from the lower corona into interplanetary space. They propagate out through the solar wind. This propagation has an influence on the CME and its geoeffectiness but this is outside of the scope of this thesis. The CMEs occur when the balance of two opposite forces that maintains equilibrium is disturbed. Something causes the upward force to become dominant over downward one and erupt the filament upward. The typical morphology for the CMEs is a so-called three-part structure, consisting of an outer leading edge, an embedded bright core, and the cavity in between (Illing and Hundhausen, 1985; Forbes, 2000). It is generally accepted that the bright core of the CMEs corresponds to dense filament plasma, which is supported by an erupting magnetic flux rope prior the eruptions (House et al., 1981; Dere et al., 1999). Nearly every CME (except a few solar slow ones originating in the quiet Sun) is accompanied by a flare.

1.4.7 Confined (Failed) Eruption

Confined eruption is a case in which the filament undergoes instability and rises to reach a terminal height where the erupting filament halts and then the filament material slides back to the solar surface (Ji et al., 2003) without showing any evidence of a CME. The suggestions for the possible causes of the failed eruption are: an insufficient free magnetic energy to energize the filament to erupt as a successful eruption (Shen et al., 2012) and the confinement by the overlying magnetic field (Hassanin and Kliem, 2016; Hassanin et al., 2016).

1.5 Solar Magnetic Field and Basics of the MHD

The Sun has a changing and strong magnetic field which is generated at the tachocline (Dynamo Theory). The polarity of the poles is reversed periodically every 9-11 years near the maximum of the sunspot cycle. The solar magnetic cycle has a period of about 22 years for the pole to return to the same magnetic polarity. The magnetic fields of 6-12 Gauss exist at the poles of the Sun and extend far out the interplanetary space, and represent the global dipole moment of the solar magnetic field. According to Hale's polarity law, the leading spot has typically the same polarity as the pole in the same hemisphere in the first half of the cycle. However, this is not the whole story.

The Sun is made of plasma which is the most common state of matter in the Universe. Plasma is usually described as a quasi-electrically-neutral matter, composed of positively and negatively charged particles which exhibits collective behavior. The magnetic field can exert forces on such electrically conducting media. The mutual interaction between a moving fluid (macroscopic single fluid) and a magnetic field is described by Magnetohydrodynamics (MHD). In this chapter we will touch on a few important topics in the field of solar magnetohydrodynamic and how these topics are very useful in describing the solar activity. Our knowledge about the behavior of the solar complex magnetic fields inside electrically conducting fluids, can help us to better understand the nature of the solar activity.

1.5.1 MHD Equations

We compile in this section the MHD equations to determine the macroscopic observables of a conducting fluid; by combining the hydrodynamic mechanics equations and Maxwell's equations. Maxwell's equations describe the electric and magnetic fields arising as a result from varying distributions of electric charge density ρ and electric currents density $\boldsymbol{J}$, and how those fields change with respect of the time. The MHD equations are written here in S.I. units (based on meter-kilogram-second (MKS) system).

First, Maxwell's equations consist of :

$$\boldsymbol{\nabla} \times \boldsymbol{E} = -\frac{\partial \boldsymbol{B}}{\partial t}\,, \quad \text{Faraday's law} \tag{1.1}$$

$$\boldsymbol{\nabla} \cdot \boldsymbol{E} = \frac{\rho}{\epsilon_0}\,, \quad \text{Gauss' law for an electric field} \tag{1.2}$$

$$\boldsymbol{\nabla} \cdot \boldsymbol{B} = 0\,, \quad \text{Gauss' law for a magnetic field (Divergence free condition)} \tag{1.3}$$

$$\boldsymbol{\nabla} \times \boldsymbol{B} = \mu_0 \boldsymbol{J} + \mu_0 \epsilon_0 \frac{\partial \boldsymbol{E}}{\partial t} \quad \text{Ampere's law with Maxwell correction} \tag{1.4}$$

where $\boldsymbol{E}$ and $\boldsymbol{B}$ are the electric and magnetic field vectors, ϵ_0 is the permittivity of free space, μ_0 is the magnetic permeability and the speed of light in a vacuum is $c = \sqrt{(\epsilon_0 \mu_0)}$.
The continuity equation, which expresses the conservation of mass density, is:

$$\frac{\partial \rho}{\partial t} + \boldsymbol{\nabla} \cdot \rho \boldsymbol{u} = 0 \tag{1.5}$$

The momentum balance describes the evolution of the velocity field. When the fluid element is subject to a pressure gradient $\boldsymbol{\nabla} p$, gravitational force $\rho \boldsymbol{g}$, and electromagnetic force $\boldsymbol{J} \times \boldsymbol{B}$, the equation of motion (momentum equation) is

$$\rho \frac{D\boldsymbol{u}}{Dt} = -\boldsymbol{\nabla} p + \rho \boldsymbol{g} + \boldsymbol{J} \times \boldsymbol{B} \tag{1.6}$$

where the differential operator $\frac{D}{Dt}$ is the total derivative that includes both the space and the time partial derivatives. In Euler's notation, we have

$$\frac{D}{Dt} = \frac{\partial}{\partial t} + (\boldsymbol{u} \cdot \boldsymbol{\nabla}) \tag{1.7}$$

Thus equation (1.6) is written as

$$\rho(\frac{\partial \boldsymbol{u}}{\partial t} + (\boldsymbol{u} \cdot \boldsymbol{\nabla})\boldsymbol{u}) = -\boldsymbol{\nabla} p + \rho \boldsymbol{g} + \boldsymbol{J} \times \boldsymbol{B} \tag{1.8}$$

According to Ohm's law, in a resistive medium, the current density $\boldsymbol{J}$ which flows in response to an electric field, is proportional to that field. The constant of proportionality is determined by how effective the plasma is at conducting the current flow. In terms of $\boldsymbol{J}$, Ohm's law for resistive MHD:

$$\boldsymbol{E} + \boldsymbol{u} \times \boldsymbol{B} = \frac{\boldsymbol{J}}{\sigma} \tag{1.9}$$

where σ is the electrical conductivity.
In MHD, the following conditions are required for plasma to be described as a macroscopic single fluid:

- Characteristic time $\gg$ ion gyroperiod and mean collision time.
- Characteristic scale $\gg$ ion gyroraduis and mean free path length.
- Plasma velocities are not relativistic.

The Induction Equation

In the limit of non-relativistic velocities and in sufficient large length-scale,

$$\frac{|\partial_t \boldsymbol{E}|}{c|\boldsymbol{\nabla} \times \boldsymbol{B}|} \sim \frac{V^2}{c^2} \ll 1\,, \tag{1.10}$$

we can neglect the displacement current in Ampere's law and (1.4) can be written as

$$\boldsymbol{\nabla} \times \boldsymbol{B} = \mu_0 \boldsymbol{J} \tag{1.11}$$

Substituting Eqs. (1.11) and (1.9) into Faraday's law (1.1), we find

$$\frac{\partial \boldsymbol{B}}{\partial t} = -\boldsymbol{\nabla} \times (\frac{\boldsymbol{J}}{\sigma} - \boldsymbol{u} \times \boldsymbol{B}) = -\boldsymbol{\nabla} \times [\frac{1}{\mu_0 \sigma}(\boldsymbol{\nabla} \times \boldsymbol{B}) - \boldsymbol{u} \times \boldsymbol{B}] \tag{1.12}$$

and the induction equation of the magnetic field for uniform η_m is obtained as

$$\frac{\partial \boldsymbol{B}}{\partial t} = \boldsymbol{\nabla} \times (\boldsymbol{u} \times \boldsymbol{B}) + \eta_m \nabla^2 \boldsymbol{B} \tag{1.13}$$

where $\eta_m = \frac{1}{\mu_0 \sigma}$ is the magnetic diffusivity, the first part in the RHS represents the convective term, and the second part represents the diffusion of the magnetic vector. The ratio between these two terms is known as the *magnetic Reynolds number*:

$$R_m = \frac{|\boldsymbol{\nabla} \times (\boldsymbol{u} \times \boldsymbol{B})|}{|\eta_m \nabla^2 \boldsymbol{B}|} \sim \frac{VB}{L} \frac{L^2}{\eta_m B} = \frac{VL}{\eta_m} \tag{1.14}$$

where V is the characteristic velocity and L is the characteristic length-scale. A related parameter is the *Lundquist Number*,

$$S = \frac{L v_A}{\eta_m} \tag{1.15}$$

where v_A is the Alfvèn velocity which is the typical velocity to which magnetic forces can accelerate plasma:

$$v_A = \frac{B}{(\mu_o \rho)^{\frac{1}{2}}} \tag{1.16}$$

For some locations, R_m may be reduced due to abnormally enhanced resistivity and turbulence. Typically,

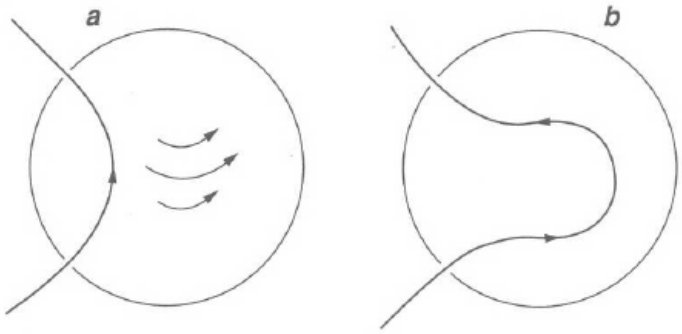

Figure 1.3: The production of toroidal field from the poloidal field due to differential rotation in the convection zone (Ω-effect). Image credit: public domain.

for astrophysical system where the length scale is very large; $R_m \gg 1$. Also for a perfectly conductive medium, $\eta_m \to 0$ is very small and thus $R_m \to \infty$, the diffusion term can be neglected and we obtain the evolution of the magnetic field in the *ideal* MHD approximation:

$$\frac{\partial \boldsymbol{B}}{\partial t} = \boldsymbol{\nabla} \times (\boldsymbol{u} \times \boldsymbol{B}) \tag{1.17}$$

In this limit, the magnetic field is said to be frozen into the fluid (Alfvèn's theorem of flux-freezing).

One consequence of the flux-freezing theorem is the Ω-effect for the solar global magnetic field, by which the differential rotation transforms poloidal flux into toroidal flux as shown in Figure 1.3. An Another consequence is that the frozen-in theorem prohibits reconnection of the magnetic field lines.

Reconnection

Magnetic reconnection describes the change of the magnetic topology, where the magnetic field lines find new connections, e.g. change between closed and open configurations. This can allow a volume of plasma mass which was previously trapped (on closed field lines) to escape from the Sun into interplanetary space. The magnetic field relaxes to a lower energy state and releases the difference in magnetic energy by reconnection into kinetic and thermal energy, including particle acceleration. According to the Sweet-Parker mechanism, reconnection occurs when two regions of magnetic field, with opposite directed field lines, approach each other towards a magnetic null sheet or current sheet. Figure 1.4 shows that the compression of these two opposite motions create a thin current sheet where the ideal MHD breaks down and the reconnection occurs, splitting the two opposite magnetic lines and reattaching them to one another.

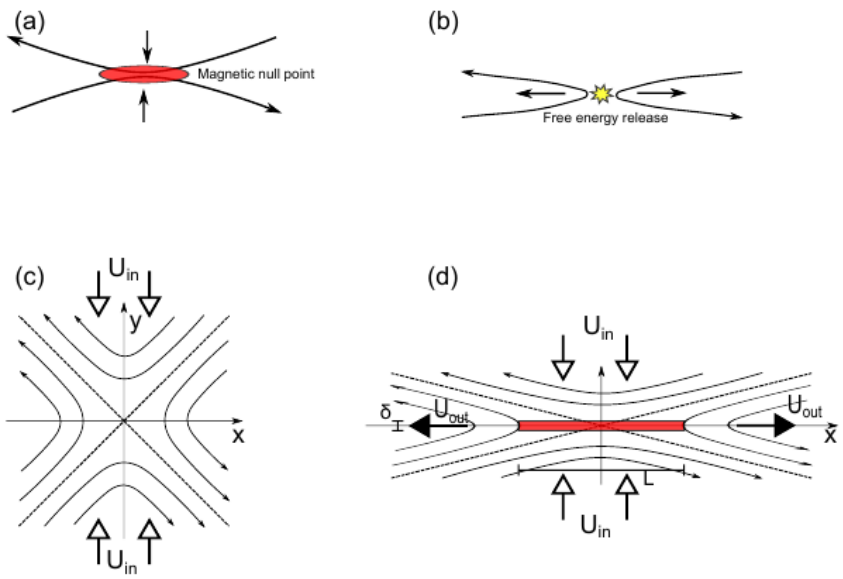

Figure 1.4: Cartoons sketching reconnection. (a) Two antiparallel field lines flow inwards towards a magnetic null point. (b) Outflow from the null point perpendicular to the direction of the inflows, associated with a release of magnetic energy. (c) Flows of dragged magnetic field lines in plasma with U_{in} towards a magnetic null. (d) The compression of antiparallel magnetic forces creates a thin current sheet (red) where non-ideal MHD reconnection behavior occurs, creating outward flows with U_{out}. Image credit: public domain.

Ideal MHD Equilibrium

Under the condition of static equilibrium and negligible gravity, the balance of forces which describes the equilibrium in the sunspots, filaments and other solar features, is written as

$$-\boldsymbol{\nabla} p + \boldsymbol{J} \times \boldsymbol{B} \quad = \quad -\boldsymbol{\nabla} p + \frac{1}{\mu_0}(\boldsymbol{\nabla} \times \boldsymbol{B} \times \boldsymbol{B}) = 0 \tag{1.18}$$

where $\boldsymbol{F_L} = \boldsymbol{J} \times \boldsymbol{B}$ is the Lorentz force which is exerted on a fluid element carring a current $\boldsymbol{J}$ in a magnetic field. By using a vector identity,

$$\boldsymbol{F_L} = \boldsymbol{J} \times \boldsymbol{B} \quad = \quad -\boldsymbol{\nabla}(\frac{B^2}{2\mu_0}) + \frac{1}{\mu_0}(\boldsymbol{B} \cdot \boldsymbol{\nabla})\boldsymbol{B} \tag{1.19}$$

Adding the above equation, (1.18) can be re-written as

$$\underbrace{-\boldsymbol{\nabla}(p + \frac{B^2}{2\mu_0})}_{\text{Gradient of total pressure}} + \underbrace{\frac{1}{\mu_0}(\boldsymbol{B} \cdot \boldsymbol{\nabla})\boldsymbol{B}}_{\text{Magnetic tension}} = 0 \tag{1.20}$$

where the total gradient of the pressure can be divided into the plasma and magnetic pressure gradients.

The ratio between these two pressure gradient is known as β-parameter (or plasma parameter):

$$\beta = \frac{2\mu_0 P_{\text{plasma}}}{B^2} \tag{1.21}$$

1⃝ Within the solar interior, in the photosphere and in the solar wind $\mapsto \underline{\beta \geq 1}$, $\mapsto$ plasma is called "warm". The plasma dominates the motion.	2⃝ In the low corona of active regions, $\mapsto \underline{\beta \ll 1}$, $\mapsto$ plasma is called "cold". Magnetic field dominates so that plasma pressure is negligible

- When the plasma is dominated by the magnetic fields, this goes to the second case where the thermal pressure is negligible. This is the case for *force-free equilibrium*, where the force balance can be approximate as:

$$\boldsymbol{F_L} = \underbrace{-\boldsymbol{\nabla}(\frac{B^2}{2\mu_0})}_{\text{Magnetic Pressure}} + \underbrace{\frac{(\boldsymbol{B}\cdot\boldsymbol{\nabla})B}{\mu_0}}_{\text{Magnetic Tension}} = 0 \tag{1.22}$$

  - The first term in this equation represents the magnetic pressure gradient, which contributes if there is inhomogeneity of magnetic field.
  - The second part represents the magnetic tension of the field, which increases with the curvature of the field lines. This part can be rewritten as

$$\boldsymbol{T_B} = \frac{(\boldsymbol{B}\cdot\boldsymbol{\nabla})B}{\mu_0} = \frac{B}{\mu_0}\frac{d(B\hat{\boldsymbol{s}})}{ds} = \frac{d}{ds}(\frac{B^2}{2\mu_0})\hat{\boldsymbol{s}} + \frac{B^2}{\mu_0}\frac{d\hat{\boldsymbol{s}}}{ds} = \boldsymbol{\nabla}_{\shortparallel}(\frac{B^2}{2\mu_0}) + \frac{B^2}{\mu_0}\frac{\hat{\boldsymbol{n}}}{R_{curv}} \tag{1.23}$$

where $\hat{\boldsymbol{s}}$ is the unit vector along $\boldsymbol{B}$, $\hat{\boldsymbol{n}}$ is the unit vector normal to the field line (i.e. $\hat{\boldsymbol{n}} \perp \hat{\boldsymbol{s}}$) and R_{curv} is the curvature raduis of the field line. Substituting the above equation into (1.22), we get

$$\boldsymbol{F_L} == \boldsymbol{\nabla}_{\shortparallel}(\frac{B^2}{2\mu_0}) + \frac{B^2}{\mu_0}\frac{\hat{\boldsymbol{n}}}{R_{curv}} - \boldsymbol{\nabla}(\frac{B^2}{2\mu_0}) = \frac{B^2}{\mu_0}\frac{\hat{\boldsymbol{n}}}{R_{curv}} - \boldsymbol{\nabla}_{\perp}(\frac{B^2}{2\mu_0}) \tag{1.24}$$

We see from the above equation that the component of the force which acts along the field lines from the tension force is equal and opposite to that in the gradient in magnetic pressure so that both always cancel. Thus, the force of the magnetic pressure gradient will only be effective in the direction perpendicular to the field direction and this is a contrast to the gas-dynamic pressure (anisotropy in the presence of a magnetic field). Graphically, this magnetic pressure can be described as the tendency

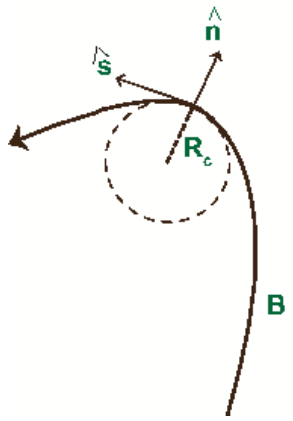

Figure 1.5: Orientation of the unit vectors $\hat{\boldsymbol{n}}$ and $\hat{\boldsymbol{s}}$, perpendicular and along the magnetic field line, respectively; R_c is the local curvature radius of the line.

of neighboring field lines to repulse each other.

The part of the tension force points toward the center of curvature of field lines and is antiparallel to the radius of curvature of field lines. This term is present only for curved field lines. The force always is a restoring force 'the magnetic tension'. If the field lines have a convex curvature into the upward direction, the force will be directed downwards. The magnetic tension can also be interpreted graphically: magnetic field lines have the tendency to shorten; *reducing the curvature*.

- An important consequence of $\beta \ll 1$ in the active region is that these regions evolve between eruptions through a sequence of force-free equilibria; the sequence being driven quasi-statically (slowly) from the photospheric boundary. Eruptions are the instabilities of the force-free equilibrium. *These are the main subjects of the thesis.*

Magnetic Diffusion

Frozen-in flux is connected with a perfectly conducting system as an essential concept in an ideal MHD.

The question now is what will happen if the field would be embedded in a flow with finite conductivity

MHD equations are a set of conservation laws. Under the frozen-in concept, the magnetic field lines and plasma are moving jointly in order to preserve the topology of the magnetic field line. This is a strong topological constraint, which prevents the magnetic field lines from " reconnecting". Therefore, even a small amount of resistivity can strongly has an impact on the plasma stability as it gives the field lines topology the chance to change within a localized area. To move from ideal to non-ideal MHD, we must include *dissipative effects*.

If $R_m \ll 1$ in the induction equation, for finite conductivity, usually in a localized region, the convective term can be neglected with respect to the diffusive term, thus

$$\frac{\partial \boldsymbol{B}}{\partial t} = \eta_m \nabla^2 \boldsymbol{B} \tag{1.25}$$

which is *the diffusion equation*. It indicates that the magnetic field variations on a length scale L are dissipated and decay over the *diffusion time scale*,

$$\tau_d = \frac{L^2}{\eta_m}. \tag{1.26}$$

This implies that the smaller the length scale is, the faster the magnetic field dissipates. The gradient of the magnetic field induces the current as $\longmapsto$ $\boldsymbol{J} = \frac{1}{\mu_0}\boldsymbol{\nabla} \times \boldsymbol{B}$. The magnetic field dissolves and its energy is decreasing as the current is dissipated into Ohmic losses heating.

Since solar flares represent a release of magnetic energy over a time-scale of 100 or 1000 s, it seems that the length scale is as small as $L \approx 10 - 100$ m. The field in this current sheet is diffusing away and so it is being annihilated and the magnetic energy converts into heat by Ohmic dissipation.

The diffusion of the magnetic field in a current sheet also allows for a magnetic reconnection, which additionally creates reconnection outflow jets from the ends of the current sheet. These hot jets carry kinetic energy which also originates from the magnetic energy.

1.6 Introduction to the CME Models

There are many approaches to the theoretical description of the various forms and aspects of solar eruptions. The arguments in this section deal with the models that focus essentially on the triggering processes and the dynamic development of the eruption. During the past years, the relation between filament eruptions and CMEs have been comprehensively examined (Subramanian and Dere, 2001; Chandra et al., 2010).

Elongated filament which most commonly exists in the quiet Sun between active regions are located along an inversion polarity line separating opposite magnetic polarities before eruption. Filaments are formed from dense and cool plasma. It is widely assumed that they are suspended against the gravity in dips of the twisted magnetic field lines. In addition, between 56% and 92% of solar filament eruptions occur jointly and lead to CMEs (Jing et al., 2004; Gopalswamy et al., 2003; Hori and Culhane, 2002; Liu et al., 2012). Therefore, many models which tried to explain the filament formation and eruption, involve a magnetic configuration of a so-called twisted flux rope as a prerequisite. One aspect, which must also be considered

in modeling CMEs, is when this magnetic flux rope should be present; already before or only during the eruption.

1.6.1 Flux Rope Eruption

A flux rope is described as a bundle of magnetic field lines that is twisting around an axis, creating helical shape by which the dense filament material is supported. These twisted magnetic fields are highly sheared and rooted on either side of a neutral line/polarity inversion line (PIL) of the photospheric flux. The footpoints of the potential (current free) arcade field lines may shift towards and along the PIL due to the photospheric motions. A twisted flux rope can be formed as a product of the reconnection of these highly sheared magnetic fields with subsequent flux cancellation (van Ballegooijen and Martens, 1989a). This reconnection takes place low in the solar atmosphere and so the photospheric material could be lifted up in the newly helical reconnected lines. The resulting helical shape may be around 1-1.5 turns or less than one turn. The filament in this case may be supported by nearly force-free flux rope which lies horizontally above the PIL (Kuperus and Raadu, 1974; van Ballegooijen and Martens, 1989a; Rust and Kumar, 1994). The two competing magnetic forces which put the flux rope in equilibrium, are the magnetic pressure and tension. Regions of strong magnetic pressure naturally tend to expand into regions of weaker magnetic pressure. Under this condition, an isolated flux rope would expand so that its axis would rise upward away from the solar photosphere. However, this is not what happen on the solar corona. The arcade-loops may arch over the flux rope, acting as an overlying magnetic field. These arcade field lines are rooted in the solar photosphere and their tension acts to maintain the flux rope in its place. The force-free condition is fulfilled here, where the gradient in the upward magnetic pressure force is balanced by the downward magnetic tension force.

So the question now is how this equilibrium condition will be broken, ensuing an eruption. Several models were suggested for how an eruption is initiated: new emergence of flux, flux cancellation and related reconnection of the magnetic field lines below the flux rope, shear motions and related reconnection of magnetic field lines above the sheared arcade, and/or twisting the configuration further. The first three mechanisms reduce the downward magnetic tension and favor the ascent of the magnetic field supporting the filament material. The fourth mechanism leads to kink unstable flux rope, triggering the eruption and leaving the configuration in more a relaxed state. The CME models may be classified as follows,

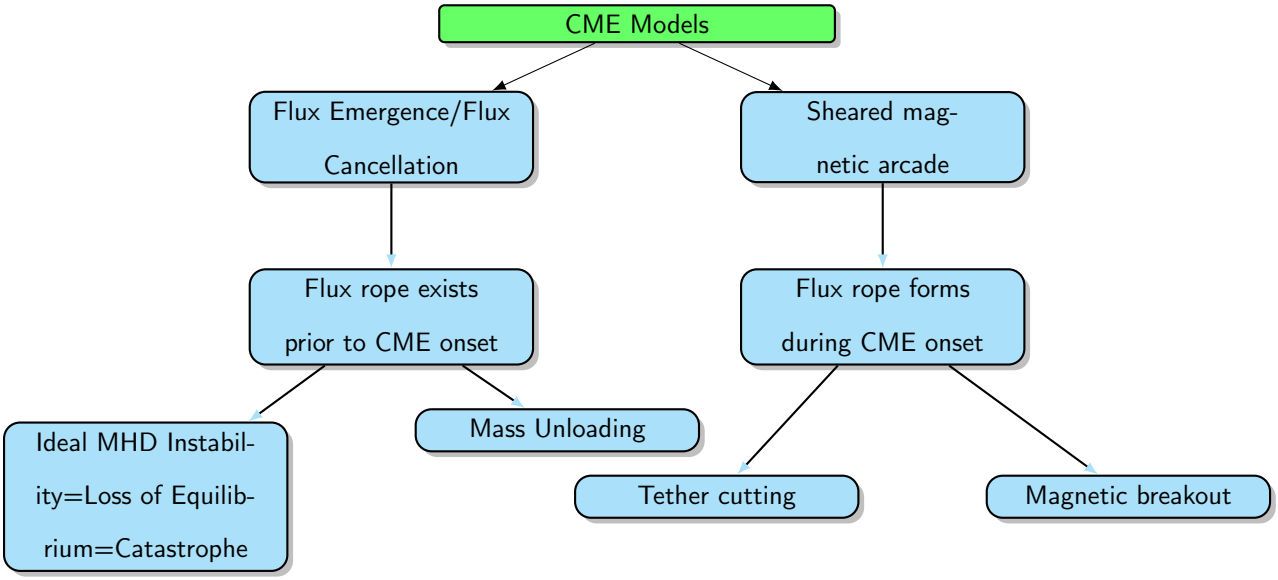

All of the above models are "Storage and Release" models. The slow photospheric plasma flows and the new emerging magnetic flux from the convection zone may distort the potential coronal magnetic field, which is anchored in the photosphere. Thereby, a free magnetic energy may be accumulated in the coronal magnetic field through a long period, and stored in the form of strong electric currents. During this process, the non-potential magnetic fields evolves quasi-statically through a series of equilibrium states. If, after a certain period of time, the distortion of the magnetic field exceeds a critical threshold, the equilibrium becomes unstable and the stored energy is now released, developing a solar eruption.

1.6.2 Flux Cancellation

How a flux rope can be created in the solar corona prior to an eruption to occur is still an open question. It may emerge from the solar convective zone (Rust and Kumar, 1994; Low, 1996) or be formed in situ by an arcade-to-rope topology transformation (van Ballegooijen and Martens, 1989a). In this model, the onset of the CME is triggered by a gradual evolution of the magnetic reconnection in the photosphere due to flux cancellation process near the PIL of sheared arcades. The converging motions of opposite polarity flux patches toward the PIL, along which the filament initially resides, can be easily driven by the development of super-granular cells. These converging motions in a sheared overlying magnetic field might lead to the mutual collision, merging and mostly canceling of magnetic fragments of the opposite polarity as illustrated in Figure 1.6. The gradual decline of the flux in this area of active regions in the vicinity of the PIL results in the internal reconnection which leads up to a filament eruption. The detailed solar observations in and around the active regions reveal many indications that the flux cancellation (Martin et al., 1985; Livi et al.,

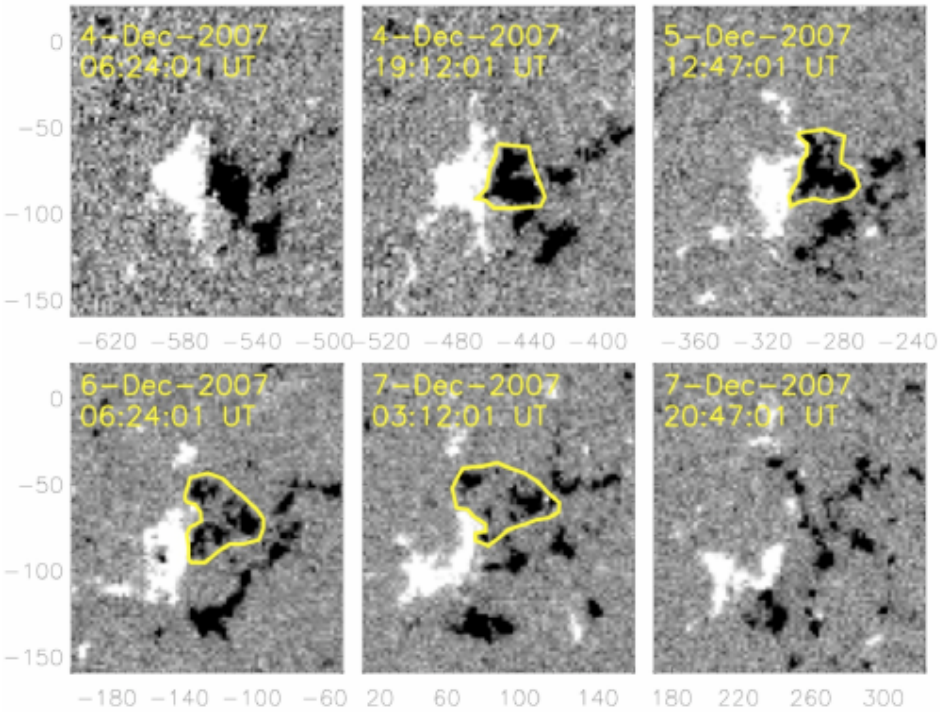

Figure 1.6: The dispersion of the magnetic field in an active region producing several CMEs. MDI longitudinal magnetograms of the AR during its disk passage on 4-7 Dec. 2007 (Green et al., 2011).

1985; Zwaan, 1987, 1996; Gaizauskas, 1993) is often connected with the solar eruptions (Flares and CMEs). Green et al. (2011) examined the eruption event on 7th December 2007 in the NOAA active region (AR) 10977. They presented a careful study regarding the way in which the flux cancellation episode might be the main cause for the formation of the flux rope during this event. This flux rope first produced a failed eruption, followed by a successful one (a CME) after 3.5 hours of the continued cancellation. They concluded that more than 34% of this AR's flux is canceled during the 2.5 days, while up to 60% of the flux could be potentially contained in the body of the flux rope. Analogous to many filament eruptions, small-scale filaments (called minifilaments) also display a gradual rise followed by a rapid rise during the eruption (Sterling and Moore, 2005; Panesar et al., 2015). Panesar et al. (2016, 2017) provided a clear evidence that the flux cancellation constitutes a central element in the basic process, which is a responsible for the formation of the minifilaments and for triggering them as jet eruptions, as is shown in Figure 1.7. They examined the structure and the evolution of different jets events. In each of these cases, the opposite polarity patches approached, merged, and canceled with each other with a flux reduction rate between 10% and 40% from the time prior to the minifilaments' appearance to after the eruption. Sustained photospheric reconnection at the PIL beneath the minifilament built twisted or at least highly sheared field lines. This lead to the upflow of a significant cool dense mass to form the minifilament. There has been the suggestion

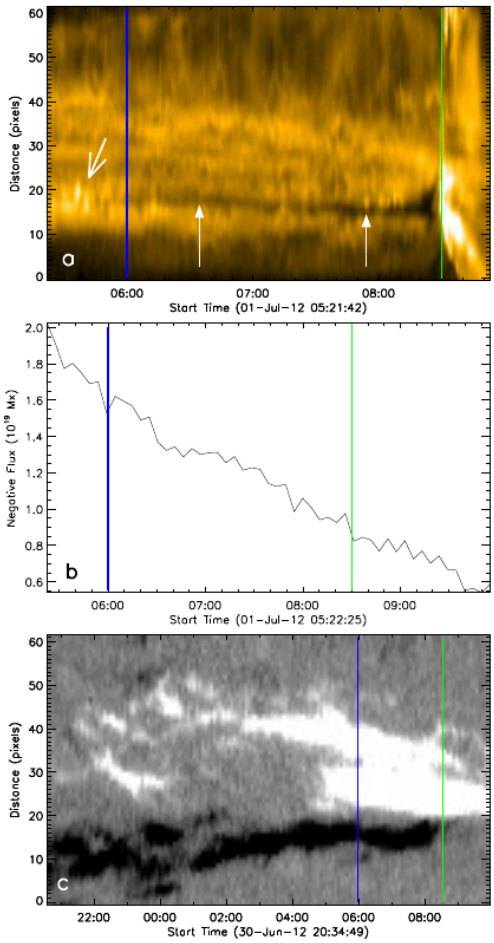

Figure 1.7: Minifilament formation and flux cancellation for jet on 01 Jul 2012: (a) The left-most arrow points to the brightening before the minifilament formation and the two upward-pointing arrows point to the dark minifilament cross-section. (b) Indicate the reduction of the negative flux as a function of time. (c) The blue and green lines mark the minifilament formation time and jet eruption time, respectively (Panesar et al., 2017).

that CMEs and jets maybe due to the same physical process operating on large and small scales, respectively (Sterling et al., 2015).

These indications led to the appearance of several models, which incorporate the flux cancellation process as a key ingredient in a filament formation and as well as its eruption (Pneuman, 1983; van Ballegooijen and Martens, 1989a, 1990; Gaizauskas et al., 1997; Martin, 1998; Mackay et al., 1998; Litvinenko and Martin, 1999; Amari et al., 1999; van Ballegooijen et al., 2000; Martens and Zwaan, 2001; Amari et al., 2000, 2003, 2010; Aulanier et al., 2010). The properties of the process can be summarized as follows:

- A stable magnetic flux rope forms above the PIL from the sheared arcades. The prominence magnetic field is a highly sheared structure and consequently they are magnetically energized. The flux rope is formed as a result of the photosphere's motions (van Ballegooijen and Martens, 1989a), Figure 1.8.

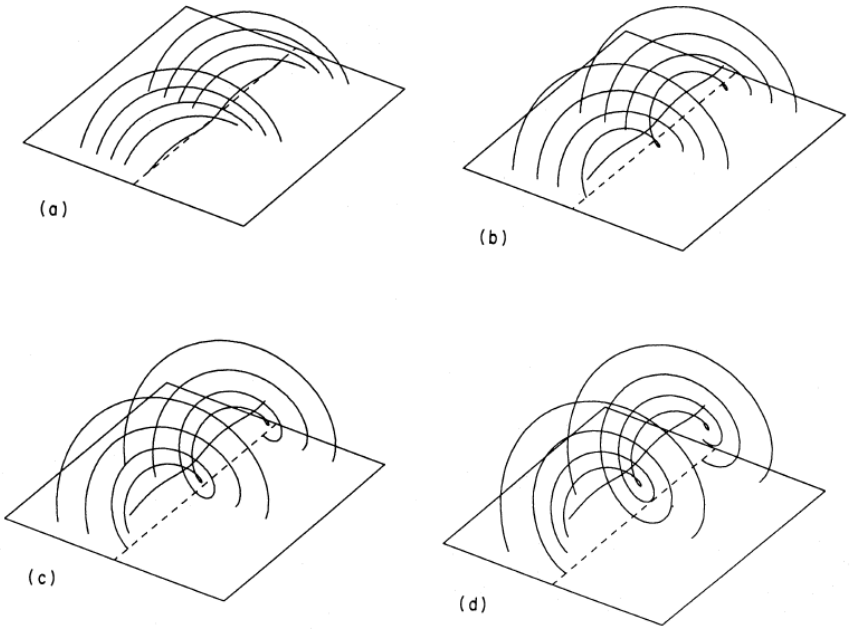

Figure 1.8: Flux cancellation in a sheared magnetic field. (a) Sheared arcades produced by flows along the PIL; (b-d) The reconnection produces the helical loops due to the converging motions toward the PIL (van Ballegooijen and Martens, 1989a).

The twisted flux rope is able to support the dense material of the filament against the solar gravity. The flux rope remains stable as long as the amount of flux reduction does not exceed the critical value to inject an eruption (Linker et al., 2001; Lionello et al., 2002).

- The simplest approach to lift up the flux rope is simply to decrease the magnetic tension of coronal potential arcades which initially restrain the stable current-carrying magnetic fields. If flux cancellation progress is continued and exceeds the threshold limit of flux reduction rate of at least 6-10% (Amari et al., 2000, 2003, 2010; Aulanier et al., 2010; Green et al., 2011; Savcheva et al., 2012), the stored free magnetic energy can trigger an eruption, as shown in Figure 1.9.

Finally, the flux cancellation mechanism is an attractive hypothesis. It can explain both prominence formation and the initiation of CMEs with associated prominence eruptions. The magnetic flux is annihilated and then convert sheared fields into a flux rope. The flux rope, which supports the cool and dense material in prominences, can be stable for hours, days or weeks. When the cancellation increases the magnetic pressure in the flux rope to the critical value, the violent eruption will take place. The critical value has to exceed the tension value of the surrounding field.

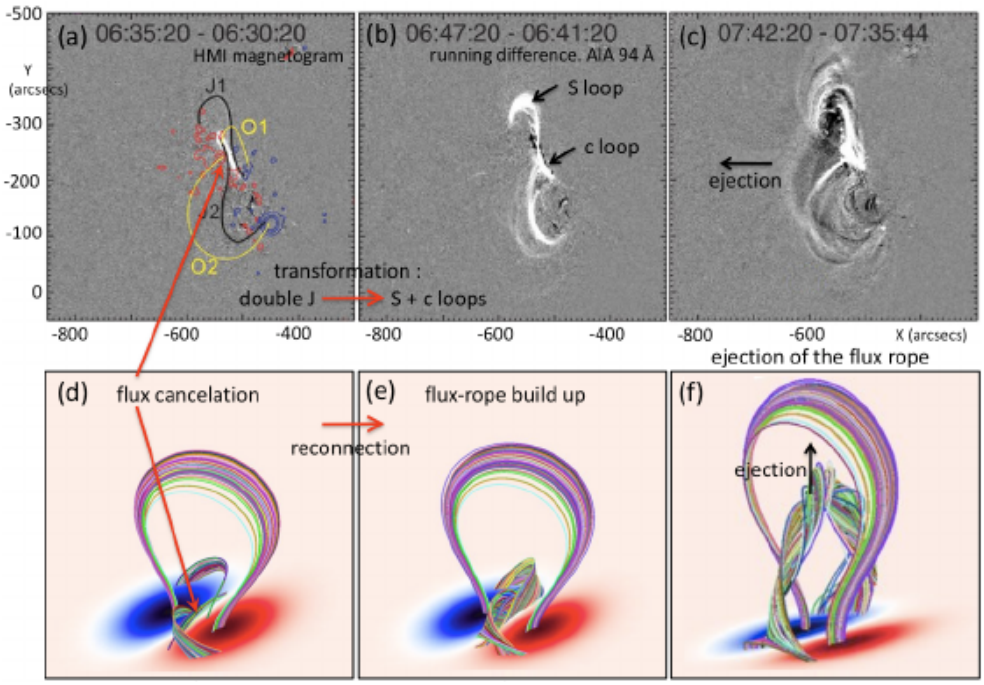

Figure 1.9: The build-up and eruption of a flux rope. (a-c) The formation and the eruption of a sigmoid observed by AIA 94 *Å*. The presence of a sigmoid is the signature of strong currents aligned with the magnetic field (Liu et al., 2010). (d-f) MHD simulation showing the built up of a flux rope, by reconnection of the field lines due to flux cancellation along the PIL and later on the flux rope eruption due to an ideal MHD instability (Amari et al., 2010).

1.6.3 Ideal Instability MHD, Flux Rope Catastrophe and Loss of Equilibrium

Loss-of-equilibrium or instability is widely accepted as the most likely mechanism for the CMEs eruption. The basic idea for this type is: when the coronal magnetic field is subjected to photospheric motions, building up free magnetic energy and evolving in a quasi-statical way (both ideally and non-ideally), it might reach a critical point (a threshold) where the pre-CME structure transitions to an unstable equilibrium (i.e., Ideal MHD Instability), as shown in Figure 1.10. Equivalently, no nearby equilibrium state exists anymore, i.e., a loss of equilibrium will occur for the coronal fields.

- Kink instability: An important field in the plasma physics is the stability of the plasma. Once it has been established that the plasma is in equilibrium, the stability of the equilibrium must be analyzed. Equilibrium asks whether there are net forces that will accelerate any part of the plasma. If there are no net forces then stability analysis asks whether a small perturbation will grow, oscillate, or be damped out. The magnetic flux rope with enough twist can become unstable by entering the helical kink instability regime. Kink instability is an ideal MHD instability, capable of triggering the initiation of an eruption when the average twist of a flux rope exceeds a critical limit. For solar conditions, the

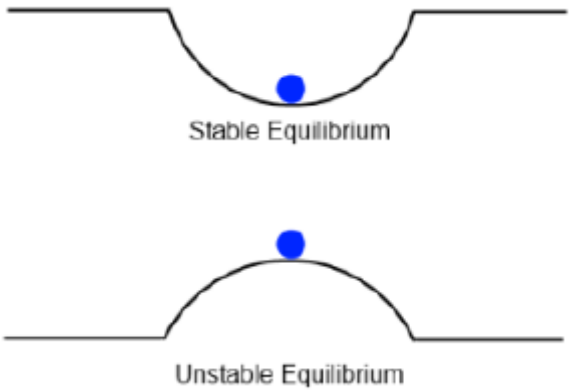

Figure 1.10: (Top) If this stable equilibrium is perturbed, the ball will return to its original location, or oscillate around it if damping is weak. (Bottom) If this unstable equilibrium is perturbed, the ball will roll away. Image credit: Public Domain

observational and numerical experience has shown that the critical value is about 3.5π (Török et al., 2004; Wang et al., 2016). The instability is illustrated in Figure 1.11. When the flux rope becomes helical kink unstable, it rises upward and then writhes, converting its twist into writhe as illustrated in Figure 1.11 bottom right part. The deformation of the unstable flux rope's axis forms an inverse γ shape or Ω shape, depending on the viewing direction (Ji et al., 2003; Romano et al., 2003; Gilbert et al., 2007; Guo et al., 2010; Hassanin and Kliem, 2016).

Several studies show the effect of the external overlying magnetic fields on the twisted flux tube and how they would stabilize the flux tube (Török and Kliem, 2005; Inoue and Kusano, 2006). According to Török and Kliem (2005), if the overlying magnetic arcades decay only gently with height, the kink instability would be suppressed after initial development, producing the so-called "failed or confined eruption" found by Ji et al. (2003). Otherwise, a torus instability sets in and accelerates the flux rope into the interplanetary space (CMEs).

- Torus instability: is closely related to the processes "flux rope catastrophe" and "loss of equilibrium". Démoulin and Aulanier (2010) and Kliem et al. (2014) showed that all three are equivalent CMEs models. In this case, a current ring is unstable against the expansion if the constraining potential field declines with height rapidly enough. In this instability, the Lorentz self-force, also called hoop force, which results from the curvature of a current-carrying flux rope, is the main driver for the expansion of the flux rope and also for the acceleration of the ejecta. A critical point is given by a so-called decay index ,$n = \frac{\delta ln B}{\delta ln z} = \frac{3}{2}$ (Bateman, 1978; Kliem and Török, 2006; Török and Kliem, 2007), which qualifies how the potential magnetic field declines along the vertical direction (z-axis). Above this value, $n > \frac{3}{2}$,

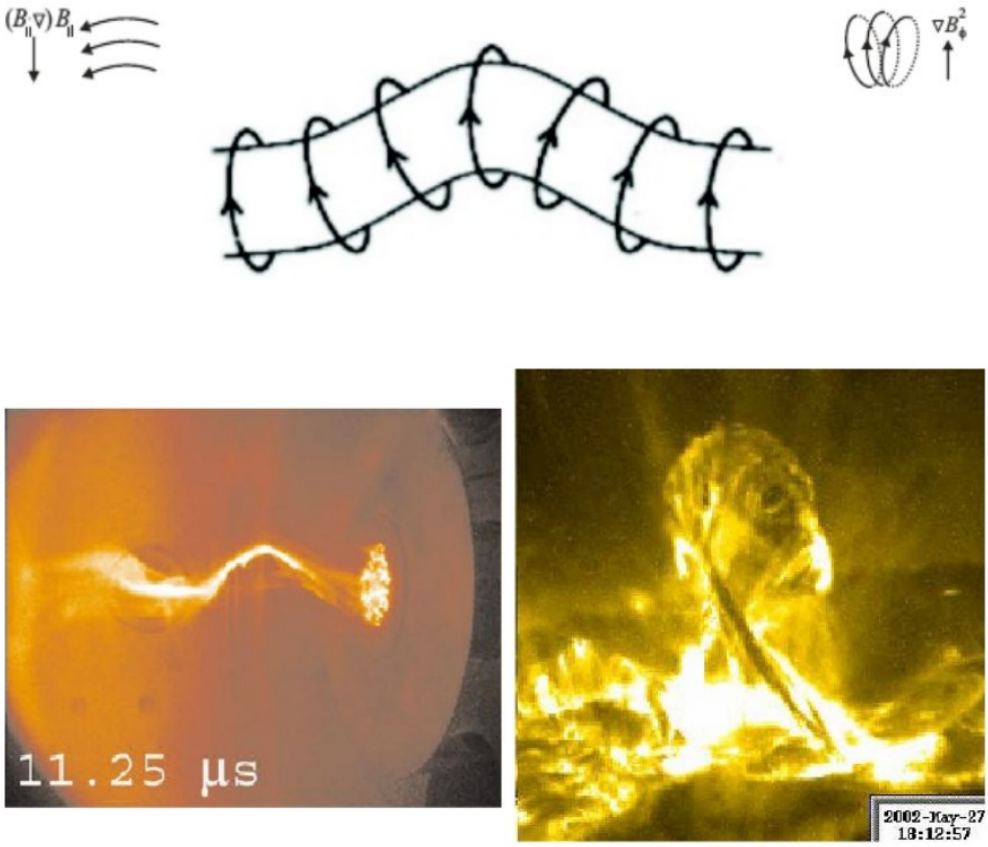

Figure 1.11: The top figure is a cartoon of a part of a flux rope with twist. Above the flux rope, at the left and right corners the effects of magnetic tension and pressure gradient are indicated. At the bottom left, the figure shows a laboratory plasma jets which is kink unstable (Hsu and Bellan, 2005). Török and Kliem (2005) show that a flux rope on the Sun can be unstable due to the helical kink instability (bottom right).

the unstable flux rope can produce a successful eruption (a CME) (Török and Kliem, 2007). The instability takes place when the decline in altitude of the downward magnetic tension becomes faster than of the upward magnetic pressure gradient. With 3D MHD simulations, Fan and Gibson (2007) studied the emergence of a flux rope from the subsurface into the magnetized corona. As illustrated by Figure 1.12, when the background magnetic field declines slowly with height, a strongly-twisted flux tube emerging out of the solar surface may still rupture through the arcade field via the kink instability (top panels); but this only rarely observed. On the other hand, when the background magnetic field declines rapidly with height, a weakly-twisted flux tube, whose twist is below the threshold for the helical kink instability, still erupts with little writhing like a planar outward expansion. They interpret that the latter case as the "torus instability". Aulanier et al. (2010) showed that before the eruption, the flux cancellation and tether-cutting reconnection (see below for explanation) build up the flux rope which first ascends slowly. When the rising flux rope exceeds the critical height at which the torus

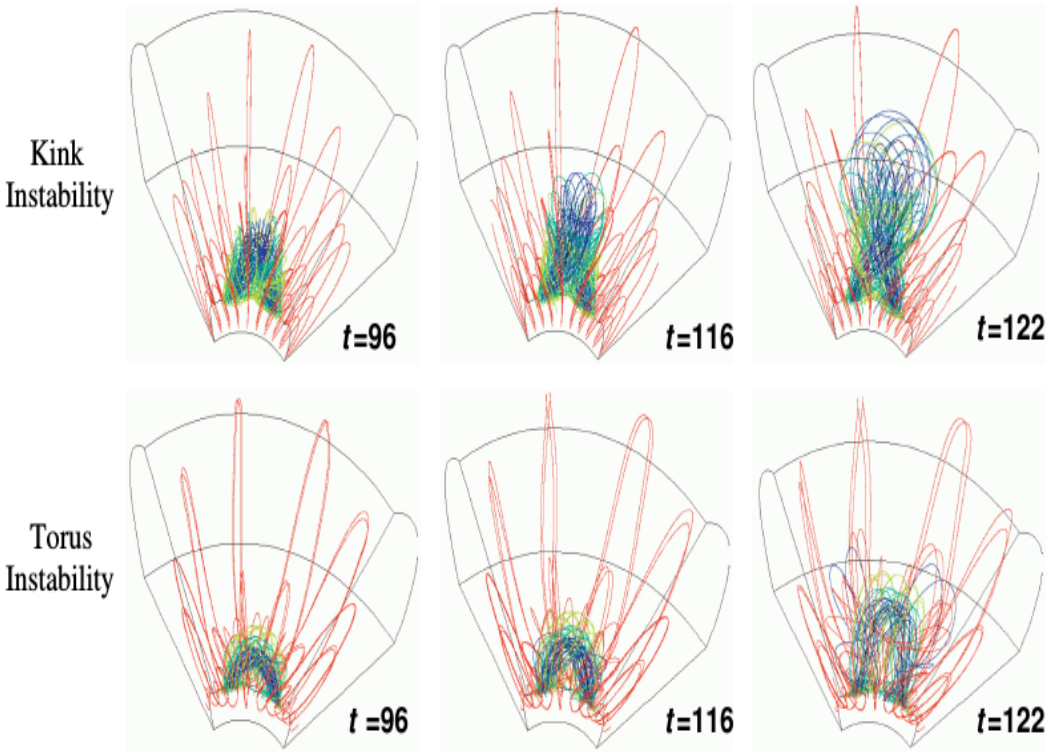

Figure 1.12: Top: the MHD simulation of the kink instability of a strongly-twisted flux tube emerging from the subsurface to the corona, where the pre-existing magnetic field declines slowly with height. Bottom: the MHD simulation of the torus instability of a weakly-twisted flux tube emerging into the corona, where the pre-existing magnetic field declines rapidly with height (Fan and Gibson, 2007).

instability takes place, the flux rope erupts, producing an ejective eruption, i.e., a CME. They also argued that the torus instability is the driver of the eruption (not the reconnection-involved processes) which causes the rapid acceleration of the erupting flux rope, producing a CME. Many observational and numerical investigations have now the suggestion that the torus instability causes the majority of CMEs (Zuccarello et al., 2016; Wang et al., 2017).

1.6.4 Tether-Cutting

The "Tether Cutting" model requires the resistive MHD for the description of the triggering process, and it is based on a pre-existing magnetic arcade configuration (Moore and Labonte, 1980; Moore et al., 2001). The starting point of the model is a bipolar active region with a core field and overlying arcade above it as shown in Figure 1.13. The core field consists of two closely J-shaped field-line systems, which together have a sigmoidal shape and are able to accumulate filament dense material. According to this model, the event onset is due to reconnection of two inner legs of a sigmoidal magnetic structure (J-shaped), which produces low-lying shorter loops across the magnetic PIL and longer twisted loops linking the two far ends of the

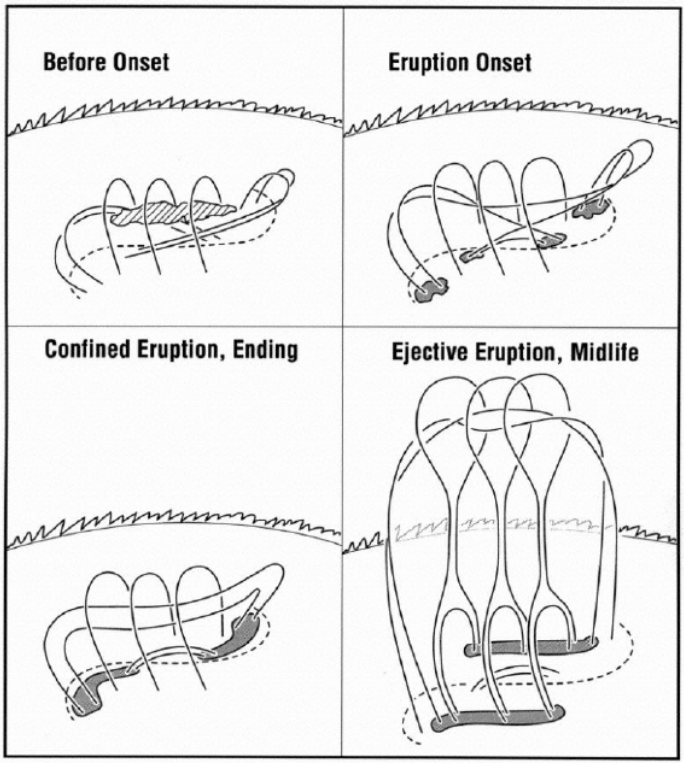

Figure 1.13: The field configuration is shown before, during, and after the onset of the eruption that takes place by internal tether-cutting reconnection (Moore et al., 2001).

sigmoid. The second stage begins when the twisted loops become unstable and erupt outward, distending the overarching envelope field. The reconnection of the flare in this model, is not a consequence of the eruption but its cause. It is assumed that the reconnection amplifies itself in "a Runaway" regime .
The legs of the envelope field subsequently reconnect back to form an arcade structure with bright ribbons at their footpoints, and the ejected flux rope escapes as a CME. Even though tether-cutting reconnection has been found to sustain the formation of twisted field lines in 3D MHD simulations of sheared non-eruptive fields (DeVore and Antiochos, 2000), and of emerging erupting fields (Manchester et al., 2004) (Archontis and Török, 2008), it has so far not been identified to be a main eruption driver in any 3D MHD simulations (Aulanier et al., 2010).

1.6.5 Breakout Modeling

Syrovatskii (1982) explained the eruptive behavior by multipolar configurations. The breakout model describes the eruption of multipolar configurations and how an eruption may be triggered in sheared arcades containing a filament channel by the magnetic reconnection in a magnetic null line above the arcade. This removes the constraint above the filament channel and allows it to rise and erupt and a flux rope will form

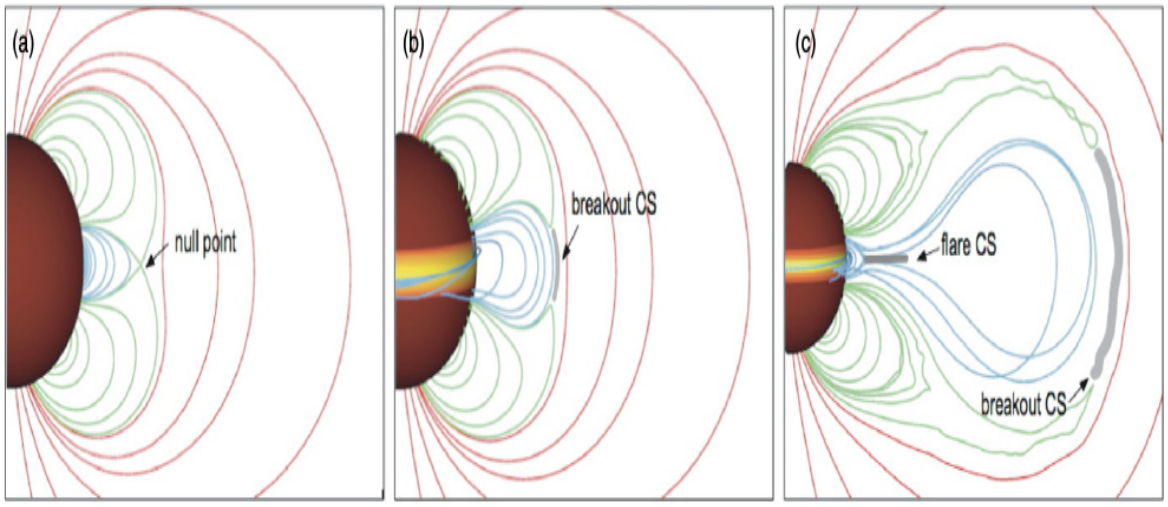

Figure 1.14: The three figures show Selected magnetic field lines at three times during the simulation, illustrating the key structures of the breakout model including current sheets (CS). Red lines indicate overlying field, green indicates side lobe field lines, and blue indicates core field lines (Karpen et al., 2012).

during the eruption (Antiochos, 1998; Antiochos et al., 1999; MacNeice et al., 2004; Lynch et al., 2004; DeVore and Antiochos, 2005; Karpen et al., 2012). The model requires a quadrupolar initial configuration and a sheared magnetic field near the PIL in the middle arcade as shown in Figure 1.14. With the inclusion of the magnetic resistivity and sufficient shearing, by means of magnetic reconnection removes the outer magnetic field arcade, which enables the further ascent of the central arcade.

The low-lying field lines expand radially. Then they begin to approach the open state. Consequently, a vertical current sheet forms deep inside the sheared field region. This leads to reconnection there. However, in this model there is no flexibility with respect to the magnetic complexity. The breakout cannot operate in a truly bipolar field and it requires the occurrence of a reconnection as an external aid that transfers a substantial amount of flux from the overlying field to erupting the side arcades.

1.6.6 Motivation

In many cases, an erupting filament remains confined in the corona without evolving into a CME. Due to the recent advances of observing capabilities, the observational studies of confined eruptions have become quite frequent (Liu et al., 2009, 2014; Shen et al., 2012; Netzel et al., 2012; Chen et al., 2013; Kuridze et al., 2013; Joshi et al., 2014b; Kumar and Cho, 2014; Kushwaha et al., 2014, 2015; Song et al., 2014; Yang et al., 2014; Cheng et al., 2015; Xue et al., 2016). Clarifying the factors that determine the confined vs. the ejective nature of an eruption is necessary to establish a comprehensive model of solar eruptions. Therefore, in this thesis we conduct firstly a detailed and comprehensive parametric MHD simulation study driven by the

helical kink instability, to model the confined event on 27 May 2002 (Ji et al., 2003). In a second step, we complete the parametric study to test whether the model can still yield a good match with the observed data, if the included line tying is much more realistic. For this purpose, we submerge the center point of the toroidal flux rope deeper below the photosphere to obtain a flatter initial coronal rope section. As an unexcepted result is that a flux rope can reform after an eruption. Since it is known that solar eruptions are a release of energy which stored in the coronal magnetic field by slow photospheric changes, we also investigate if the converging motions are key ingredients for building up magnetic energy in a reformed flux rope, which may lead to its eruption. Furthermore, we shed an additional light about another possibility of the formation of flux rope, beside flux emergence and flux cancellation process. For the simulation models of this thesis, the concept of the kink and torus instability of a twisted flux rope is invoked as a possible scenarios for triggering process of solar eruptions.

The simulations were performed using fully three-dimensional MHD simulations as Fortran code. The work is based on the use of the Titov & Démoulin (1999) model as the initial equilibrium for the simulations Titov and Démoulin (1999). This thesis is organized in the following chapters. The introduction in *chapter 1* describes the solar activity as well as CMEs models and compiles the MHD equations. *Chapter 2* is dedicated to the numerical model we use in the simulations. In *chapter 3*, we present the extension work of Török and Kliem (2005) to obtain a complete modeling of the confined eruption on 2002 May 27 and a much more realistic manner of this event, is achieve in *chapter 4*. *Chapter 5* presents a new approach for modeling homologous eruptions by imposing motions in the bottom boundary, such as converging motions and building up a free magnetic energy in the flux rope. Last, a summary of this thesis is presented in *chapter 6*, together with perspectives. The refereed publications are enclosed in *chapter 7*.

CHAPTER 2

Numerical Modeling

Solving the MHD equations can be very intricate, since they are coupled to each other. Unless several approximations are made, numerical methods are needed to solve such equations. To perform the simulations that are presented in the next chapters we use the numerical code of Török and Kliem (2003) (TK03), which solves the full set of 3D ideal MHD equations using a modified Lax-Wendroff scheme. Similar to Török and Kliem (2005) (TK05), we use the Titov and Démoulin (1999) (TD99) model of a force-free flux rope equilibrium in bipolar ambient field as the initial condition. In this chapter, we describe the main characteristics of such tool to study confined eruption and the homologous eruptions.

2.1 Governing Equations and Normalization of the Variables

Recalling the compressible ideal MHD equations, which we complied in the first chapter, and employing the simplifying assumptions of zero plasma beta and gravity, we have

$$\begin{aligned} \partial_t \rho &= -\boldsymbol{\nabla} \cdot (\rho\, \boldsymbol{u})\,, \\ \rho\, \partial_t \boldsymbol{u} &= -\rho\, (\boldsymbol{u} \cdot \boldsymbol{\nabla})\, \boldsymbol{u} + \boldsymbol{J} \times \boldsymbol{B} + \boldsymbol{\nabla} \cdot \mathbf{T}\,, \\ \partial_t \boldsymbol{B} &= \boldsymbol{\nabla} \times (\boldsymbol{u} \times \boldsymbol{B})\,, \\ \boldsymbol{J} &= \mu_0^{-1}\, \boldsymbol{\nabla} \times \boldsymbol{B}\,, \end{aligned} \tag{2.1}$$

where T denotes the viscous stress tensor ($\mathsf{T}_{ij} = \rho\,\nu\,[\partial u_i/\partial x_j + \partial u_j/\partial x_i - (2/3)\delta_{ij}\,\boldsymbol{\nabla}\cdot\boldsymbol{u}]$) and ν is the kinematic viscosity. The bulk viscosity is neglected (since the viscous term is included only to facilitate relaxation towards equilibrium states and to improve numerical stability).

We normalize the variables, using the initial apex height of the flux rope h_0, as the characteristic length, the magnetic field strength $\tilde{B}_{0z_{max}}$, density $\tilde{\rho}_0$, and Alfvén velocity $\tilde{v}_{a0} = \dfrac{\tilde{B}_{0z_{max}}}{(\mu_0\tilde{\rho}_0)^{\frac{1}{2}}}$, at the axis of the TD99 flux rope, and the corresponding Alfvén time $\tau_A = h_0/\tilde{v}_{a0}$. The units are h_0, $\tilde{v}_{a0}$, τ_A, $\tilde{\rho}_0$, $\tilde{B}_{0z_{max}}$, and $\dfrac{\tilde{B}_{0z_{max}}}{\mu_0 h_0}$ for $\boldsymbol{x}$, $\boldsymbol{u}$, t, ρ, $\boldsymbol{B}$, and $\boldsymbol{J}$, respectively.

After some manipulation, the set of the ideal MHD equations can be written in the flux conservative form, i.e., in the following format:

$$\partial_t \boldsymbol{U} + \partial_x \boldsymbol{F}(\boldsymbol{U}) + \partial_y \boldsymbol{G}(\boldsymbol{U}) + \partial_z \boldsymbol{H}(\boldsymbol{U}) = 0, \tag{2.2}$$

where $\boldsymbol{U}$ is the vector of the integration variables and $\boldsymbol{F}$, $\boldsymbol{G}$, $\boldsymbol{H}$ are nonlinear flux terms,

$$\boldsymbol{U} = \begin{pmatrix} \rho \\ \rho u_x \\ \rho u_y \\ \rho u_z \\ B_x \\ B_y \\ B_z \end{pmatrix}, \quad \boldsymbol{F} = \begin{pmatrix} \rho u_x \\ \rho {u^2}_x + \frac{1}{2}(-{B^2}_x + {B^2}_y + {B^2}_z) \\ \rho u_x u_y - B_x B_y \\ \rho u_x u_z - B_x B_z \\ 0 \\ u_x B_y - u_y B_x \\ u_x B_z - u_z B_x \end{pmatrix}, \quad \boldsymbol{G} = \begin{pmatrix} \rho u_y \\ \rho u_x u_y - B_x B_y \\ \rho {u^2}_y + \frac{1}{2}({B^2}_x - {B^2}_y + {B^2}_z) \\ \rho u_y u_z - B_y B_z \\ u_y B_x - u_x B_y \\ 0 \\ u_y B_z - u_z B_y \end{pmatrix},$$

$$\boldsymbol{H} = \begin{pmatrix} \rho u_z \\ \rho u_x u_z - B_x B_z \\ \rho u_z u_y - B_z B_y \\ \rho {u^2}_z + \frac{1}{2}({B^2}_x + {B^2}_y - {B^2}_z) \\ u_z B_x - u_x B_z \\ u_z B_z - u_y B_z \\ 0 \end{pmatrix} \tag{2.3}$$

and $j_x = \partial_y B_z - \partial_z B_y, \quad j_y = \partial_z B_x - \partial_x B_z, \quad j_z = \partial_x B_y - \partial_y B_x$.

For more information, we refer to Ugai and Tsuda (1977) , where the pressure term and energy equation are

included, and to Török and Kliem (2003).

2.2 The Modified Lax-Wendroff Scheme

For three Cartesian variables x, y and z, the conservative form of the MHD equations is given in eq.(2.2) and eq.(2.3). The numerical scheme which is is adopted in our simulations, is the modified two-step Lax-Wendroff scheme as in Török and Kliem (2003, 2005), is derived using a second-order Taylor expansion of $\boldsymbol{U}$ in time where the spatial derivatives of $\boldsymbol{F}$, $\boldsymbol{G}$ and $\boldsymbol{H}$ replace the time derivatives of $\boldsymbol{U}$ (Richtmyer and Morton, 1967; Török and Kliem, 2003). In order to achieve numerical stability for a finite-difference scheme of second-order accuracy in both time and space, a two-step scheme was introduced. The standard version of first step provides the auxiliary variables at time $t = (2n+1)\Delta t$ from the values at $t = 2n\Delta t$,

$$U^{\mathrm{n+1}}_{\mathrm{i,j,k}} = \frac{1}{6}(U^{\mathrm{n}}_{\mathrm{i+1,j,k}} + U^{\mathrm{n}}_{\mathrm{i\text{-}1,j,k}} + U^{\mathrm{n}}_{\mathrm{i,j+1,k}} + U^{\mathrm{n}}_{\mathrm{i,j\text{-}1,k}} + U^{\mathrm{n}}_{\mathrm{i,j,k+1}} + U^{\mathrm{n}}_{\mathrm{i,j,k\text{-}1}}) - \frac{\Delta t}{2\Delta x}(F^{\mathrm{n}}_{\mathrm{i+1,j,k}} - F^{\mathrm{n}}_{\mathrm{i\text{-}1,j,k}}) - \frac{\Delta t}{2\Delta y}(G^{\mathrm{n}}_{\mathrm{i,j+1,k}} - G^{\mathrm{n}}_{\mathrm{i,j\text{-}1,k}}) - \frac{\Delta t}{2\Delta z}(H^{\mathrm{n}}_{\mathrm{i,j,k+1}} - H^{\mathrm{n}}_{\mathrm{i,j,k\text{-}1}}), \tag{2.4}$$

where the i, j and k subscripts are for the space variables x, y and z respectively.

The first term on the right-hand side of eq.(2.4) of the standard Lax-Wendroff scheme leads to the effective first-order spatial derivatives at the grid point (i, j, k) being averaged by the spatial derivatives obtained at the six nearest neighbors $(i+1, j, k), (i-1, j, k), (i, j+1, k), (i, j-1, k), (i, j, k+1)$ and $(i, j, k-1)$. This averaging is known as the "Lax step" and enhances the numerical diffusion and thereby improves the numerical instability. This can be considered as a disadvantage if the required derivatives of quantities exhibit a high spatial variation, such as the magnetic component in our investigated configurations in the areas of strong field. Therefore, this averaging term is replaced by $U^{\mathrm{n}}_{\mathrm{i,j,k}}$ (Török and Kliem, 2003). With this modification, the effective spatial derivatives are calculated directly at the grid point. The second step of our scheme, which calculates the physical variables at time $t = (2n+2)\Delta t$, is the standard second Lax-Wendroff step:

$$U^{\mathrm{n+2}}_{\mathrm{i,j,k}} = U^{\mathrm{n}}_{\mathrm{i,j,k}} - \frac{\Delta t}{\Delta x}(F^{\mathrm{n+1}}_{\mathrm{i+1,j,k}} - F^{\mathrm{n+1}}_{\mathrm{i\text{-}1,j,k}}) - \frac{\Delta t}{\Delta y}(G^{\mathrm{n+1}}_{\mathrm{i,j+1,k}} - G^{\mathrm{n+1}}_{\mathrm{i,j\text{-}1,k}}) - \frac{\Delta t}{\Delta z}(H^{\mathrm{n+1}}_{\mathrm{i,j,k+1}} - H^{\mathrm{n+1}}_{\mathrm{i,j,k\text{-}1}}) \tag{2.5}$$

2.3 The Artificial Smoothing

We employ a modified version of the Lax-Wendroff scheme to evolve the ideal-MHD equations. While highly diffusive, the original Lax-Wendroff scheme has the advantage of being very stable. During the so called Lax step, the value of the variables in each grid cell is replaced by the average from its immediate neighbor cells. In order to stabilize the modified scheme, we apply an artificial smoothing to the density and velocity variables $\Psi = (\rho, u_x, u_y, u_z)$ (Sato and Hayashi, 1979) after the time step instead of fully replacing the variable value by its neighbors average in the auxiliary step according to the following expression:

$$\Psi^{n}_{i,j,k} \rightarrow (1-\sigma)\Psi^{n}_{i+1,j,k} + \frac{\sigma}{6} * (\Psi^{n}_{i-1,j,k} + \Psi^{n}_{i+1,j,k} + \Psi^{n}_{i,j-1,k} + \Psi^{n}_{i,j+1,k} + \Psi^{n}_{i,j,k-1} + \Psi^{n}_{i,j,k+1}) \tag{2.6}$$

For $\sigma = 1$ this yields the Lax step. In practice, values $\sigma = 0.001 - 0.05$ are used. Thus the artificial smoothing can be interpreted as a strongly reduced Lax step which can be adapted to each simulation for the optimum compromise between numerical diffusion and stability. For the magnetic field we only apply the artificial smoothing for further stabilization when necessary, to avoid reducing the currents (free energy) and Lorentz force. In the simulations reported in this thesis, the magnetic field is smoothed only when localized flow pattern is imposed in the bottom plane and only for the bottom plane in the vicinity of the polarity inversion line, where the flows converge. Spatially varying smoothing is implemented. $\boldsymbol{u}$ and ρ are smoothed the level of $\sigma = 0.05$ at $z = 0$ and at $\sigma = 0.001$ for $z > 0.5$, with a gradual transition at intermediate height (*Chapter 5*). In this work we adopt the philosophy of implementing the numerical diffusion as required by the different runs, and at the same time we keep the identical numerical diffusion for runs that have similar initial conditions.

2.4 Definition of the Non-Uniform Grid

The simulations of this work require the best possible spatial resolution, in order to enable relatively small-scale processes near the flux rope to be studied such as the formation of current layers, as well as a large simulation box in order to track the rise of the magnetic flux rope for a sufficiently large height range of about $1R_{\odot}$. Therefore, a stretched grid with spatially varying resolution is used, as illustrated in Figure 2.1. Now a suitable function $x(w)$ has been chosen, such as

$$x(w) = w + a_1[exp(b[w - w(s)]^2) - 1] + a_2[exp(b[w - w(s)]^C) - 1] \tag{2.7}$$

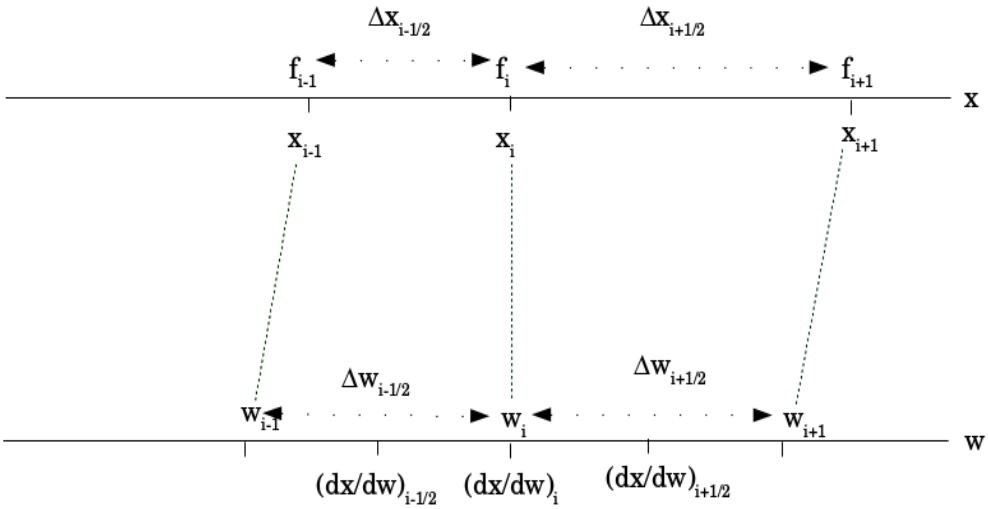

Figure 2.1: Non-uniform grid defined through the use of a stretched coordinate system where x-axis represents the stretched grid and w-axis represents the auxiliary uniform grid. A function $f(x)$ is defined on a nonuniform grid.

where $w(s)$ is introduced to allow a central uniform grid with $x(i) = w(i)$ in a volume that encloses the initial flux rope, as illustrated in the Figure 2.1. a_1, a_2, b, and C are chosen to be free parameters to allow a high flexibility in the choice of the grid size.

2.5 The Choice of Time Step

A variable time step, which is used in the numerical algorithm, has to obey the Courant-Friedrichs-Levy (CFL) criterion. The CFL condition expresses that any information is not allowed to travel through more than one cell for every spatial direction i within one time-step

$$\Delta t < \frac{\Delta_i}{|u_i| + v_f} \tag{2.8}$$

Here, $\Delta = Min(\Delta x, \Delta y, \Delta z)$ on the grid, $u_i(t)$ is the velocity of the flow and v_f is the highest propagation velocity of the MHD waves on the grid, which is v_{Ao} (in our approximation of zero plasma-β). v_f is set in this work as $v_f = v_{a_{max}}(t = 0) = 1$. The smaller Δt, the more stable is the scheme, but the simulation consumes more time. The time step varies in the course of the simulations, in accordance with the evolution of $Max(u(t))$on the grid.

2.5.1 The Adopted Grid

We consider a finite cube of size $[-L_x, L_x] \times [-L_y, L_y] \times [0, L_z]$ for the physical domain. The domain can be restricted in this study to the *half cube* $[-L_x, L_x] \times [0, L_y] \times [0, L_z]$ because the considered configurations are line-symmetric with respect to the z-axis. The simulations are performed on two differently sized grids- $141 \times 319 \times 505$ and $241 \times 190 \times 207$- resolving the computational domain $|x| \leq 5$, $|y| \leq 5$, $0 \leq z \leq 10$ and $|x| \leq 16$, $|y| \leq 16$, $0 \leq z \leq 32$, respectively, with resolution 0.02 in the flux rope area. In order to implement the boundary conditions, two layers of "ghost points" are added to the box in each direction.

2.6 Titov-Démoulin (TD99) Model as the Initial Condition

The initial magnetic configuration of the simulations is an analytical equilibrium model, developed by Titov and Démoulin (1999) which contains a twisted current-carrying flux rope in an approximate force-free equilibrium. This allows us to perform an extended parametric study. The axisymmetric model developed by TD is shown in Figure 2.3. It consists of a circular flux tube with a toroidal ring current, I, with the apex at height $z = h$ above the photospheric surface $z = 0$. The toroidal ring current has a torus radius R; the major radius, and a tube radius a; the minor radius. Below the photospheric surface, which represents the bottom boundary of the computation box, the symmetry axis of the torus is located at a depth d. Two subphotospheric magnetic points sources of strength $\pm q$, buried at the symmetry axis, provide the external poloidal field component $\boldsymbol{B}_{ep}$ (also called the "strapping field"), which counterbalances the outward-directed Lorentz self-force of the current channel (hoop force of the rope (Shafranov, 1966)). These two magnetic sources resemble the pair of main sunspots in a bipolar active region. Under such force-free equilibrium, the field lines at the surface of the flux rope are purely poloidal, and they have an infinite number of turns in a finite length. To produce a finite twist throughout the configuration, an external toroidal field component, $\boldsymbol{B}_{et}$, is introduced by a line current, I_0, running along the symmetry axis. The purpose of the external toroidal field is to control the number of turns of the field lines within the flux rope. This component models the shear field typically seen in active regions. The field by the line current is known to prevent ejective eruptions (Roussev et al., 2003; Török and Kliem, 2005). The system has six free parameters R, d, L, N_t, q and I_0, where N_t which are indicated in Figure 2.3, denotes the number of turns of the field lines around the torus axis at the surface of the torus. Instead of N_t, it is possible to prescribe a, the small raduis of the flux rope. The choice of these parameters determines the equilibrium ring current I (see TD99). Using an unstable state of this equilibrium to produce a confined eruption is the purpose of the first part of the thesis. This is initially studied by varying the initial twist of the flux tube N_t and the line current I_0. In

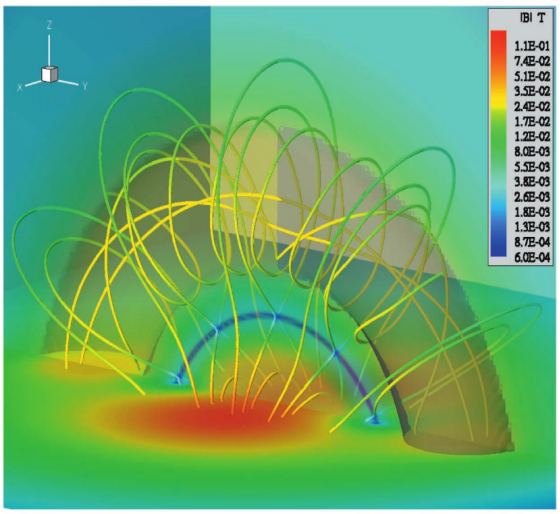

Figure 2.2: Three-dimensional view of the magnetic field configuration for the initial state. The magnetic X-line is highlighted by blue Roussev et al. (2003).

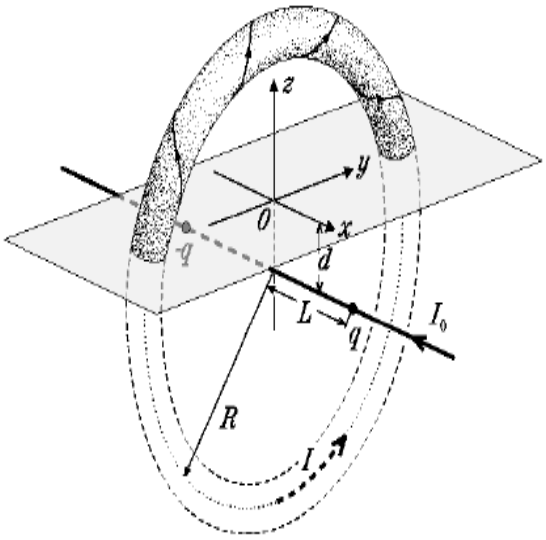

Figure 2.3: Titov & Démoulin (1999) model of a twisted magnetic flux tube.

the TD equilibrium with sufficient twist and a sufficiently large value of I_0, a kink instability occurs and develops into a confined eruption. In addition, another ideal MHD instability can occur in the TD system, which manifests itself in a global expansion of the flux tube; *torus instability*. For very small values of I_0, we can model the ejective eruptions (CME) by kink or torus instability in the second part of the thesis.

The initial density distribution is set to $\rho_o(x) = |B_0(x)|^{\frac{3}{2}}$. All simulations start from rest $u_o = 0$ at $t = 0$ except for an initial small upward velocity perturbation which is slightly varied according to the initial twist of the flux rope Φ and is applied only in a sphere of radius a at the flux rope apex as in Török & Kliem (2005). This yields a slow decrease of the initial Alfvén velocity v_A, from the strong-field regions (flux rope and sunspots) in the TD model. Specifically, this choice yields a height dependence of $v_A(0, 0, z, 0)$ very similar to the observationally inferred one in Vršnak et al. (2002) and is in agreement with Dulk and McLean (1978).

2.6.1 The Boundary Conditions

Closed boundaries are used in this work as done in Török & Kliem (2003) and Török & Kliem (2005), except for the converging motions in chapter (5) which are applied in the first layer of grid points $z = 0$. These closed boundaries at the top, bottom and side edges of the simulations box are implemented by specifying $\boldsymbol{u} = 0$ in the boundaries.

The line symmetric boundary conditions about the z-axis are realized by the mirroring the variables as

follows

$$\begin{aligned}
\rho(x,-y,z) &= \rho(-x,y,z),\\
B_x(x,-y,z) &= B_x(-x,y,z),\\
B_y(x,-y,z) &= B_y(-x,y,z),\\
B_z(x,-y,z) &= -B_z(-x,y,z),\\
u_x(x,-y,z) &= -u_x(-x,y,z),\\
u_y(x,-y,z) &= -u_y(-x,y,z),\\
u_z(x,-y,z) &= u_z(-x,y,z),
\end{aligned}$$

At the bottom of the simulation box, $k < 3$ for $z < 0$, the tangential components of the magnetic field, $B_{x,y}$, are obtained by extrapolation, as follows

$$\partial_z B_{x,y}(x,y,0) = \frac{B_{x,y}(x,y,\Delta z) - B_{x,y}(x,y,-\Delta z)}{2\Delta z} \tag{2.9}$$

where $\partial_z B_{x,y}(x,y,0)$ is computed as the one-sided derivative, using four points $i = 0,1,2,3$ (third-order interpolating polynomials)

After finding the value of $\partial_z B_{x,y}(x,y,0)$, the values of $B_{x,y}(x,y,-\Delta z)$ at the ghosts layer are obtained as

$$B_{x,y}(x,y,-\Delta z) = \frac{11}{3}B_{x,y}(x,y,0) - \frac{5}{3}B_{x,y}(x,y,\Delta z) + \frac{9}{3}B_{x,y}(x,y,2\Delta z) - \frac{2}{3}B_{x,y}(x,y,3\Delta z) \tag{2.10}$$

Since we integrate the ideal MHD equations, this implies that the normal field component B_n, is preserved throughout our simulations in all boundaries; staying $B_z(z=0)$, in particular, it is determined from $\nabla\cdot\boldsymbol{B}(z=0) = 0$.

CHAPTER 3

Helical Kink Instability in a Confined Solar Eruption

These results were published as A. Hassanin & B Kliem, Astrophys. J. 832:106 (2016)

A model for strongly writhing confined solar eruptions suggests an origin in the helical kink instability of a coronal flux rope which remains stable against the torus instability. In this chapter, the model is tested against the well observed filament eruption on 2002 May 27 in a parametric MHD simulation study which comprises all phases of the event. Good agreement with the essential observed properties is obtained. These include the confinement, terminal height, writhing, distortion, and dissolution of the filament, and the flare loops. The agreement is robust against variations in a representative range of parameter space. Careful comparisons with the observation data constrain the ratio of the external toroidal and poloidal field components to $B_{\rm et}/B_{\rm ep} \approx 1$ and the initial flux rope twist to $\Phi \approx 4\pi$. Different from ejective eruptions, two distinct phases of strong magnetic reconnection can occur. First, the erupting flux is cut by reconnection with overlying flux in the helical current sheet formed by the instability. If the resulting flux bundles are linked as a consequence of the erupting rope's strong writhing, they subsequently reconnect in the vertical current sheet between them. This reforms the overlying flux and a far less twisted flux rope, offering a pathway to homologous eruptions.

3.1 Introduction

Erupting magnetic flux on the Sun often remains confined in the corona without evolving into a coronal mass ejection (CME). The rise of the flux then halts and any embedded filament or prominence material slides back to the bottom of the corona along the magnetic field lines (Ji et al., 2003). Confined and ejective eruptions begin similarly (Moore et al., 2001); both forms are usually associated with a flare. Their initially accelerating rise indicates the onset of an instability. Confined (or "failed") eruptions present an important testbed for theories of solar eruptions. Understanding what prevents an evolving eruption from becoming ejective is also relevant for the study of the space weather and its terrestrial effects (Gosling, 1993; Webb et al., 2000).

In eruption models based on ideal MHD instability (van Tend and Kuperus, 1978), confinement results when the condition for the torus instability (in general terms: a sufficiently rapid decrease of the coronal field with height) is not met at or above the eruption site. This is possible if the eruption is caused by the onset of the helical kink instability in the stability domain of the torus instability (Török and Kliem, 2005). If the helical kink saturates before the rising flux reaches the height range where the torus instability can act, then the eruption remains confined; otherwise a CME results. Another possibility arises if the coronal field is structured such that the condition for the torus instability is fulfilled in two separate height ranges enclosing a stable height range, as has been found, e.g., by Guo et al. (2010) and Xue et al. (2016). If slowly rising current-carrying flux reaches the lower unstable range, it erupts due to the torus instability, but is halted in the stable height range.

Another model for confined eruptions suggests that the reconnection of two magnetic loops may yield two stable new loops, while producing a flare due to the release of magnetic energy during the reconnection (Nishio et al., 1997; Hanaoka, 1997). Observational support for this model was based on low-resolution data, which did not clearly reveal the nature of the interacting loop-shaped structures (Green et al., 2002). Coronal magnetic loops are no longer considered to contain sufficient free magnetic energy to power an eruption, rather the much larger amount of flux and free energy typically contained in a filament channel appears to be required. The suggested scenario indeed occurred in an event that showed the reconnection between two filaments (Török et al., 2011b; Joshi et al., 2014a). A CME was associated, but must have originated in the perturbed flux overlying the filaments which remained in place. Jiang et al. (2013,2014) reported partly similar (more complex) failed filament eruptions (Jiang et al., 2013, 2014b). Overall, events of this category are very rare.

The confinement of eruptions may also be related to the existence of a coronal magnetic null point which spans a dome-shaped magnetic fan surface above the eruption site. In the case of an eruption, the footprint

of the fan surface yields a circular flare ribbon (Masson et al., 2009). This configuration has been found to be associated with both confined eruptions (Wang and Liu, 2012; Deng et al., 2013; Vemareddy and Wiegelmann, 2014; Kumar et al., 2015) and ejective ones (Liu et al., 2015; Joshi et al., 2015; Kumar et al., 2015). Therefore, the fan surface of a coronal magnetic null does not appear to be the primary factor deciding the ejective vs. confined nature of eruptions launched under it. In fact, reconnection at the null may facilitate the removal of overlying, stabilizing flux (Sun et al., 2013; Jiang et al., 2014a).

Observational studies of confined eruptions have become quite frequent with the recent advances of observing capabilities (Liu et al., 2009, 2014; Shen et al., 2012; Netzel et al., 2012; Chen et al., 2013; Kuridze et al., 2013; Joshi et al., 2014b; Kumar and Cho, 2014; Kushwaha et al., 2014, 2015; Song et al., 2014; Yang et al., 2014; Cheng et al., 2015; Xue et al., 2016). Statistical studies of their association with source region structure and flare magnitude were also performed (Wang and Zhang, 2007; Cheng et al., 2011). Despite the large variety of these events, several trends are apparent. Strong overlying flux is typically observed, and for several events it was demonstrated to possess a height profile that prevents the torus instability. Naturally, this favors the central part of active regions above their periphery. Indications of the helical kink and the dissolution of embedded filaments are often found. Confinement also shows an association with the magnitude of energy release by the eruption, with only a minor fraction of the B-class flares but nearly all >X1-class flares being accompanied by CMEs. The underlying cause-effect relationship, i.e., whether the confinement limits the flare magnitude or an insufficient flare energy release prevents the eruption from developing into a CME, is not yet clear. However, since there are about three orders of magnitude between the weakest CME-associated flares (in the low-B-class range) and the strongest confined flare, the flare magnitude cannot be decisive by itself but must be considered in the context of the source region's magnetic structure, particularly the properties of the overlying flux.

Occasionally, even eruptions producing X3 flares can remain confined, as in the exceptional active region (AR) 12192. Insufficient magnetic shear, twist or helicity in the AR's core field and overlying flux preventing the torus instability have been suggested to be the possible causes of confinement in this region (Thalmann et al., 2015; Sun et al., 2015; Chen et al., 2015; Jing et al., 2015; Inoue et al., 2016; Liu et al., 2016a). Since a strong eruption (the X3 flare) occurred in the first place, confinement by the overlying flux appears to be the most obvious explanation.

In this chapter we present a simulation study of the confined filament eruption on 2002 May 27, whose detailed and comprehensive observations were analyzed by Ji et al. (2003) and Alexander et al. (2006). The initial phase of the eruption, up to the point the rising flux reached its terminal height, was already modeled by Török & Kliem (2005) and Török & Kliem (2005). Using a flux rope susceptible to the helical

kink mode but not to the torus instability as the initial condition in their MHD simulations, the rise profile of the flux rope apex, the rope's developing helical shape, and its distortion during the deceleration showed close agreement with the observations. Thus, the helical kink instability appears to be the prime candidate mechanism for this event. Our simulations substantiate this model for confined eruptions in two ways. First, we extend the computations to model the whole event, and second, a parametric study suggests that the requirement on the initial twist can be relaxed to about 4π, which is closer to twist estimates for other events than the estimate of $\approx 5\pi$ by TK05. We also focus on the magnetic reconnection, demonstrating that it occurs in two distinct locations and phases which correspond to the observed brightenings and changes of topology, and consider the fate of the erupting flux, which can reform a (less twisted) flux rope.

3.2 Observations

The eruption of a filament in AR 9957 near the west limb of the Sun on 2002 May 27 commencing at about 18 UT is a classical case of a confined event. Detailed analyses of the EUV observations by *TRACE* (Handy et al., 1999) and X-ray observations by *RHESSI* (Lin et al., 2002) were presented in Ji et al. (2003) and Alexander et al. (2006), so that here we only give a brief summary of the most relevant observations. The filament was observed by *TRACE* in the 195 Å band at high resolution (of 0.5 arcsec per pixel) and cadence (of up to 9 s). A strong writhe develops during the rise, resulting, for the given perspective of the observer, in an inverse-gamma shape. The filament reaches the peak projected height of 84.4 Mm at 18:09:31 UT, experiencing a strong distortion of its upper part, which is followed by the dissolution into a heterogeneous group of loop-shaped threads. The threads form new connections and eventually disappear to give way to a set of bright flare loops in the same place, appearing in the 195 Å band from 19:03 UT onward. After saturating the detector for $\gtrsim$ 10 min, they begin to turn into absorption at 19:17 UT. The *TRACE* observations of these characteristic phases are shown in Figure 3.1. There are no signs of a CME in the data of the LASCO coronagraph (Brueckner et al., 1995).

The accompanying soft X-ray (SXR) flare of *GOES* class M2.0 commences near 18:01 UT and reaches its peak at 18:10 UT (Figure 3.2). Hard X-rays (HXRs) observed by *RHESSI* are emitted from the very beginning of the filament's rise and peak at 18:06:40 UT in the 12–25 keV band. EUV brigthenings in the 195 Å band also commence simultaneously with the filament's rise and intensify from 18:04:30 UT, i.e., at about half of the rise. Initially, the strongest HXR sources and much of the brightest 195 Å emissions are located close to the rising filament, primarily at its top side. At about 18:06 UT the positions of these sources switch to the bottom of the corona along a line connecting the footpoints of the filament (see Figure 3.3

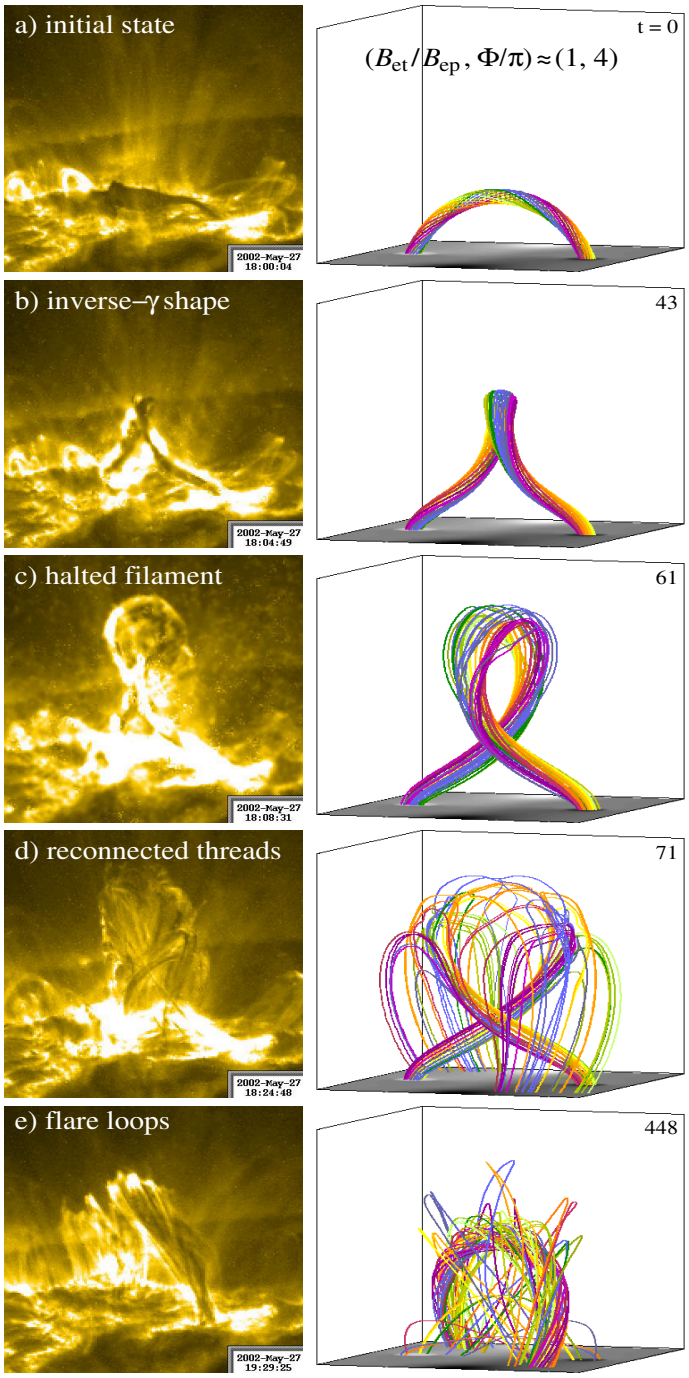

Figure 3.1: Characteristic stages of the confined filament eruption in AR 9957 on 2002 May 27 observed by *TRACE* at 195 Å (*left column*) compared with the best matching Case 1-4 of the parametric simulation study (*right column*). *TRACE* images are rotated by 90 deg. Magnetic field lines in the volume 5×5×4 in the center of the box are shown, and the magnetogram, $B_z(x, y, 0)$, is included in gray scale. The first four panels show field lines in the core of the kink-unstable flux rope (with start points on a circle of radius $a/3$ centered at the rope axis) and the final panel shows mostly ambient field lines that were first reconnected with, and subsequently disconnected from, the field lines shown above in the course of the two main reconnection phases.

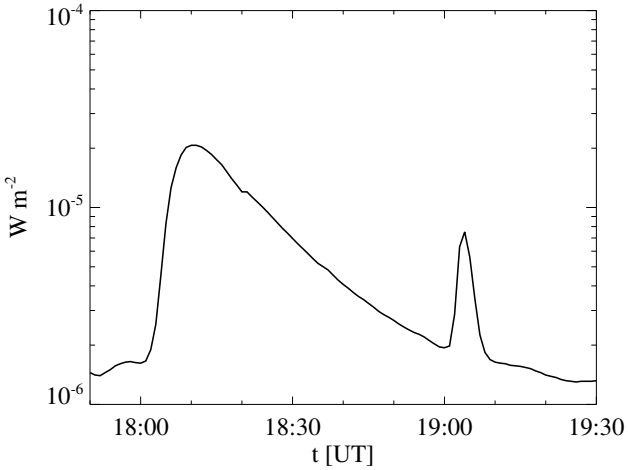

Figure 3.2: *GOES* soft X-ray light curve of the M2.0 flare associated with the eruption. An unrelated C7.5 flare originating at the east limb is superimposed after 19 UT.

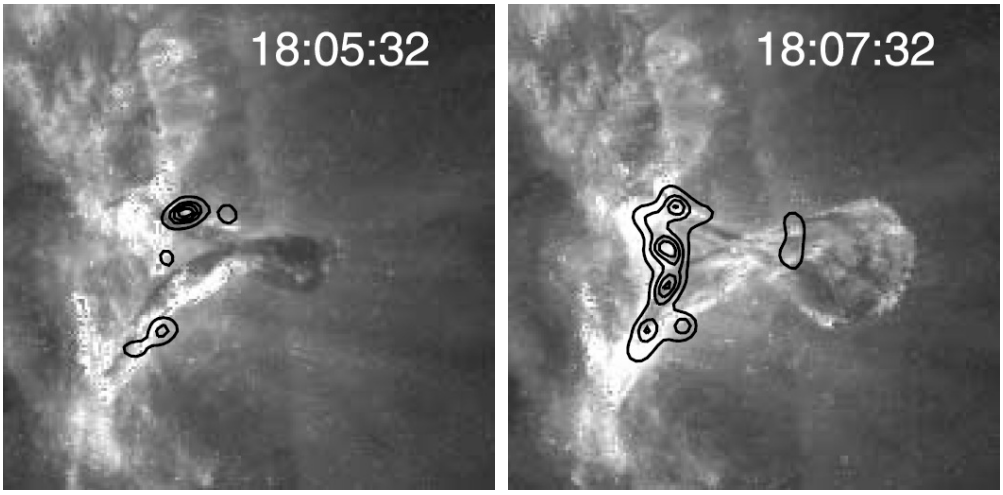

Figure 3.3: *TRACE* 195 Å and *RHESSI* 12–25 keV observations in the rise phase of the confined eruption ((with permission) from Alexander et al., 2006).

and the full image sequence in Alexander et. al (2006). Additionally, a weak HXR source, peaking nearly simultaneously with the 12–25 keV HXRs from the whole AR, occurs near the crossing point of the filament's legs (mostly slightly above the crossing point; also see Figure 3.3). This source stimulated the suggestion that the filament legs reconnected with each other in this eruption (Alexander et al., 2006). (Similar evolution of the HXR sources was observed in other strongly kinking filament eruptions (Liu and Alexander, 2009)). The band of bright EUV emission near the bottom of the corona (Figure 3.1(c)–(d)) does not evolve into a set of flare loops; such loops rather appear at greater heights of $\approx$ 35–50 Mm and only late in the event (Figure 3.1(e)).

The details of the photospheric flux distribution as well as the exact path and footpoints of the filament

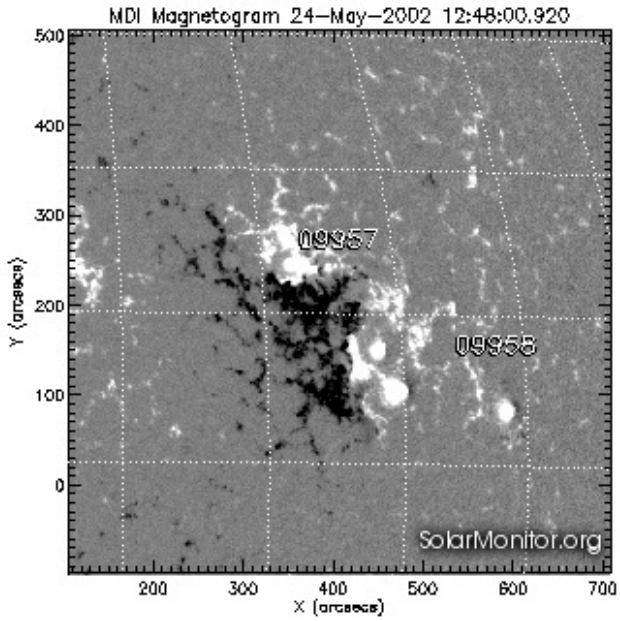

Figure 3.4: MDI line-of-sight magnetogram of AR 9957 (and the adjacent small AR 9958) on 2002 May 24, 12:48 UT.

are difficult to discern, due to the proximity to the limb. Figure 3.4 shows AR 9957 and the adjacent, near unipolar small AR 9958 on May 24, 3.25 days before the eruption. Both ARs are decaying, and the magnetograms from the MDI instrument Scherrer et al. (1995) near the time of the eruption indicate that no principal change of their structure occurs in the meantime, i.e., the changes appear to consist of the standard processes of flux dispersal and cancellation. Prior to the eruption, cool filamentary plasma can be seen in the *TRACE* 195 Å images along the whole polarity inversion line of AR 9957, but only the section at solar-$y \lesssim 230$ erupts. The 195 Å flare ribbons and flare loops are also exclusively formed along this section (Figure 3.1). Therefore, a bipolar source model appears justified. The southern footpoint of the erupting filament section is rooted in negative photospheric polarity, indicating right-handed field.

3.3 Numerical Model

As in TK05 we integrate the compressible ideal MHD equations in the limit of zero plasma beta and gravity,

$$\partial_t \rho = -\boldsymbol{\nabla} \cdot (\rho \boldsymbol{u}), \tag{3.1}$$

$$\rho \, \partial_t \boldsymbol{u} = -\rho \, (\boldsymbol{u} \cdot \boldsymbol{\nabla}) \, \boldsymbol{u} + \boldsymbol{J} \times \boldsymbol{B} + \boldsymbol{\nabla} \cdot \mathsf{T}, \tag{3.2}$$

$$\partial_t \boldsymbol{B} = \boldsymbol{\nabla} \times (\boldsymbol{u} \times \boldsymbol{B}), \tag{3.3}$$

$$\boldsymbol{J} = \mu_0^{-1} \, \boldsymbol{\nabla} \times \boldsymbol{B}, \tag{3.4}$$

using a modified Lax-Wendroff scheme (Török and Kliem, 2003). Here T denotes the viscous stress tensor ($\mathsf{T}_{ij} = \rho\,\nu\,[\partial u_i/\partial x_j + \partial u_j/\partial x_i - (2/3)\delta_{ij}\,\boldsymbol{\nabla}\cdot\boldsymbol{u}]$) and ν is the kinematic viscosity, included to prevent numerical instability. In the modified Lax-Wendroff scheme, the stabilizing, but rather diffusive Lax step is replaced by a small amount of so-called artificial smoothing (Sato and Hayashi, 1979), applied to $\boldsymbol{u}$ and ρ, but not to $\boldsymbol{B}$. This smoothing consists in replacing 5 percent of the value of the variable on each grid point by the average of its six neighbors after each iteration step (Török and Kliem, 2003). Although far less diffusive than the Lax step, which replaces the whole value of the variable, this level of smoothing suffices to prevent numerical instability even when the evolution becomes highly dynamic at small scales after the onset of magnetic reconnection. Reconnection occurs in the simulations due to the intrinsic numerical diffusion of the magnetic field in the second-order finite-difference scheme whenever current sheets steepen sufficiently. The simplifying assumption $\beta = 0$ is very well justified for eruptions that originate in active regions, where $\beta \sim 10^{-4}$–10^{-2} low in the corona (Gary, 2001). The neglect of gravity is justified as we do not attempt to model the return of the lifted filament plasma, which begins to slide back to the bottom of the corona along the field lines as soon as the rise phase of the eruption ends.

Similar to TK05, we use the Titov-Démoulin (TD) model of a force-free flux rope equilibrium in bipolar ambient field (Titov and Démoulin, 1999) as the initial condition. This approximate analytical equilibrium allows us to perform an extended parametric study. For the range of parameters considered here, force-free equilibrium is well approximated. The configuration consists of three elements. A toroidal current channel of major radius R and minor radius a, running in the center of a magnetic flux rope, is partially submerged such that the symmetry axis of the torus runs horizontally at depth d under the photosphere, which is represented by the bottom boundary of the computation box. The ring current I of the current channel carries a purely poloidal field, but inside the current channel both poloidal and toroidal components of field and current exist, as required by a force-free equilibrium. This structure models the filament. A pair of subphotospheric magnetic sources of strength $\pm q$, placed at the symmetry axis at distances $\pm L$ from the torus plane, provides the external poloidal field component, $B_{\rm ep}$ (occasionally called the "strapping field"), which enables the equilibrium by balancing the Lorentz self-force of the current channel (Shafranov, 1966). This yields two flux concentrations in the photosphere near the positions $x = \pm L$ which resemble the pair of main sunspots in a bipolar active region. Finally, an external toroidal field component, $B_{\rm et}$, is introduced by a line current I_0 running along the symmetry axis. This component models the shear field typically seen in active regions, in particular, the axial field of the filament channel that hosts the filament. The field by the line current is known to prevent ejective eruptions (Roussev et al., 2003; Török and Kliem, 2005; Myers et al., 2015), except for very small values of I_0. This feature is consistent with the present purpose of

modeling a confined eruption.

The initial density is set to $\rho_0(\boldsymbol{x}) = |\boldsymbol{B_0}(\boldsymbol{x})|^{3/2}$, also as in TK05. This scaling with the initial field, $\boldsymbol{B_0}(\boldsymbol{x})$, ensures a slow decrease of the Alfvén velocity, V_A, with distance from the flux concentrations, as is typical in the corona. In particular, the resulting height profile $V_\mathrm{A}(z)$ closely matches the coronal height profile inferred in Vršnak et al. (2002) from solar radio bursts emitted by coronal shocks (see their result for $\beta \ll 1$, perpendicular shock propagation, and five-fold Saito density). The system is at rest initially, except for a small initial velocity perturbation applied at the flux rope apex, which is detailed below.

The initial apex height of the toroidal axis of the current channel and flux rope, $h_0 = R - d$, the initial field strength B_0, density ρ_0, and Alfvén velocity V_A0 at that position, and the resulting Alfvén time, $\tau_\mathrm{A} = h_0/V_\mathrm{A0}$, are used to normalize the variables.

The computations are performed on a stretched Cartesian grid which resolves the volume $|x| \leq 5$, $|y| \leq 5$, $0 \leq z \leq 10$ with $141 \times 319 \times 505$ grid points such that the resolution is high ($\Delta = 0.02$) and nearly uniform in the central part ($|x| \lesssim 0.9$, $|y| \lesssim 2.8$) and gradually degrades toward the side boundaries but not with height. Closed boundaries are implemented throughout. The velocity is kept at zero in the bottom boundary to represent the photosphere; this keeps the normal component of the magnetic field in this boundary invariant.

3.4 Parametric Study

A twisted flux rope in force-free equilibrium is susceptible to two relevant modes of configuration change, both of which are referred to as a form of kink instability in the plasma physical literature. One of these is the torus instability. In the case of an arched flux rope, this primarily leads to an expansion of the rope in the major toroidal direction. Thus, it is a form of the lateral kink. The torus instability is primarily controlled by the height profile, or in full toroidal symmetry by the major radial profile, of the external poloidal field, parameterized by the decay index $n = -\mathrm{d}\,\log\,B_\mathrm{ep}(z)/\mathrm{d}\,\log\,z$. The critical (threshold) decay index lies between unity and about two (depending on various conditions), with a canonical value of $n_\mathrm{cr} \approx 3/2$ (Kliem and Török, 2006; Démoulin and Aulanier, 2010; Zuccarello et al., 2015).

The other relevant mode is the helical kink instability with azimuthal mode number $m = 1$, in the astrophysical literature often simply referred to as the kink instability. This instability is primarily controlled by the flux rope twist, here expressed as twist angle $\Phi(r) = lB_\phi/(rB_\zeta)$, where (r, ϕ, ζ) are local cylindrical coordinates referring to the magnetic axis of the rope and l is the rope length. For a line-tied flux rope, relevant in the solar atmosphere, the critical (threshold) value for the case of a uniformly twisted rope is $\Phi_\mathrm{cr} = 2.49\pi$ (Hood and Priest, 1981). Non-uniformity of the radial twist profile appears to raise the critical

average twist (Török et al., 2004) The modes with higher m in a force-free flux rope also appear to have a higher threshold (van der Linden and Hood, 1999).

If an external toroidal field component is present, the changing flux rope must bend and compress this flux. Hence, $B_{\rm et}$ acts stabilizing and raises the cited thresholds, which were obtained for $B_{\rm et} = 0$. Consequently, for appropriate values of $B_{\rm ep}(z)$, $B_{\rm et}$, and Φ, the flux rope can be in a kink-unstable but torus-stable equilibrium (where "kink" refers to the helical kink mode). This is the rationale of the model for confined eruptions by TK05.

Testing this model by comparison with a specific event should preferably include a parametric study which considers the variation of $B_{\rm ep}$, $B_{\rm et}$, and Φ within plausible ranges. A first such study was performed by TK05, who varied $B_{\rm et}$ and Φ. By changing the line current I_0, i.e. the strength of $B_{\rm et}$, they matched the terminal height of the kink-unstable flux rope to the observed value. For the resulting $B_{\rm et}$ the threshold value of the twist, averaged over the cross section of the current channel, is about 3.5π (Török et al., 2004). The closest agreement with the observed shape of the erupting filament was obtained for $\Phi = 5\pi$ (from varying Φ in steps of π).

In this chapter we extend the parametric study of TK05 by varying the strength of $B_{\rm et}$ (i.e., the line current I_0), the average twist Φ (i.e., the minor radius a for each selected I_0), and the spatial scale of $B_{\rm ep}$ (i.e., the source distance L). The force balance in conjunction with the normalization of field strength fixes the strength of $B_{\rm ep}$ at the position of the current channel for given R and a, but the spatial scale of $B_{\rm ep}$, i.e., its decay index, can still be varied (by varying L). Our strategy here is to consider I_0 and Φ as free parameters and change L, for each considered I_0 and Φ, until the ratio of terminal height, h_∞, and distance between the footpoints, $D_{\rm f} = 2(R^2 - d^2)^{1/2}$, matches the observation, $h_\infty/D_{\rm f} \approx 1.1$. For our chosen value of d/R (see below), this is equivalent to $h_\infty \approx 3.6h_0$. Since $B_{\rm ep}$ controls the torus instability, which is suggested to decide the confined vs. ejective nature of an eruption (Guo et al., 2010), this strategy appears to be the natural choice for the present task. The optimum I_0 and Φ are then determined by comparison with the further observed properties of the eruption. This yields a better founded estimate of the magnitude of $B_{\rm et}$ in the modeled event. In case a smaller $B_{\rm et}$ results, also a smaller Φ may match the data. Recent estimates of twist in erupting solar flux found values up to about 4π (Guo et al., 2013; Li and Zhang, 2015; Liu et al., 2016c)—not much but systematically smaller than the estimate in TK05, motivating us to address this option.

We consider line currents in the range $(0.4–1)I_{00}$, where $I_{00} = 4.5 \times 10^{12}$ A is the value used in TK05. The average twist is varied in the range $3.5\pi \leq \Phi \leq 5\pi$ in increments of $\pi/2$. For the geometry of the flux rope and the dimensional value of the sources of $B_{\rm ep}$ we adopt the values chosen in TD99 and TK05 to

represent an average solar active region, i.e., $R = 110$ Mm, $d = 50$ Mm, and $q = 10^{14}$ Tm^2. Given the fact that only the basic geometrical aspects of the complex field in AR 9957 can be approximated by the TD model, we leave the laborious option of additionally varying the geometry, i.e., increasing d/R to obtain a flatter flux rope, for future work (see Section 3.5.3 for a brief discussion). It should be noted that the normalization by B_0 changes the values of q, I, and I_0 by the same factor. Table 3.1 provides an overview of the I_0-Φ combinations analyzed in detail in the following. These exemplify the behavior of the system in the considered range of parameters. Parameter values obtained by scaling the simulation results to the observations, i.e., h_0, L, τ_A, and V_{A0}, are also given.

Table 3.1: Overview of the parametric study (see text for the further parameters of the equilibria). The length unit in the simulations is scaled to $h_0 = 23$ Mm for all cases. The ratio B_{et}/B_{ep} is given at the magnetic axis of the flux rope.

Case	I_0/I_{00}	a [Mm]	L [Mm]	B_{et}/B_{ep}	Φ	$n(h_0)$	τ_A [s]	V_{A0} [km s^{-1}]
1.4-4	1.0	21	105	1.37	4.0π	0.86	7.1	3400
1-5	0.7	19	120	1.03	5.0π	0.75	14.6	1500
1-4	0.7	22	140	1.15	4.0π	0.62	9.4	2600
1-3.5	0.7	25	140	1.15	3.5π	0.62	4.5	5200
0.8-4	0.4	23	170	0.80	4.0π	0.48	10.2	2300

All runs are started with a small velocity perturbation in order to exclude a downward kinking of the flux rope apex, which is preferred above the upward kinking by the TD equilibrium for some parameter combinations (Török et al., 2004). We prescribe a small upward-directed velocity in a small sphere of radius a centered at the apex of the flux rope for a few Alfvén times. The perturbation velocity is linearly ramped up from zero at $t = 0$ to a maximum and then simply switched off. For all runs with $\Phi \geq 4\pi$ the helical kink mode is weakly or moderately unstable and develops out of the numerical noise if the equations are simply integrated in time. The only function of the initial perturbation for these runs is to guarantee that the kink is directed upward. Uniform values of, respectively, 0.02 V_{A0} and $2\tau_A$ are chosen for the peak upward perturbation velocity and ramp-up time in these runs. For $\Phi = 3.5\pi$ the helical kink mode turns out to be stable for $I_0 = 0.7I_{00}$. Here the initial perturbation has the primary function to push the flux rope into the kink-unstable domain. The strength of the perturbation must be adjusted when L is varied for the matching of the observed terminal height; larger L values (i.e., stronger B_{ep} above the flux rope) require somewhat stronger perturbations. For the optimum L in this case, the perturbation is ramped up to 0.04 V_{A0} in $4\tau_A$.

3.5 Results

3.5.1 Confined Eruption Comprising two Phases of Reconnection

All simulations performed in this study yield a dynamic behavior in basic agreement with the key aspects of the observations throughout the event: (1) the writhing of the erupting flux according to the $m = 1$ helical kink mode which yields the observed shape, (2) the confinement at the observed height, (3) the subsequent dissolution of the erupting flux by reconnection with the overlying flux, and (4) the formation of the final loop arcade by a second phase of reconnection. A continuation of the simulation in TK05 (which is not presented here) yields the same basic agreement. In Figure 3.1 we show this for the Case 1-4 which matches the *TRACE* observations best. Quantitative information in the following description also refers to this case. Following the prescribed initial perturbation, the eruption starts with an exponentially growing rise (linear phase of the helical kink instability) up to $t \approx 40$. The characteristic helical shape develops clearly and in agreement with the observed inverse-gamma shape. This represents the conversion of flux rope twist into writhe of the rope's axis (Török et al., 2010). The corresponding rotation of the rope axis about the vertical reaches ≈ 60 deg. Both current sheets (see below) form in this phase, beginning already at $t \approx 2$.
Subsequently, the instability saturates, and the flux rope reaches its terminal height of $\approx 3.6h_0$ and maximum apex rotation of 120 deg during $t = 60$–65. The saturation occurs by the changing balance between the weakening tension and hoop forces in the twisted flux rope and the increasing back reaction from the pile-up of ambient flux, which steepens the well known helical current sheet in their interface [see Figure 3.5] (Gerrard et al., 2001; Kliem et al., 2010, 2014). The helical current sheet reaches a higher current density than the kinking current channel. The axial direction of the current in the helical sheet is opposite to that in the current channel, so that they repel each other. The rise of the flux rope also produces the vertical current sheet below the rope (Figure 3.5), which is known to be the prominent current sheet and a key element in ejective events Lin and Forbes (2000). The current in the vertical sheet attracts the rising current channel.

Reconnection plays an important role in the saturation of the instability (Figures 3.1, 3.6, and 3.7). It commences in both current sheets at $t \approx 50$, but initially intensifies more prominently in the helical sheet. We refer to this process as the *first reconnection phase*. In all runs we have performed, the flux rope reconnects with overlying ambient flux at various places in this current sheet and eventually is completely cut (at $t \approx 75$ in Case 1-4). The reconnection proceeds mostly at two symmetrical X-lines at the sides of the rising flux rope in its upper part (Figures 3.1(d) and 3.6(c)), but at times also just above the apex. The latter can be seen at its peak time from the z axis profiles in Figure 3.7(b), which show the steepened helical current sheet at $z = 3.6$ and its reconnection inflows. The complete reconnection of the flux rope eliminates

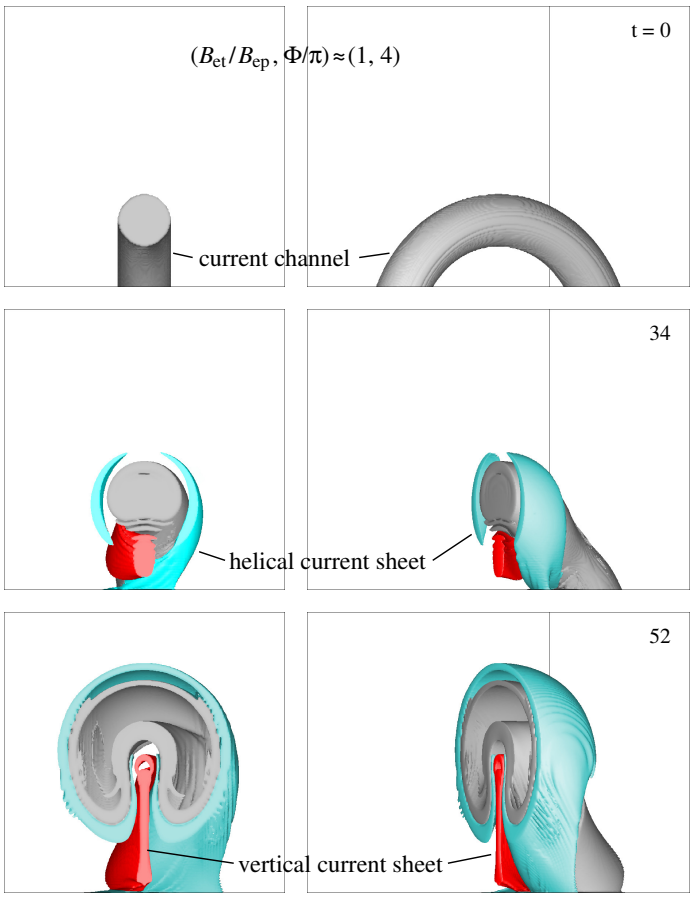

Figure 3.5: Isosurfaces of current density, $|\boldsymbol{J}|$, in Case 1-4, showing the current channel in the center of the TD flux rope (*gray*), the helical current sheet (*cyan*), and the vertical current sheet (*red*) in the volume $4\times4\times4$, each in a front view and a side view rotated by 60 deg. An isosurface level of, respectively, 6 and 4 percent of $\max(|\boldsymbol{J}|)$ is chosen for $t = 34$ and 52. With the exception of the side view at $t = 0$, all isosurfaces are restricted to the volume $\{y \geq 0\}$, to display the structure in the center of the system.

the driving forces of the rise.

The field lines reconnected in the helical current sheet are shaped like two linked hooks (Figure 3.6(c)). The linking is a consequence of the strong writhing (apex rotation); this will be discussed in Section 3.5.5 below. One side of each hook consists of a leg of the original flux rope, and the other side consists of originally overlying flux. Flux in the leg rotated backward in the view of Figure 3.1 now finds its other footpoint in front of the other leg which is rotated forward, and the situation is line-symmetrical with respect to the z axis for the other hook. Exactly this topology is shown by several filament threads in the *TRACE* observations, confirming the reconnection with overlying flux. Moreover, both the range of apex heights and the somewhat irregular arrangement of the new field lines, distributed around the center of the eruption, correspond well to the *TRACE* data. The new field lines show two directions of motion, toward the center of the system (z axis), which we address below, and downward. As the reconnection progresses, the outer,

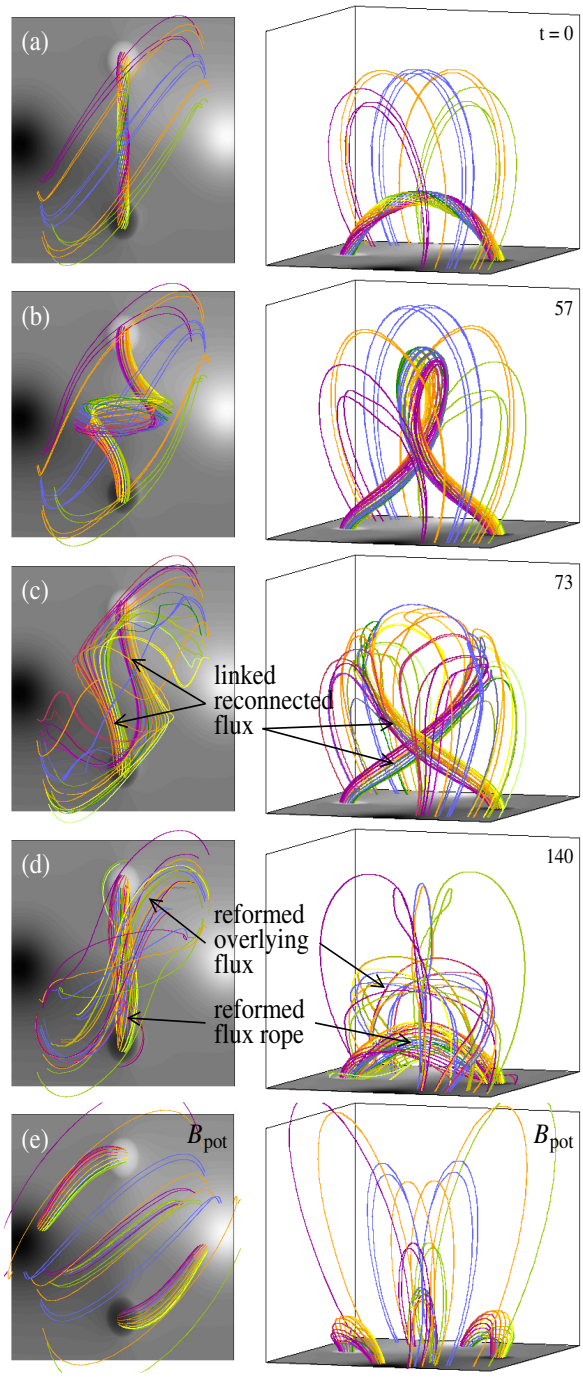

Figure 3.6: Overview of reconnection and necessity of the second reconnection phase in the considered model: (a) TD equilibrium for Case 1-4, (b) ideal phase of the helical kink instability (already during saturation), (c) two hook-shaped, linked flux bundles after the first reconnection, (d) reformed flux rope and overlying arcade resulting from the second phase of reconnection, and (e) the corresponding potential field. All field lines are traced from start points in the same fluid elements (mostly fixed in the bottom plane; the others moving with the top part of the unstable flux rope).

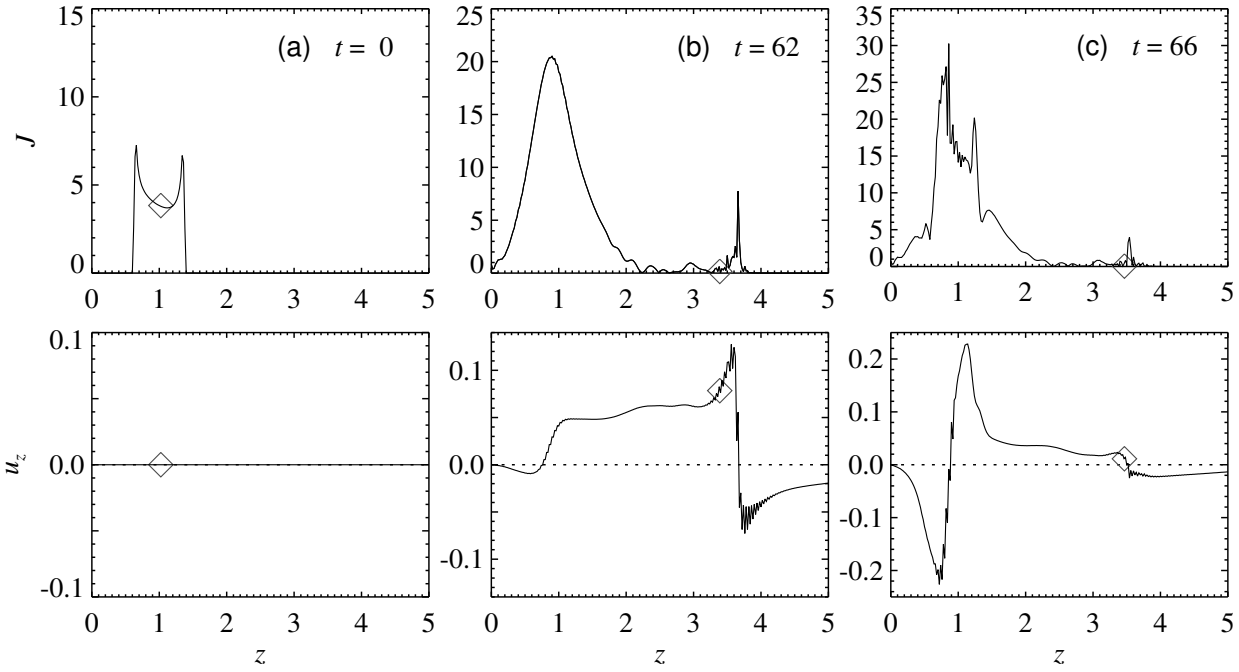

Figure 3.7: Profiles of current density $|\boldsymbol{J}|$ and velocity u_z at the z axis at characteristic times in Case 1-4, showing the current sheets and reconnection flows. The diamond marks the position of the fluid element initially at the apex of the flux rope's magnetic axis. (a) initial configuration, (b) time of peak reconnection rate in the helical current sheet, (c) time of peak reconnection rate in the vertical current sheet.

already reconnected parts of the erupted flux slide down on the surface of the still loop-shaped inner part, distorting the inner flux by dragging it out sideways and downward. This is very similar to the motion of the threads in the upper part of the erupted filament and the resulting distorted appearance.

It is worth emphasizing again that the reconnection of the flux rope with *overlying* ambient flux progressively *decreases* the flux content of the rope, up to its full destruction. The consequence of this reconnection is opposite to the classical "flare reconnection" of ambient flux in the vertical current sheet *under* a rising flux rope, which *increases* the flux in the rope (Lin and Forbes, 2000; Qiu et al., 2007; Vršnak, 2008; Janvier et al., 2014).

The further evolution of the two hook-shaped, linked flux bundles is shown in Figure 3.6(d). Since the axial currents in the flux bundles have the same main (toroidal) direction and the Lorentz force of bent flux points to the center of curvature, the bundles attract and approach each other, steepening the vertical current sheet in the center of the system, where reconnection of ambient flux is ongoing from $t \approx 50$. This leads to a *second phase of strong reconnection* when the legs of the original flux rope come into contact. The upward and downward reconnection outflows from the vertical current sheet strongly amplify during $t \approx 63$–100, with the peak values of current density and outflow velocity occurring around $t = 66$; see Figure 3.7(c). For the parameters of Case 1-4 this reconnection proceeds between the original flux rope legs. Such reconnection

is hardly ever observed in ejective eruptions, where, according to the standard picture, purely ambient flux reconnects in the vertical current sheet (Karlický and Kliem, 2010; Kliem et al., 2010). Since the attractive force of the linked flux bundles continues to act until they are fully reconnected, the necessary outcome is a reformed flux rope low in the volume. This rope is largely complete by $t \approx 115$, somewhat less coherent, and considerably less twisted than the original rope. The other two halves of the flux bundles, which are now reconnected, are both rooted in ambient photospheric flux. They straighten out as they are released from the vertical current sheet with the upward reconnection outflow, restoring the arch-shaped overlying flux at heights somewhat below the terminal height of the erupted filamen. This corresponds well to the considerable starting height and the late appearance of the observed flare loops.

Subsequently, reconnection in the vertical current sheet continues at a much lower, gradually decreasing rate. The outflow velocities soon fall into the 0.005–0.01 range, a factor ~ 20 below their peak values, and stay in this range for a long time. The reconnection is then no longer driven by the erupted flux rope and the current sheet continuously shortens. As a result, the overlying flux gradually adjusts its shape in a few 10^2 Alfvén times (compare Figures 3.6(d) and 3.1(e)).

From a more general perspective, the second reconnection can also be understood as a necessary element in approaching a state of lower energy. Figure 3.6(e) shows the magnetic connections between the four flux concentrations of the TD magnetogram in the corresponding potential field. The connections are flipped from the ones in the initial TD equilibrium (Figure 3.6(a)). The writhing of the unstable flux rope turns the legs into the opposite direction, however. In order to approach the potential field, the legs must turn back and reconnect a second time if they are linked after the first reconnection. We will consider this process and its variants for other parameters in more detail in Section 3.5.5.

3.5.2 Supporting EUV and HXR Observations

In addition to the basic agreement between observation and simulation found above, further specific aspects in the observation data compare favorably with the simulations. Most of these are found to support the model quite strongly, and the other ones appear at least consistent with the model. Figure 3.8 shows EUV snapshots that correspond to the first reconnection phase in the helical current sheet. The brightenings at various, changing locations indicate the occurrence of reconnection with overlying flux at locations similar to those in the simulations. The two brightenings marked in panel (c) are particularly persistent. Several reconnected filament threads appear at these locations (panel (d)), in agreement with the preferential reconnection at two X-lines at similar positions in the simulations. An indication of reconnection at a single X-line at the top of the structure is seen at the time of panel (a).

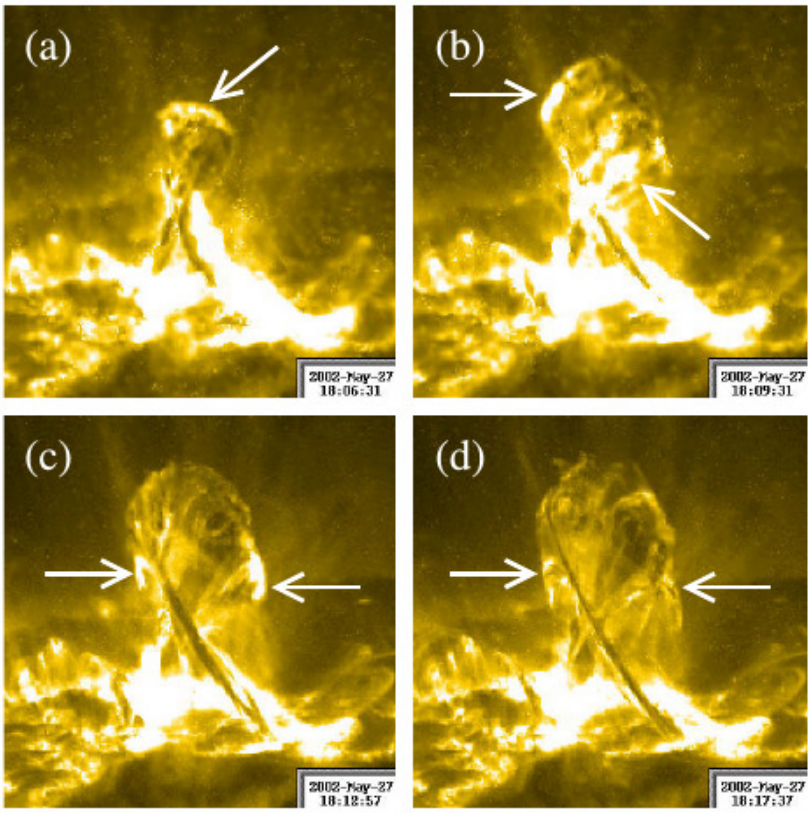

Figure 3.8: *TRACE* 195 Å images indicating that reconnection with overlying flux proceeds at various, changing locations, which are marked with arrows in (a)–(c). Reconnected filament threads appear at the position of such brightenings (d).

High current densities and the onset of reconnection in the helical current sheet are consistent with the observation of EUV brightenings and HXR sources near the surface and primarily on the top side of the rising filament (see Figure 3.1(b)–(c), Figure 3.3 at 18:05:32 UT Ji et al. (2003); Alexander et al. (2006)). The transition of the dominant reconnection in the simulations from the helical to the vertical current sheet corresponds to the transition of the main HXR and EUV sources from the legs of the rising filament to the bottom of the corona under the filament in the course of the rise (around 18:06 UT; see Figure 3.3 Alexander et al. (2006)), although reconnection in the helical current sheet likely continues to contribute to these emissions for some time.

Flare loops in ejective eruptions are formed below the reconnecting vertical current sheet. They typically appear in a continuous sequence, growing from rather small heights and footpoint separations and rather high shear to much larger, unsheared arcades of approximately semicircular loops. They begin to form early; even at the temperature of 1.5 MK mainly imaged in the 195 Å band they are often already seen during the impulsive rise phase. There is hardly ever any sign of twist in them. The flare loops in the considered event

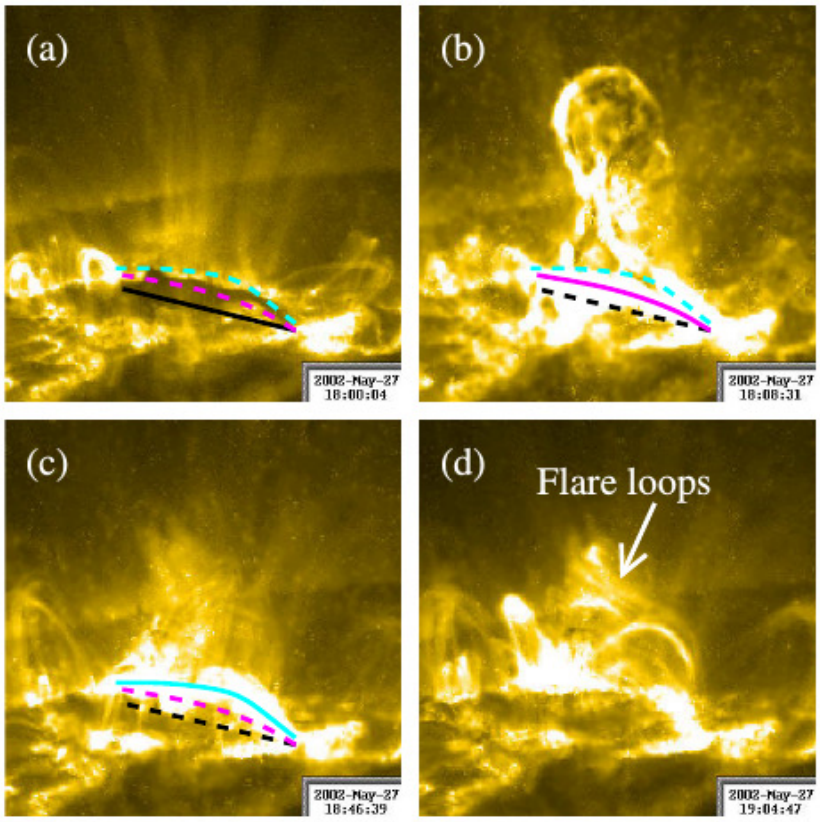

Figure 3.9: *TRACE* 195 Å images showing a rise of the brightenings under the erupted filament during the evolution of the disintegrated filament threads and the indication of initial S shape by the flare loops. (a) The visible filament end points prior to eruption are connected by a black line. (Note that the true left (northern) end point of the filament is likely located further westward.) (b) The brightenings before the filament threads reconnect are indicated by the magenta line. They are consistent with a location near the polarity inversion line under the filament. (c) The brightenings just before the reconnecting filament threads disappear, indicated by the cyan line, must have a higher position. (d) The set of dominant flare loops initially indicate an S shape similar to the reformed overlying flux in Figure 3.6(d).

appear at a considerable height and delay and show only a very minor subsequent rise. This is consistent with a formation above the reconnecting vertical current sheet in the second reconnection phase seen in the simulations. They show a change of shape from moderately S shaped to approximately semicircular (seen nearly edge on), which also corresponds to the simulation (see the initial shape in Figures 3.9(d) and 3.6(d) and the final shape in Figure 3.1(e)). Indications of twist become quite clear when the flare loops have cooled sufficiently (Figure 3.1(e)). This very unusual property is a natural outcome of the reformation process of overlying flux in our simulations because part of the original flux rope joins the reformed overlying flux (see Figure 3.6(c) and also Section 3.5.5).

The *TRACE* images also provide indications of reconnected flux low in the corona. The EUV brightenings under the erupted filament show an ascent during the time the disintegrated filament threads evolve and

the second reconnection is ongoing; see Figure 3.9. Whereas the HXR footpoint sources in Figure 3.3 (right panel) and the corresponding EUV brightenings in Figures 3.3 and 3.9(b) are consistent with a location at the bottom of the corona along the polarity inversion line under the filament, the EUV brightenings in Figure 3.9(c) are not. There is no reason to expect that the latter are displaced from the polarity inversion line to the degree that the figure would imply if they were located at the bottom of the corona. Hence, they must be elevated, indicating reformed flux that connects the original footpoints of the filament. Moreover, at times when the *TRACE* images are somewhat less saturated, these EUV brightenings resemble a collection of very low-lying loops. They remain bright throughout the phase reconnected filament threads are seen in the images ($\sim$ 18:10–50 UT, with the images during $\sim$ 18:50–19:03 UT being strongly distorted by particle hits on the detector in the Earth's radiation belts). Essentially, this is the decay phase of the SXR flare (Figure 3.2). The long decay of the SXR light curve clearly indicates ongoing reconnection.

The set of dominant EUV flare loops become visible after 19:03 UT, i.e., when the reconnection indicated by the SXRs and by the low-lying bright EUV structures significantly decreases. This is consistent with the picture obtained from the more recent multi-band EUV observations of flares with the *Solar Dynamics Observatory*, which show that flare plasmas are often heated to $T \geq 10$ MK before they cool to show flare loops at 1.5 MK in the 193–195 Å band. The low densities at the considerable height of the flare loops in the considered event imply long cooling timescales, making it plausible that the loops appear only when the reconnection decreases significantly. In contrast, the cooling is far more efficient at the higher densities of the low corona, where the bright 195 Å structures in Figure 3.9(b) and (c) appear throughout the second reconnection phase.

The second phase of reconnection indicated by these observations lasts much longer than the second phase of fast reconnection in the simulation. This is likely to result from the more irregular 3D arrangement of the reconnected filament threads (Figures 3.1(d) and 3.9(c)) compared to the hook-shaped reconnected flux bundles in the simulation (Figure 3.6(c)).

Some filamentary material reappears along the polarity inversion line under the erupted filament immediately after the event (Figure 3.1(e)). This is consistent with the reformation of a flux rope in the simulation, although the new structure is far less coherent than the original filament.

3.5.3 Matching of Shape

Proceeding to more quantitative comparisons between observation and simulation, we attempt to estimate the external toroidal (shear) field, $B_{\rm et} \propto I_0$, and twist, Φ, in the source region from the best match. First, the shapes of the structures formed by the eruption are compared with the corresponding shapes in the

simulation. Four characteristic shapes are identified in the *TRACE* data as displayed in Figure 3.1(b)–(e): (1) the inverse-gamma shape of the erupted filament which is formed by the fully developed helical kink instability; (2) the distorted upper section of the filament at the moment the terminal height is reached; (3) the disintegrated and reconnected filament threads resulting from the first reconnection in the helical current sheet; and (4) the flare loops resulting from the second reconnection in the vertical current sheet.

The reconnected filament threads are characterized by the first *TRACE* image that clearly shows two sets of reconnected threads with a leg in front of the erupted structure (18:24:48 UT). These new connections are traced by cool filament material draining down to the flare ribbon on the front side of the eruption site. (The extent down to the flare ribbon for these and further reconnected threads can be seen most clearly from the moving filament material in the animation of the *TRACE* data.) The selected time lies well within the interval the reconnected threads are seen or indicated in the data ($\sim$ 18:12–18:50 UT). They appear with apex points lying at the side of the erupted filament which still contains threads that extend up to the terminal height of the eruption and are most likely not yet reconnected. The apex points of the reconnected threads lie about halfway between the crossing point of the filament legs prior to their reconnection and the terminal height. The flare loops are characterized by the image at 19:29:25 UT which shows their final shape and the indications of twist most clearly.

Correspondingly, the field line plots to be compared with the reconnected filament threads are selected at a time a significant fraction of the field lines has reconnected in the helical current sheet and their new apex points lie about halfway between the crossing point of the flux rope legs and the terminal height of the eruption. This also clearly shows the location of their new footpoints. For the comparison with the flare loops we select a snapshot that clearly shows an arch-shaped collection of field lines in the reformed overlying flux near the position of the observed flare loops and no significant further change. For most of our cases, this is reached quite long after the reformation of the flux rope, because the overlying flux passes through many small adjustments of its shape under the influence of ongoing relatively slow reconnection in the vertical current sheet (see the animation accompanying Figure 3.1).

The field lines at $t = 0$ and for the first three characteristic shapes are all started from the same points in the bottom plane such that they show the flux of the rope within $r = a/3$. A choice of this magnitude is not only suggested by the thickness of the erupting filament in the first half of its rise, when it is not yet disintegrated and its thickness appears clearly, but also by the properties of a force-free flux rope. The condition of force-freeness couples the axial and radial length scales of the rope. For example, in a uniformly twisted rope, the radial length scale equals the pitch of the field lines. Thin flux ropes of moderate twist are possible if the twist profile peaks strongly at the axis of the rope (Liu et al., 2016c), but for filaments

in decaying regions like AR 9957, the current density and twist likely peak at the surface of the flux rope (Bobra et al., 2008). This is similar to the TD equilibrium [see Figure 3.7(a)]. Therefore, a weakly twisted flux rope of $\Phi \approx (3\text{–}5)\pi$ in AR 9957 should be considerably thicker than the observed filament (if the minor radius of the TD rope in our best matching Case 1-4 were reduced to $a/3$, the average twist would rise to 16π).

Moreover, the *TRACE* images give the impression that the filament threads run near the magnetic axis of the erupting structure, i.e., not only in the bottom part of a flux rope, as is often assumed in the literature. During about 18:12:30–18:26 UT the threads in the front leg are nearly straight and at times appear to wind about each other. Both properties are expected for flux near the axis of a flux rope, but not near its outer parts. The very good geometrical correspondence between the displayed field lines near the axis of the TD rope and the observed shapes of the filament supports this view.

The five cases are compared with the *TRACE* data in Figures 3.1 and 3.10, with the best matching Case 1-4 shown in Figure 3.1. Overall, all five cases show an excellent match of the inverse-gamma shape, a good to very good match of the shape when the maximum height is reached, and a relatively good match of the filament thread shapes during the phase of reconnection in the helical current sheet. Strong differences among the cases are only found for the prominent flare loops in the final stage of the event, which are relatively well matched only by Case 1-4 and roughly matched by three other cases.

Inverse-gamma shape. Since the inverse-gamma shape develops very well in all our cases, we pay attention to the fact that the southern filament leg shows a clear S shape. This feature was used in TK05 to fix the best matching flux rope twist to be $\Phi = 5\pi$ (the legs were rather straight for 4π and too helical for 6π and higher). As expected, Figure 3.10 shows that the S shape of the flux rope legs is more pronounced for higher Φ and lower $B_{\rm et}$. The Cases 1-5, 1-4, and 0.8-4 yield an excellent match.

Distortion of the halted filament. The distortion of the filament's upper section tends to develop most clearly for high $B_{\rm et}$ when the overlying flux resists the eruption strongly. We find it most pronounced in Cases 1-4 and 1-5 and in the case (1.4-5) studied in TK05. For the other three cases it develops as well, but only immediately after the end of the rise. We have also measured the height of the leg crossing point at the end of the rise relative to the terminal height. Here the *TRACE* data (0.35) are closely matched by Cases 1-3.5 (0.33) and 1-4 (0.32), quite well matched by Cases 1-5 (0.30) and 1.4-4 (0.40), and still reasonably matched by Case 0.8-4 (0.27).

Reconnected filament threads. All simulation runs match the observation data in the key feature: the new loops are formed in the distorted upper section of the erupted flux by reconnection with overlying flux. Differences are mainly found in the footpoint locations of the new loops. These clearly depend on the main

direction of the ambient flux, i.e., on the magnitude of $B_{\rm et}$, since $B_{\rm ep}$ is fixed at the initial flux rope position by the equilibrium condition and thus does not vary strongly among our cases in the volume immediately above the flux rope. The dominance of $B_{\rm et}$ in the overlying flux can clearly be seen in Case 1.4-4, where the outer legs of the new loops are strongly aligned in the toroidal (y) direction. As $B_{\rm et}$ decreases by the factors 0.7 and 0.4, this alignment changes progressively toward the x direction of $B_{\rm ep}$. The latter cases are in somewhat better agreement with the thread shapes observed by *TRACE*.

Flare loops. The main direction of the overlying flux influences the shape of the structures most clearly when this flux is reformed, becoming visible as flare loops. Here our cases differ most obviously. One or two prominent bundles of loops are formed at the end of each simulation run, but their main direction approximates the observed one preferably in the cases with $B_{\rm et}/B_{\rm ep} \approx 1$. The initial flux rope twist influences the resulting main direction of the flare loops as well, because it determines the writhing of the flux rope, and thus influences the steepening of the helical current sheet and location of the first reconnection. A moderate twist, i.e. Case 1-4 in Figure 3.1, yields by far the best match. The ratio of projected height and footpoint distance is ≈ 1.6 for the observed flare loops and ~ 1, ~ 1, ≈ 1.6, ~ 4, and $\gg 1$ for our cases (in the order they are listed in Table 3.1) from the field line plots in Figures 3.1(e) and 3.10(e).

A further geometrical property of interest is how the values of L obtained from matching the terminal height of the eruption (see Table 3.1) compare to the distance of the polarities in the source region. We roughly estimated the latter from the magnetogram on May 24 when the AR was located at about 25 deg west (Figure 3.4). The center of gravity of the flux distribution then had a distance of about 40 Mm from the unstable section of the inversion line for both polarities. Here the nearly unipolar neighboring AR 9958 was included because it certainly contributed to the flux passing over the filament. The value may have increased somewhat by the ongoing dispersal of the flux in the subsequent 3.25 days up to the eruption, but such minor change, which is difficult to estimate, is not important for our rough comparison. The L values obtained from the simulation runs are all considerably (2.5–4 times) larger. They clearly show the expected increasing trend for decreasing $B_{\rm et}$, reflecting the necessity of a more stabilizing $B_{\rm ep}$. It is not surprising that the TD model yields L values which are too large, because its toroidal geometry inevitably yields an initial flux rope apex height above the apex height of the observed flat filament if the ratio of terminal height and footpoint distance is scaled to the observed one. To prevent the onset of the torus instability, L must therefore be larger than observed. The initial height differs by a factor of ~ 1.5 (Figure 3.11). A flatter TD flux rope could lower the mismatch of L by a larger factor, since shape also matters for stability; in particular, line tying is stronger for a flatter rope. The mismatch is likely also due to the differences in the structure of the ambient field, which is far more complex in reality (compare the magnetograms in

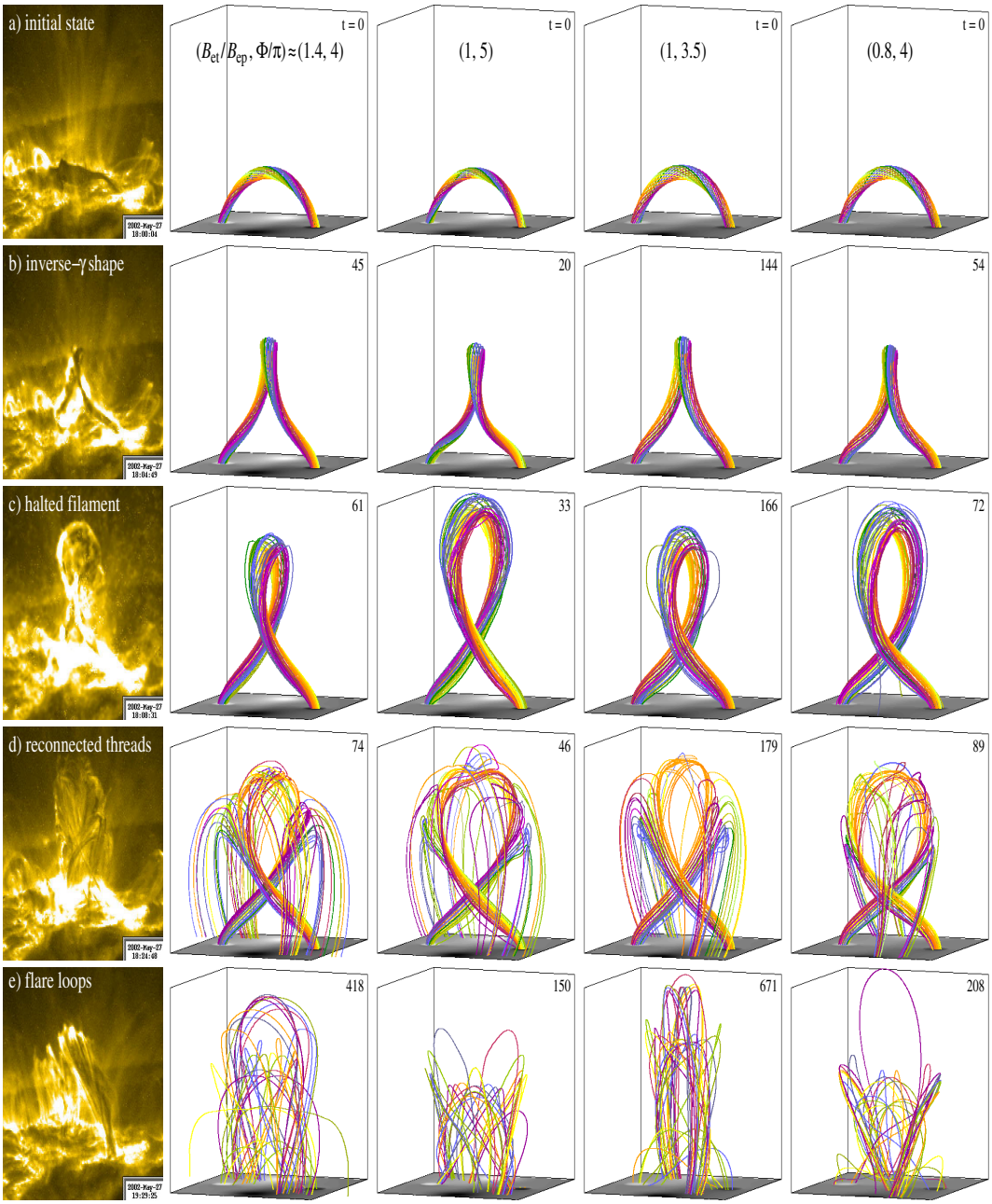

Figure 3.10: Characteristic stages of the eruption in *TRACE* 195 Å observations (*left column*), compared with cases 1.4-4, 1-5, 1-3.5, and 0.8-4 (*columns 2–5*). The format of the field line plots is identical to Figure 3.1.

Figures 3.4 and 3.6). The clarification whether a flatter TD rope (i.e., a larger value of d/R) can account for most of the mismatch in the value of L must be left for future work.

In summary, the observed shapes of the rising and halted (distorted) filament are well matched in a wide range of the parameters in the TD model. The appearance of the reconnected filament threads is best matched for the reduced line current values ($B_{\rm et}/B_{\rm ep} \lesssim 1$), whereas the observed distance of the photospheric flux concentrations tends to favor the higher line current ($B_{\rm et}/B_{\rm ep} = 1.4$). The observed flare loops are satisfactorily matched only by Case 1-4.

3.5.4 Scaling of the Simulations and Timing

Scaling to the Observed Rise Profile

Next we compare the timing of the different phases of the eruption between simulation and observation. This requires a scaling of the time unit in the simulations, $\tau_{\rm A}$, to the elapsed time in the observations and an absolute placement of a reference time in the simulations relative to a reference time in the observations. As in TK05, we use the rise profile $h(t)$ and its derivative $u_z(t)$, derived by Ji et al. (2003) from the *TRACE* images, for this purpose. From the simulation runs we extract the rise profile of the fluid element initially at the apex point of the flux rope's magnetic axis, which is a standard output. This height is slightly smaller than the upper edge of the group of field lines plotted in Figures 3.1 and 3.10 during the rise but reaches the same terminal value. The peak of this rise curve is also slightly delayed from the time of maximum field line height selected in Figures 3.1(c) and 3.10(c), because the fluid element experiences a short phase of additional upward acceleration (discussed below) when the upper edge of the flux rope is halted by the overlying flux. This delay is small, up to 90 s (in Case 1-3.5) and 40 s for our best matching case, and does not influence any of our conclusions. The reference time in the observation data is chosen to be the time the terminal height is essentially reached (18:08:31 UT, with 1 min and only 1 Mm of further rise remaining). As already mentioned above, the length unit in the simulation, h_0, is scaled by requiring $h_\infty/D_{\rm f} = 1.1$ which, for our chosen value of d/R, is equivalent to $h_0 \approx h_\infty/3.6 = 23$ Mm.

The result of the scaling is shown in Figure 3.11. All our five cases, as well as the case presented in TK05, reproduce the observed rise profile quite well. They all deviate weakly in the initial height, which is too high in the simulations due to the geometrical restriction of the TD model to a torus. The scaling yields the dimensional values for the distance of the photospheric flux concentrations, L, and for the Alfvén velocity in the source volume of the eruption, $V_{\rm A0} = h_0/\tau_{\rm A}$, which are listed in the figure and in Table 3.1.

The estimates of $V_{\rm A0}$ depend on the growth rate of the instability through the dimensional value of $\tau_{\rm A}$, which increases with increasing growth rate. Thus, $V_{\rm A0}$ decreases with increasing twist Φ and decreasing

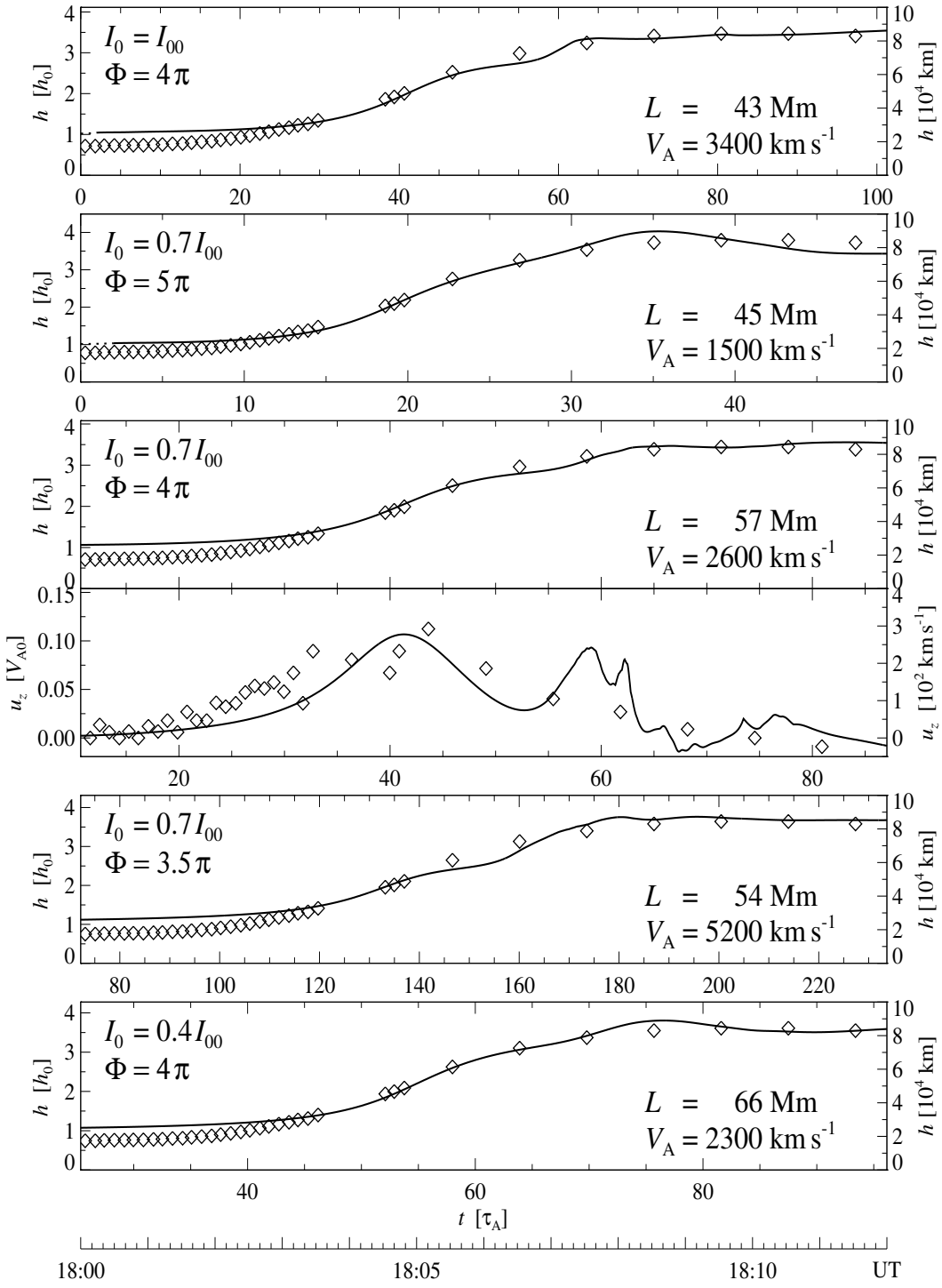

Figure 3.11: Scaling of the five cases to the observed rise curve of the filament apex. Diamonds show smoothed projected height data from Ji et al. (2003) and the derived velocities. 18:08:31 UT is selected as the reference time (see text). The small initial perturbation in the simulations is shown dotted.

external toroidal field $B_{\rm et}$. The Alfvén velocity in the low corona of active regions is not well known. Values in the range $V_{\rm A0} \sim$ 1000–2000 km s^{-1} are often quoted. However, values higher by a factor of 10 or even somewhat more appear realistic as well if typical field strengths and densities estimated from radio bursts low in the corona (Dulk and McLean, 1978) are adopted. Therefore, the estimates of $V_{\rm A0}$ must be considered acceptable for all our cases.

Timing of Instability Onset and Reconnected Structures

Since the scaling procedure uses the observed rise profile of the filament apex point, the phase of inverse-gamma shape and the arrival at the terminal height in the simulations are assigned the corresponding observation times. The resulting assignments for the onset time of the instability, formation time of the reconnected hook-shaped loops (reconnected filament threads), and reformation time of the overlying flux (flare loops) in the simulations can be used to check the simulations against the observations.

Onset time of instability. This yields a perfect match for Cases 1.4-4 and 1-5 and a slightly early onset of the instability by $\approx$ 1.5 min before the first height data point (at 18:00:04 UT) for Case 1-4, by $\approx$ 5.5 min for Case 1-3.5, and by $\approx$ 4 min for Case 0.8-4. This comparison is not a sharp discriminator between our cases because the initial development of the filament is very slow, so that the onset time of the rise in the *TRACE* data cannot be determined sufficiently precisely. A similar judgment results if the typical coupling between CME acceleration and flare X-ray emission Zhang and Dere (2006) is considered. A very close coupling would favor our first three cases. However, Bein et al. (2012) found that the CME acceleration onset precedes the onset of the SXR flare emission in about 75 percent of all events with an average difference of 4–5 minutes. The differences obtained from our scalings stay in this range (Bein et al., 2012).

Formation time of reconnected filament threads. As discussed in Section 3.5.3, we use the time the reconnected threads are first seen clearly on the front side of the erupted flux (18:24:48 UT, which is about one third into the time range reconnected threads are visible), and the corresponding time in the simulations is given by the selections for Figures 3.1(d) and 3.10(d). It should here be kept in mind that the latter times refer to the progress of reconnection near the axis of the flux rope ($r \leq a/3$), while reconnection commences much earlier at the periphery of the rope ($r = a$). The simulation time elapsed from 18:00:04 UT and the ratio of the elapsed times are given in Table 3.2. The elapsed times in the simulation are shorter by factors of $\sim$ 2.5, i.e., the kink-driven reconnection in the helical current sheet proceeds much faster than in reality. We conjecture that the perfect coherence of the TD flux rope is the main reason for this difference. The observed filament is far from being so coherent, as is most clearly seen from the arrangement of the reconnected filament threads which result from the reconnection in the helical current sheet. There is a

weak trend for the cases with the higher growth rates to match better. However, the differences between the cases are much smaller than their difference to the observations; hence, they are insufficient for favoring some cases above the others.

Table 3.2: Timing of the reconnected filament threads. The observation time is $t_{\rm obs}$ =18:24:48 UT. The corresponding simulation time elapsed from 18:00:04 UT, $\Delta t_{\rm sim}$, dimensionless and scaled, and the ratio of elapsed times, $\Delta t_{\rm sim}/\Delta t_{\rm obs}$, are listed.

Case	$\Delta t_{\rm sim}$ [$\tau_{\rm A}$]	$\Delta t_{\rm sim}$ [s]	$\Delta t_{\rm sim}/\Delta t_{\rm obs}$
1.4-4	74	524	0.35
1-5	46	673	0.45
1-4	61	571	0.38
1-3.5	106	474	0.32
0.8-4	64	648	0.44

Table 3.3: Timing of the flare loops relative to 18:00:04 UT. The observation time is $t_{\rm obs}$ =19:10:41 UT.

Case	$\Delta t_{\rm sim}$ [$\tau_{\rm A}$]	$\Delta t_{\rm sim}$ [s]	$\Delta t_{\rm sim}/\Delta t_{\rm obs}$
1.4-4	412	2930	0.69
1-5	150	2190	0.52
1-4	438	4130	0.97
1-3.5	599	2670	0.63
0.8-4	183	1860	0.44

Table 3.4: Timing of the flare loops relative to 18:24:48 UT. The observation time is $t_{\rm obs}$ =19:10:41 UT.

Case	$\Delta t_{\rm sim}$ [$\tau_{\rm A}$]	$\Delta t_{\rm sim}$ [s]	$\Delta t_{\rm sim}/\Delta t_{\rm obs}$
1.4-4	338	2410	0.87
1-5	104	1520	0.55
1-4	377	3560	1.29
1-3.5	492	2200	0.80
0.8-4	119	1210	0.44

Formation time of flare loops. We use the time the flare loops are first seen clearly in their whole extent down to the prominent flare ribbons. This is the case at 19:10:41 UT (earlier than the time of the *TRACE* image in Figures 3.1(e) and 3.10(e), which best displays the internal structure of the flare loop arcade, as explained in Section 3.5.3). Subsequently, apart from a very minor, gradual increase in height, there is no significant change in the position and shape of the flare loops. The corresponding times in the simulations are given by the selections for Figures 3.1(e) and 3.10(e). The results from the scaled simulations are compiled in Table 3.3 in the same format as in Table 3.2. Again, the times elapsed in the simulation are shorter, but here the mismatch is significantly smaller. The mismatch tends to be reduced further by referring to the observed formation time of the reconnected filament threads, 18:24:48 UT. This is compiled in Table 3.4

and yields agreement with the observations to within 30 percent for the Cases 1.4-4, 1-4, and 1-3.5. This latter comparison refers exclusively to the long phase of weakly driven and relatively slow reconnection in the vertical current sheet, which gradually completes and shapes the reformed overlying flux in the simulation (Section 3.5.1) and is indicated by the gradual decrease of the SXR flux in the observations (Figure 3.2).
The preceding phase of strongly driven, fast reconnection in the vertical current sheet ($t \approx 63$–100 in Case 1-4 (Section 3.5.1)) roughly coincides with the interval of flux rope reformation in the simulation (up to $t \approx 115$ in Case 1-4). Unfortunately, the *TRACE* observations only provide tentative indications of a reformed flux rope (the brightenings in Figure 3.9(b) and (c) and the subsequent reformation of cool filamentary structures in the same place) without any clear hint on its timing. Therefore, the rate of fast reconnection in the vertical current sheet in the simulations cannot be quantitatively compared with the *TRACE* data.

Timing Comparison with the Hard X-ray Emissions

Further aspects of interest in timing comparisons are the *HXRs from the whole active region*, which at their peak time mostly originate from footpoint sources under the rising filament, and the appearance of a coronal HXR source near the crossing point of the filament legs. Our simulations do not include the acceleration of particles, but a link to the HXR emissions is given by the observation that the time of peak reconnection rate in eruptions is associated with the peak flux of the high-energy emissions (Qiu et al., 2004). It is clear that the bulk of the HXR-emitting electrons must originate in one or both reconnecting current sheets (helical or/and vertical) in the system. The 12–25 keV light curves for both source regions begin to rise early in the eruption (before 18:04 UT), peak in the late stage of the filament rise (18:06:40–18:07 UT), and gradually decrease subsequently (Alexander et al., 2006). Thus, the onset of reconnection and the time of peak reconnection rate are weakly delayed in the simulations. In Case 1-4 these times ($t \approx 50$ and $t \approx 62$–66) correspond to $\approx$ 18:06 UT and $\approx$ 18:08–18:09 UT, respectively.
Since reconnection depends on both global and local conditions (e.g., on the imposed inflow velocity and on the current sheet thickness), its onset and peak times depend more sensitively on the parameters in the system than the shapes formed by the erupting flux. In particular, the distribution of flux in the photosphere may play a critical role. AR 9957 shows flux concentrations near the polarity inversion line, whereas no such feature exists in the TD equilibrium. These flux concentrations may cause a faster steepening of the vertical current sheet, resulting in earlier onset and peak times of reconnection in this sheet. Similarly, inhomogeneities in the overlying flux, which certainly exist, may cause a stronger and earlier steepening of the helical current sheet in some places as compared to the simulations which use a smooth model field. This effect is indicated by the location of the first HXR sources and EUV brightenings at one position just on

top of the northern leg of the rising filament during ≈ 18:02–18:06 UT (see Figure 3.3 (left panel) and the animated *TRACE* images). Additionally, due to the numerical diffusion, the current sheets in the simulation may steepen less readily than the current sheets in the corona. Given these effects, we consider the timing of the fastest reconnection in our simulations to be in basic agreement with the timing of the main HXR emissions and EUV brightenings.

The *coronal HXR source* near the crossing point of the filament legs starts at a somewhat later time and intensifies more impulsively than the bulk of the HXR emission from the active region, indicating an independent origin. Alexander et al. (2006) suggested that the radiating electrons were accelerated by reconnection in the vertical current sheet between interacting filament legs. However, this process likely causes the bulk HXR emissions after their source locations switch from the rising filament legs to the bottom of the corona under the filament at ≈ 18:06 UT. A further argument against the suggestion comes from the fact that, for most of the time, the coronal HXR source is located somewhat above the crossing point, where neither the reconnection electric field (i.e., the acceleration) nor the ambient plasma density (i.e., the target density for the energetic particles) are expected to be maximal. The indications for particle acceleration by reconnection in the helical current sheet are strongest when the main HXR sources and most prominent EUV brightenings are located just on top of the rising filament legs, i.e., up to ≈ 18:06 UT, which precedes the peak of the coronal HXR source. Therefore, it is of interest whether there exist further effects that might have caused this source.

The simulations indeed show a special phenomenon in the right place and at the right time. This is a strong distortion of the inner part of the current channel, which emanates from the upper tip of the vertical current sheet. Figure 3.5 at $t = 52$ shows the situation when this process begins to develop strongly. The vertical current sheet extends into the current channel from below, such that the original circular cross section is strongly distorted. The resulting Lorentz force drives a further strong upward motion from the tip of the current sheet into the volume of the current channel, which is halted by the tension of the overlying flux at the helical current sheet about 10 Alfvén times later. This motion is visible in Figure 3.11 as a second peak of the apex velocity in Case 1-4 during $t = 52$–63 and in Figure 3.7(b) as an upward flow in the range $z \approx 2$–3, which is faster than the reconnection outflow in the range $z \approx 1$–1.5. The same phenomenon is clearly indicated by the $h(t)$ curves for the other cases (Figure 3.11), where it also occurs shortly before the terminal height is reached. Layers of alternating toroidal current direction (negative for the current channel and the vertical current sheet, positive for the helical current sheet) are here pushed together very closely and change their local configuration rapidly. The resulting induced electric fields may be responsible for the acceleration of the electrons whose emission is seen as the coronal HXR source.

Summary of Timing Comparisons

To summarize the comparison of the timing, all our simulations can be scaled to the observed rise profile of the eruption, resulting in a good match which is also consistent with known values of the Alfvén velocity in active regions. The further possible comparisons refer primarily to the progress of reconnection and yield a heterogeneous picture. Reconnection in the simulations commences somewhat later than in the observed event. However, as long as it is strongly driven by the helical kink, it proceeds considerably (2–3 times) faster. Both differences are likely due to the simplicity of the initial TD equilibrium, whose external field is much smoother and whose flux rope is much more coherent than the corresponding structures in AR 9957. The rather prompt shift of fast, driven reconnection from the helical to the vertical current sheet corresponds to the shift of the strongest HXR sources from the legs of the erupting filament to the bottom of the corona under the filament. The subsequent much slower, undriven reconnection in the vertical current sheet, which reforms and gradually adjusts the overlying flux, proceeds at a rate comparable to the observed one in three of our cases (1.4-4, 1-4, and 1-3.5), whereas it is too fast by a factor ~ 2 for the other two. In spite of the differences, the reconnection in the simulations appears to be in basic agreement with the observed timing (and source locations) of the HXR emissions and major EUV brightenings in the associated flare. The weak coronal HXR source slightly above the crossing point of the erupted filament's legs may be due to the strong distortion of the erupted flux by the upward-growing vertical current sheet.

3.5.5 Flux Rope Reformation

The reformation of the flux rope described in Section 3.5.1 occurs in the whole parameter range studied in this chapter; thus, it could be a typical phenomenon in confined eruptions driven by the helical kink instability. As is obvious from Figure 3.6, the process requires the reconnection of the erupted flux rope with overlying flux in such a way that two linked flux bundles result. This, in turn, requires a sufficient writhing of the erupting flux, such that the flux rope apex rotates (about the vertical) beyond the direction of the immediately overlying flux. It does not require that the reconnection with overlying flux occurs at two X-lines. Figure 3.12 illustrates that, after sufficient writhing, linked flux bundles are formed as well if the reconnection proceeds at only one X-line on top of the erupted flux. This can be traced to the fact that the reconnection outflows always align with the antiparallel component of the reconnecting flux.

For our best matching Case 1-4 with $B_{\rm et} \approx B_{\rm ep}$, the rotation must exceed $\approx \pi/4$, which is a rather modest requirement for the helical kink. Even if the external field is purely poloidal, passing nearly perpendicularly over the polarity inversion line (i.e., if shear field exists only within the current-carrying filament channel), the required rotation of $\gtrsim \pi/2$ can easily be reached by a well developed helical kink (Kliem et al., 2012).

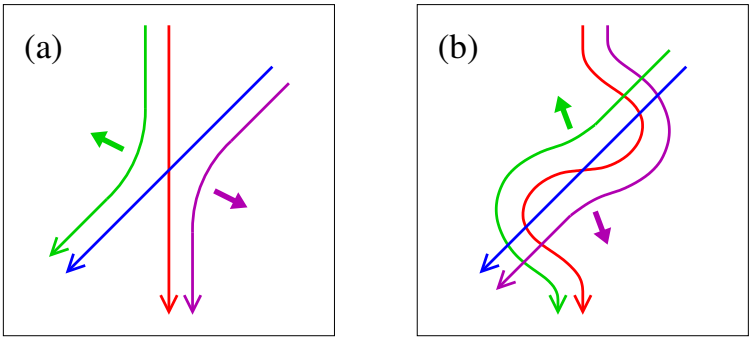

Figure 3.12: Schematic showing that linked flux bundles (green and magenta in (b)) result from reconnection of a rising flux rope (red) and overlying flux (blue) if and only if the flux rope writhes sufficiently, such that its top part rotates beyond the direction of the overlying flux. The reconnection outflow directions are indicated by filled arrows.

The reformation may be a pathway to a sequence of homologous flares that start with one or several confined eruptions and may include one ejective eruption (CME) at the end [as, e.g., in the events analyzed in Shen et al. (2011)]. More complex sequences are possible if erupting flux is only partly stopped in the corona, which is occasionally observed (Liu et al., 2007; Koleva et al., 2012).

Whether the torus instability can lead to the flux rope reformation process found here is not yet clear. Its requirement on the decay index implies a weaker pile-up of ambient flux above the unstable flux rope. Moreover, torus-unstable flux does not writhe considerably by itself. The presence of a sufficiently strong external toroidal field component leads to both stronger writhing (Isenberg and Forbes, 2007; Kliem et al., 2012) and flux pile-up, but also has a stabilizing effect. Therefore, further study will be required to determine the potential of the torus instability for the reformation of a flux rope.

No reformation was found in a previous simulation study of a kink-unstable flux rope which remained confined (Amari and Luciani, 1999). Quantitative information about the height profile of the ambient field in that simulation was not given, but, from the geometry shown and from the confinement of the unstable flux rope, one can expect that the ambient field prevented the torus instability from occurring. The flux rope reconnected with the overlying flux; however, different from our simulations, this resulted in two unlinked flux bundles. The reason for this difference lies in the chosen special orientation of the flux rope along the line between the main concentrations of the ambient flux.

A partial reformation occurs in our model if the legs of the erupted flux rope begin to reconnect with ambient flux before they complete their mutual reconnection, which can be expected if the ambient flux ($B_{\rm et}$ or $B_{\rm ep}$) is sufficiently strong. The effect begins to act when the line current is raised above our reference value, $I_0 > I_{00}$. It also occurs when the sources of $B_{\rm ep}$ (i.e., the sunspots) are closer to the polarity inversion line, leading to a stronger $B_{\rm ep}$ low in the volume. Both cases lie beyond the range of parametric study in this

chapter.

Rather small values of twist are found in the reformed flux ropes in the present study. Three of the four effects leading to this result are obvious from Figure 3.6. The initial twist is first lowered by conversion into writhe. Second, the remaining twist per unit length decreases inversely proportional to the increasing length of the flux rope (in Case 1-4, this is 2.4 times the initial length when the terminal height is reached). Third, only the twist in the two short sections below the crossing point of the legs is transferred to the reformed rope. Additionally, one can expect that the twist tends to equilibrate along each linked hook-shaped flux bundle between the first and second reconnection phases by propagating from the original flux rope leg to the untwisted, originally overlying flux. In Case 1-4 a twist of only $\approx 0.7\pi$ results.

Since the long section of the expanded flux rope above the crossing point becomes part of the reformed overlying flux, that flux necessarily inherits part of the twist in the initial flux rope. This is apparent in the final stage of the runs shown in Figures 3.1 and 3.10, most clearly for Cases 1-4 and 1-5.

3.6 Conclusions

(1) Using a kink-unstable force-free flux rope in equilibrium as the initial condition, the MHD simulations presented in this chapter achieve good agreement with the essential properties of the confined filament eruption in AR 9957 on 2002 May 27, as observed by the *TRACE* satellite in the EUV. These include (i) the confined nature of the eruption, (ii) its terminal height, (iii) the writhing of the erupting flux according to the $m = 1$ helical kink mode which yields the observed inverse-gamma shape, (iv) the dissolution of the erupting flux by reconnection with the overlying flux, and (v) the formation of the flare loop arcade, which shows indications of twist, by a second phase of reconnection. The agreement is obtained in a representative range of parameter space. This robustness supports the model for confined eruptions by TK05, which assumes a kink-unstable and torus-stable flux rope to exist at the onset of the eruption.

(2) Through quantitative comparisons with the observations, the performed parametric study constrains the ratio of external toroidal (shear) field component and external poloidal (strapping) field component to $B_{\rm et}/B_{\rm ep} \approx 1$ and the average twist in the initial flux rope to $\Phi \approx 4\pi$, in better agreement with recent twist estimates for other events than the estimate in TK05.

(3) Different from ejective eruptions (CMEs), the confined eruption triggered by the helical kink is found to comprise two distinct phases of strong reconnection. The first phase occurs in the helical current sheet and destroys the rising flux rope through reconnection with overlying flux (opposite to standard "flare reconnection" in ejective events). In the whole range of parameters studied here, this reconnection occurs

after a strong writhing of the erupted flux rope, such that the resulting two flux bundles are linked. This, in turn, causes the second phase of strong reconnection between the legs of the original flux rope in the vertical current sheet in the center of the system, which restores the overlying flux. Flare loops are formed in this flux above the vertical current sheet.

(4) The second reconnection also results in the reformation of a flux rope of similar or only moderately reduced flux. Although the twist is strongly reduced (to $\Phi < \pi$ in our simulations), the reformation offers a pathway to homologous eruptions, preferably if the sequence starts with one or several confined events and includes only one CME at the end.

3.7 Discussion

Of the five cases presented here, one eruption (Case 1-3.5) starts from marginal stability, three from weakly unstable equilibria, and one (Case 1-5) from a moderately unstable equilibrium. No principal differences in the general behavior of the five cases were found and all parametric trends discussed in Section 3.5 appear to be coherent across them. Therefore, although the magnetic field on the Sun will not jump across the marginal stability line right into the unstable domain of parameter space, it appears justified to study models that employ weakly or even moderately unstable equilibria (as, e.g., in TK05) if done with appropriate caution.

We have found that the reconnection rate in the numerical model can differ significantly, but not extremely, from the solar one, especially for reconnection strongly driven by an ideal MHD process. Reconnection driven by the helical kink, which pushes the unstable flux rope against the overlying flux, is too fast in the simulations by a factor 2–3. The subsequent undriven reconnection in the vertical current sheet overall proceeds at a rate comparable to (within 30 percent of) the observed rate for three of our five cases, including the best matching case, and is too fast by a factor ≈ 2 for the other cases. The rate of "flare reconnection" in a previous modeling of a weak ejective event, estimated to be ≈ 1.5 times lower than on the Sun (Kliem et al. 2013), fits into the picture. None of these rates is off by an order of magnitude or more, whereas the numerical diffusion of the code, although intentionally kept at the minimum allowed by the numerical scheme, exceeds the magnetic diffusivity in the corona by many orders of magnitude. It is obvious that the reconnection rate in solar eruptions must primarily be controlled by the large-scale motions of the unstable flux, which act as drivers of the reconnection inflows or outflows. These motions can be modeled with relatively high accuracy by an ideal MHD code, as our comparisons with the observed shapes and rise profile of the considered eruption demonstrate.

Comparing a parametric simulation study of an analytical model like the present one with the method of data-

constrained simulations (where the initial condition typically is a nonlinear force-free field model obtained from the observations by extrapolation or flux rope insertion), one finds specific strengths on either side. The parametric study allows one to disentangle—sometimes discover and often quantify—the relevant effects, isolating the most important ones and their trends. It often also allows matching the observations rather closely, like in the present investigation. Data-constrained modeling can potentially match the observations even better, since the model can account much better for the complexity of the solar field. Less effort for the computations and their analysis may be required. In some cases, new effects can be discovered which are absent in analytical models due to the simplicity of those models. Hence, the modeling strategies are complementary.

All eruptions in our parametric simulation study remain confined and show a strong rotation of the flux rope apex about the vertical. The rotation angles in the five cases in Table 3.1 all reach 120–160 deg. A strong apex rotation (reaching ~ 90 deg or higher) is also often observed in confined eruptions on the Sun, but is not a typical property of ejective eruptions. Both findings do not support the idea that a considerable apex rotation (as typically resulting from the helical kink instability) facilitates an ejective behavior of eruptions by locally aligning the erupting flux with the overlying flux, such that the erupting flux can pass through the overlying flux without having to open a large part of it (Sturrock et al., 2001). The observation and simulation results can be better understood if the cause-effect relationship is reversed. If an eruption is halted, then the magnetic tension of the erupting flux can no longer be relaxed by expansion but only by further writhing, resulting in a tendency for confined eruptions to develop a strong writhing.

CHAPTER 4

An Improved MHD Modeling of the Confined Filament Eruption

The results were published as Hassanin, Kliem & Seehafer, Astron. Nachr., 337, 1082, (2016).

This chapter presents an improved MHD modeling of the confined filament eruption in solar Active Region 9957 on 2002 May 27 which is done in the *chapter 3* by extending the parametric studies of the event in Török and Kliem (2005) and Hassanin and Kliem (2016). Here the initial flux rope equilibrium is chosen to possess a small apex height identical to the observed initial filament height, which implies a more realistic inclusion of the photospheric line-tying. The model is found to match the observations as closely as in the preceding studies, with the closest agreement again being obtained for an initial average flux rope twist of about 4π. Thus, the model for strongly writhing confined solar eruptions which assumes that a kink-unstable flux rope in the stability domain of the torus instability exists at the onset of the eruption's main acceleration phase is further substantiated.

4.1 Introduction

The numerical modeling by TK05 and HK16 realized only a relatively poor matching of the initial filament height, which was too high in the model by a factor of ≈ 1.3. Although this mismatch appears rather modest by number, the shape of the relatively high arching model flux rope implies a weaker effect of the photospheric line tying compared to reality. To see this, one can represent the flux rope by a section of

a torus and consider a flux surface at a certain radial distance a_1, from the toroidal axis. The flatter the rope, the larger the two end sections of the rope axis that are not fully enclosed by the flux surface. The field lines at radius a_1 in these sections are arch-shaped, i.e., they do not pass under the rope axis, different from the middle section of the axis. This arch-shaped flux realizes the stabilizing line tying effect, whereas the flux in the middle section contributes to the destabilizing hoop force. Therefore, we here complement the parametric study of HK16 in order to test whether the model can still yield a good match with the observation data if the line tying is included much more realistically. We submerge the center point of the toroidal flux rope deeper below the photosphere to obtain a flatter coronal rope section.

4.2 Numerical Model

All basic assumptions and the other numerical settings are kept the same as in TK05 and HK16. For a torus of major radius R with the center point submerged by depth d, the apex height of the toroidal axis is $h_0 = R - d$ and the footpoint distance of the coronal section is $D_\mathrm{f} = 2(R^2 - d^2)^{1/2}$. The projected initial and terminal apex heights of the filament in the considered event were determined by Ji et al. (2003) from the *TRACE* 195 Å images to be $h_0 = 17.4$ Mm and $h_\infty = 84.4$ Mm, respectively, giving $h_\infty/h_0 = 4.85$. These values are close to the true values because the event occurred close to the (west) limb and the rise did not indicate any strong non-radial direction. HK16 estimated $h_\infty/D_\mathrm{f} \approx 1.1$ from the *TRACE* images. Hence, $h_0/D_\mathrm{f} \approx 1.1/4.85 = 0.23$.

Let the quantity κ be defined by $\kappa = (2h_0/D_\mathrm{f})^2$. Inserting the expressions for h_0 and D_f into this definition and resolving for d/R gives $d/R = (1-\kappa)/(1+\kappa)$. The above observational estimates fix κ to a value of 0.21. Thus, $d/R = 0.66$. For the value of $R = 110$ Mm assumed in HK16, this yields $d = 72$ Mm, while actually a depth d of only 50 Mm was used in that study. Requiring further that h_0 matches the observationally estimated value, thus fixing both d/R and $R-d$, we obtain $R = 51$ Mm and $d = 33.6$ Mm.

4.3 Simulation of the Confined Eruption

In order to model the confined nature of the eruption, flux rope equilibria in the stability domain of the torus instability are considered. This requires that the external field, especially the external poloidal field, decreases sufficiently slowly with height at and above the initial flux rope position (Roussev et al., 2003; Kliem and Török, 2006). The vertical scale length of B_ep scales linearly with the "sunspot distance" L in the model, so that a sufficiently large value of L guarantees torus stability and confinement. For each L, the strength of B_ep at the position of the flux rope (at its magnetic axis) is determined by the equilibrium

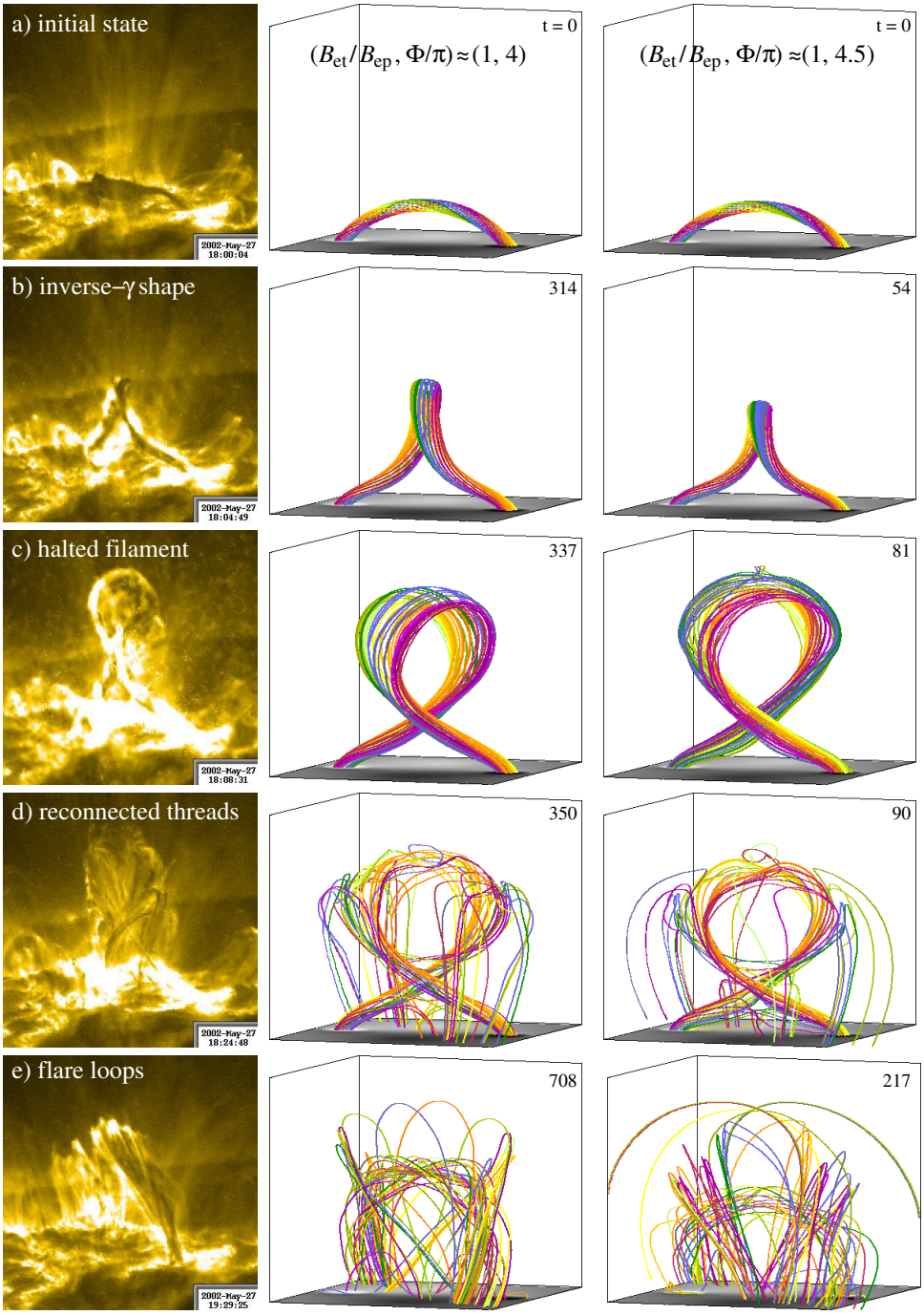

Figure 4.1: Comparison of the main features of the confined filament eruption at about 18 UT on 2002 May 27 in AR 9957 observed by *TRACE* at 195 Å (*left column*) with Cases 1 (*middle column*) and 2 (*right column*). Only the central part of the box, the volume 6^3, is shown. The magnetogram, $B_z(x, y, 0, t)$, is included in gray scale. The first four panels show magnetic field lines outlining the core of the kink-unstable flux rope (with starting points on a circle of radius $r = a/3$, centered at the apex of the rope axis). The fifth panel shows ambient field lines after the two main reconnection phases.

condition (see, e.g., TD99), which fixes q for given I, or vice versa. Thus, if the geometry of the flux rope (R and a) and the ring current I are set, q will be determined for each L such that $B_{\rm ep}$ at the magnetic axis attains the equilibrium value, which is given by R, a, and I but does not depend on L. However, different L yield a different decrease of $B_{\rm ep}$ with height, i.e., a different amount of overlying flux. There is a critical value $L_{\rm cr}$ for the onset of the torus instability, with instability for $L < L_{\rm cr}$. For $B_{\rm et} = 0$, one finds $L_{\rm cr} = R$ for the bipolar $B_{\rm ep}$ of the TD99 equilibrium if the canonical value for the critical decay index of the external poloidal field for the onset of the torus instability is used, $n = -{\rm d}\log B_{\rm ep}(R)/{\rm d}\log R = 3/2$. The critical value of L decreases for increasing $B_{\rm et} > 0$ (which acts stabilizing), but this dependence has not yet been quantified. Since the overlying flux decreases with decreasing L, the terminal height of an erupting flux flux rope increases with decreasing L.

The strength of $B_{\rm et}$ in the simulations presented here is taken to be the optimum one found in our previous extended parametric study of the event, given by $I_0 = 3.15\times10^{12}$ A. This yields $B_{\rm et}/B_{\rm ep} \approx 1$ at the magnetic axis of the flux rope.

In order to initiate an eruption and model the observed helical shape, the initial flux rope twist is set near the critical value for the onset of the helical kink instability. This value is $\Phi_{\rm cr} \approx 2.5\pi$ for a line-tied and uniformly twisted tube with $B_{\rm et} = 0$ (Hood and Priest, 1981; Einaudi and van Hoven, 1983), but rises for increasing $B_{\rm et} > 0$ and increasing non-uniformity of the radial twist profile. These parametric dependencies are not yet well known, especially the dependence on $B_{\rm et}$. Previous studies of line-tied, kink-unstable, arched flux ropes with aspect ratios $R/a \sim 2$–10 and a range of values for $B_{\rm et}$, both representative of erupting solar flux, suggest that the critical twist may typically be near the value $\Phi_{\rm cr} \approx 3.5\pi$ (Fan and Gibson, 2003; Török et al., 2004; Török and Kliem, 2005; Kliem et al., 2012; Hassanin and Kliem, 2016). Therefore, we ran the simulations with the initial twist set to $\Phi = 3.5\pi$, 4π, and 4.5π, which is accomplished by adjusting the minor radius a. These twist values are averaged over the cross section of the current channel. It turned out that, for the given geometry (a/R and d/R) and the given $B_{\rm et}$, the twist $\Phi = 3.5\pi$ lies well in the kink-stable domain of the parameter space, so that even a moderate upward initial velocity perturbation could not launch an eruption. Hence, here we present and compare the simulation runs with $\Phi = 4\pi$ and $\Phi = 4.5\pi$. The corresponding values $L = 30$ Mm and $L = 37$ Mm, respectively, were determined by trial and error such that the observed terminal height of the event is rather closely matched.

The range of initial twists considered here is consistent with the results of Guo et al. (2013); Li and Zhang (2015); Liu et al. (2016b), who found values up to about 4π in erupting solar magnetic flux. The parametric simulation study of the considered event in HK16 favored this same value but found reasonable agreement with the observations also for $\Phi = 4.5\pi$.

4.4 Results

4.4.1 Shapes Formed by Instability and Reconnection

The two simulation runs analyzed in this chapter are Case 1 with $\Phi = 4\pi$ and $L = 30$ Mm and Case 2 with $\Phi = 4.5\pi$ and $L = 37$ Mm. They are first compared with each other and with the *TRACE* observations based on the field line plots in Figure 4.1, where panels (a)–(d) show flux near the axis of the flux rope ($r \leq a/3$) and panel (e) shows ambient flux that has reconnected twice with the rope. The times for each case were selected such that the resulting shapes correspond to the four characteristic shapes that occurred in the event.

The helical deformation (writhing) of the rising filament first produced an *inverse-gamma shape* (Fig. 4.1(b)). Both cases match this shape quite well. The higher twist of Case 2 yields a slightly better match of the S-shape developed by the right (southern) filament leg.

As the eruption approached and reached its terminal height, a strong *distortion of the halted filament* occurred (Fig. 4.1(c)). The threads in the upper part of the filament were dragged to the side, which marked the beginning dissolution of the filament. The distortion results from the sideways oriented outflows of the beginning reconnection with the overlying flux at the top of the filament loop (TK05; HK16). Both cases match the terminal height and show the distortion. Case 1 shows it slightly more clearly and also reproduces the overall shape of the halted filament slightly better. The latter is quantified by the ratio of the leg crossing point height and the terminal height, which is 0.35 for *TRACE*, 0.27 for Case 1, and 0.24 for Case 2.

Next, *reconnected filament threads* appeared as the result of the first reconnection in the helical current sheet (Fig. 4.1(d)). The reconnection is strongest with the overlying flux and eventually cuts the whole flux rope. The figure shows this when about half of the flux in the rope is reconnected. A *TRACE* image that clearly shows the first two sets of reconnected threads (on the front and right-hand side) is used for the comparison. Both cases agree with the observations in the location of the main reconnection at the sides of the filament loop above the crossing point. This location is indicated by the bend points of the reconnected filament threads and flux rope field lines and by various intermittent brightenings in the full series of *TRACE* images (see the animations in Ji et al. (2003) and Alexander et al. (2006), and HK16). The new footpoints of the two sets of reconnected filament threads lie in front of the other filament leg, relatively close to the middle of the whole structure. Both simulation runs show a similar location of the reconnected field line's new footpoints, with Case 1 approaching the observations somewhat better.

The field line plots in Figure 4.1(d) show a significant difference to the corresponding plots for the cases in HK16. Here also the lower part of the erupted rope's legs reconnects with ambient flux. The resulting field

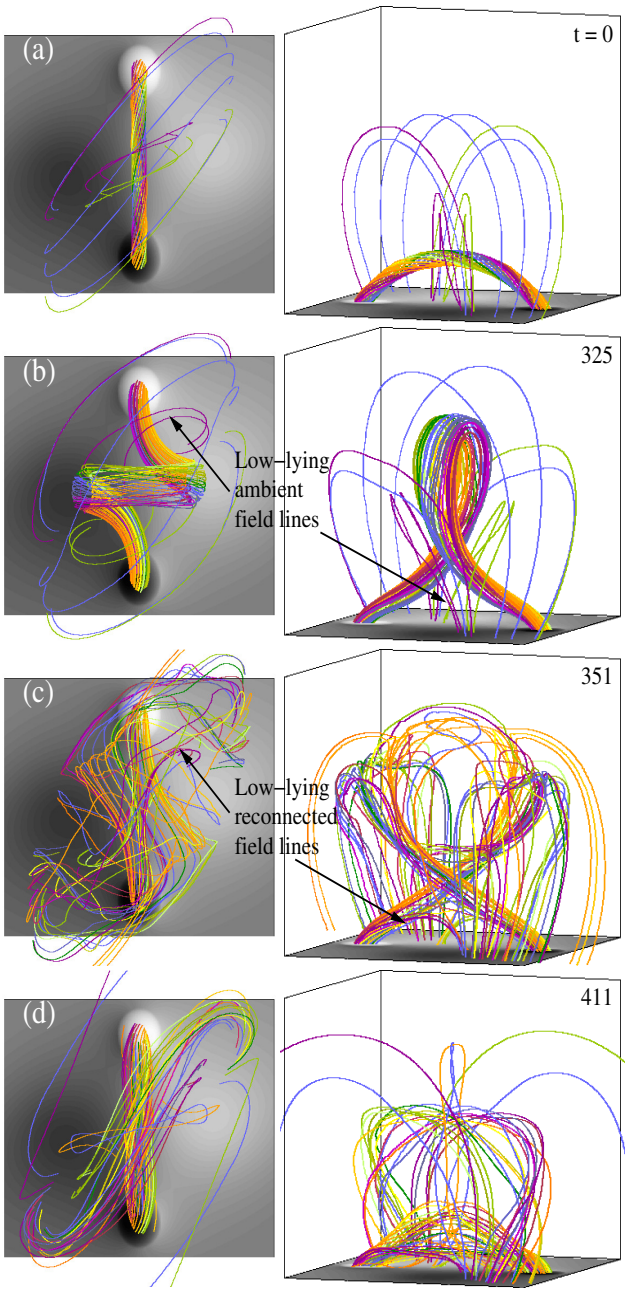

Figure 4.2: Top and side views represent an overview of the reconnection in Case 1. The first main reconnection phase occurs in the helical current sheet, mainly between the top part of the erupted flux rope and overlying flux (panels (c)). This eventually cuts the flux rope completely, producing two bundles of linked flux. Some additional reconnection with ambient flux occurs in the lower part of the helical current sheet (indicated in panels (c)). The second main reconnection phase occurs in a vertical current sheet that forms between the approaching, linked flux bundles, resulting in the reformation of a weakly twisted flux rope and arch-shaped overlying flux (panels (d)). The latter is weakly twisted because it includes the part of the initial flux rope above the leg crossing point.

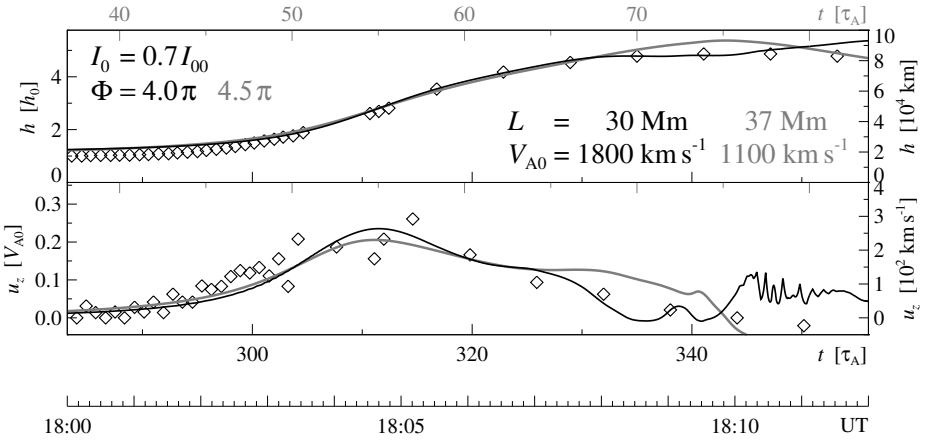

Figure 4.3: Comparison of height and velocity of the fluid element initially at the apex of the flux rope's magnetic axis with the observed rise curve of the filament apex. *Black (gray) lines and legends* refer to Case 1 (Case 2). Smoothed height data from Ji et al. (2004) and smoothed, derived velocities are shown as diamonds. The simulation quantities are normalized by the initial apex height, h_0, Alfvén velocity at the rope's magnetic axis, V_{A0}, and the resulting Alfvén time $\tau_A = h_0/V_{A0}$.

lines are similar to those in the potential field of the TD99 magnetogram, different from the field lines that reconnect in the top part of the flux rope (see Figs. 6(c) and (e) in HK16). The additional reconnection here is due to the proximity of the "sunspots" (a smaller L), which strengthens the ambient flux low in the volume compared to the cases studied in TK05 and HK16. Only a small fraction of the flux in the rope reconnects in this way, so that the reformation of a flux rope (discussed next) is very similar to the previous cases.

Finally, an arcade of *flare loops* was formed (Fig. 4.1(e)). The simulations show this to result from a second phase of reconnection, which occurs in a vertical current sheet that forms between the legs of the cut flux rope near the crossing point in Figure 4.1(c). This happens because the two halves of the cut rope are interlinked. This linking is a consequence of the writhing of the rising flux rope due to the helical kink (see Fig. 4.2 below and HK16). Reconnection in a vertical current sheet is a key process in ejective events (eruptive flares/CMEs) and usually referred to as "flare reconnection". It adds flux to the escaping flux rope above the current sheet and produces flare loops below the sheet. Here the second reconnection reforms a flux rope *below* the vertical current sheet and restores arch-shaped overlying flux *above* it, consistent with the unusual start height of the flare loops. The restored overlying flux shows an overall agreement with the observed flare loops in both cases. In particular, the ratio of projected height and footpoint distance, ≈ 1.1 for Case 1, and ≈ 0.8 for Case 2, matches the observed value of ≈ 1.0 quite well. Both cases also show that the restored overlying flux inherits a small part of the twist in the erupted flux rope, in agreement with the very unusual indication of twist in the flare loops. The field line plots additionally show sets of higher-arching

loops that differ in shape from the flare loop arcade. These contain a minor part of the reformed overlying flux in Case 1, but a significant part (about one half) in Case 2. Hence, the comparison with the observed flare loops clearly favors Case 1 above Case 2.

On the other hand, the value of L in Case 2 lies closer to the distance of the flux concentrations from the polarity inversion line in the magnetogram of the eruption's source region. HK16 estimated the distance to be ~ 40 Mm for both polarities.

The sequence of the two major reconnection phases, the linking of the reconnected halves of the original flux rope, and the eventually resulting reformed flux rope are shown in more detail in Figure 4.2. A flux rope is reformed in the location of the original one, which corresponds to the very low-lying bright EUV loops in Figure 4.1(d). It contains nearly as much flux as the original rope, but is only weakly twisted, $\Phi < 1\pi$.

4.4.2 Rise Profile and Timing

Figure 4.3 shows the scaling of the two simulation runs to the observed rise profile of the eruption. Both cases can be scaled to agree quite well with the observation data. Case 1 fits slightly better, which can be best seen in the comparison of the velocities. The simulation time axes show that, in both runs, the instability needs a long time to lift the flux rope to the observed height, i.e. has a small growth rate. The instability in Case 1 (2) clearly begins to develop out of the initial noise ≈ 10 (≈ 35) min before the initially very slow rise of the filament can be discerned in the*TRACE* data. In fact both initial equilibria are chosen very close to the threshold of the helical kink mode. A small upward initial velocity perturbation, applied only at the flux rope apex and linearly rising to 0.04 (0.02) $V_{\mathrm{A}0}$ at the termination time of 4 (2) τ_{A} for Case 1 (2), is required to launch the instability. The flux rope is slightly lifted above its initial position in the analytical (i.e., approximate) equilibrium during the perturbation and subsequent gradual development in the simulations. Thus, the scaled flux rope heights at 18:00 UT in Figure 4.3 lie slightly above the observed filament height. These heights match the observation much better than the ones in the cases analyzed in TK05 and HK16. More importantly, the more realistic inclusion of the line-tying at the footpoints of the flux rope in the simulations analyzed here is not compromised by the slight initial lifting of the flux rope apex.

The scaling determines the dimensional value of the Alfvén time. This combines with the dimensional value of the length unit (h_0) to imply a value for the Alfvén velocity in the source region of the eruption, which is given in the plot and agrees with the range of known values of this parameter in active regions for both cases (Innes et al., 2003; Wang et al., 2007; Régnier et al., 2008).

4.5 Discussion

Both cases presented in this chapter match the observations reasonably well, thus, both are a valid model of the event. Most items in the comparisons with the observation data yield only a small difference between the cases (mostly favoring Case 1); only the comparisons with the flare loop arcade and with the distance of the flux concentrations in the source region's magnetogram show moderate differences. We give the latter aspect a lower weight in our overall judgment, because the TD99 model in its original form employed here is generally not suited to closely model the complexity of the photospheric flux distribution in a solar active region. Overall then, Case 1 is the better-fitting run. Additionally, the smaller initial twist of this case is in better agreement with recent estimates of the twist that can accumulate in active regions before an eruption occurs.

Comparing Case 1 here with the best case of the broad parametric study of the event in HK16, we first note that both yield the plausible value of $\Phi = 4\pi$ for the initial average twist. Both yield a good match of the observation data. None of the differences in the detailed matching is significant. Case 1 here is slightly superior in reproducing the distortion of the filament when the terminal height is reached and superior in matching the initial part of the rise profile, while the best case in HK16 is slightly superior in reproducing the inverse-gamma shape, the flare loop arcade, and the final part of the rise profile. The difference in matching the distance of the flux concentrations in the magnetogram (parameter $L = 30$ Mm and 57 Mm vs. ~ 40 Mm in the observation data) is not significant. Since Case 1 here achieves the agreement with the observations using a more realistic inclusion of the line tying, it represents the superior model.

4.6 Conclusion

The modeling of the confined filament eruption in solar Active Region 9957 on 2002 May 27 is here further improved above the results in TK05 and HK16 by including the photospheric line-tying of the assumed initial flux rope in a more realistic manner. This is accomplished by using a flatter initial rope, whose apex height agrees exactly with the estimated filament height. A good matching of the observation data is found, equivalent to the previous modeling in the overall quantitative agreement, with only minor, non-significant differences in the details.

Again, an initial average flux rope twist $\Phi \approx 4\pi$ is indicated and a less twisted flux rope is reformed by a sequence of two main reconnection phases, the first in a helical current sheet (different from ejective eruptions), the second in a vertical current sheet (partly similar to ejective eruptions). Additional reconnection of the flux rope legs with ambient flux reduces the flux content of the reformed flux rope somewhat in comparison

to the simulation runs in HK16.

The equivalent quantitative matching of the observation data by the improved model in this chapter lends further support to models for solar eruptions which assume an unstable flux rope to exist at the onset of the eruption's main acceleration phase. In particular, the model for strongly writhing confined eruptions by TK05, which assumes an initially kink-unstable flux rope in the stability domain of the torus instability, is substantiated.

CHAPTER 5

Flux Rope Reformation as a Model for Homologous Solar Eruptions

The results are in preparation for publication.

Based on zero-β pressureless MHD numerical simulations, we proposed in *chapter 3* and *chapter 4* that the failed filament eruption on 2002 May 27 (Ji et al., 2003; Alexander et al., 2006), was caused by the helical kink instability of a flux rope. The toroidal flux rope equilibrium by Titov and Démoulin (1999) was used as the initial condition. It was also found that a two-step reconnection process—first between the rope and the overlying flux, then between the legs of the cut rope—resulted in the reformation of a flux rope in stable state and with strongly reduced twist of less than one turn.

Employing the reformed flux rope result as a new initial condition, we present in this chapter the first MHD simulation results of a homologous sequence of eruptions that show a transition from a confined to two ejective eruptions. The ejective eruptions develop as a result of imposed boundary converging motions and the repeated reformation of a flux rope after each eruption. Subsequently, a part of the positive and negative sunspot flux converges towards the PIL and mostly cancel each other. The two ejective eruptions are driven by continuous flux cancellation. The amount of flux reduction is available to transfer to the magnetic configuration of the reformed flux rope, building up a free magnetic energy. With sustained flux cancellation and progressive weakening of the magnetic tension, we find 6% of flux reduction leads to the first ejective eruption and the second ejective eruption commences after 25% of flux reduction. These results might demonstrate the ability to obtain a homologous eruption by flux cancellation. Depending on the initial configuration of the flux rope, the eruption may loss the equilibrium due to the helical kink or the

torus instability. Furthermore, we shed additional light here about another possibility of the formation of a flux rope, beside flux emergence and flux cancellation processes. Understanding the evolution of homologous eruptions is vital for gaining insight into the mechanisms that produce CMEs and their associated flaring.

5.1 Introduction

It has been observationally found that CMEs frequently exhibit a so-called three-part structure, consisting of an outer leading edge, an embedded bright core, and the cavity in between (Illing and Hundhausen, 1985; Forbes, 2000). It is generally accepted that the bright core of the CMEs corresponds to dense filament plasma, which is supported by an erupting magnetic flux rope prior to the eruptions (House et al., 1981; Dere et al., 1999).

Therefore, all studies which try to model the CMEs involve a magnetic flux rope at some point despite the difference in the underlying physics prior to the eruption (Green and Kliem, 2009; Savcheva et al., 2012; Ouyang et al., 2015). Our question now is at which stage of this eruption the flux rope should be embedded to play its central role. Two possible models with different interpretations have emerged. In the first model, a twisted flux rope is a fundamental to the initiation process of the eruption (Forbes and Isenberg, 1991; Török and Kliem, 2005; Kliem and Török, 2006; Green et al., 2007, 2011; Hassanin et al., 2016; Hassanin and Kliem, 2016). This is because the flux rope may emerge as a coherent structure lifting plasma from the convection zone into the atmosphere (Rust and Kumar, 1994; Lites et al., 1995; Low, 1996; Cheng et al., 2014; Romano et al., 2014). A new flux rope may also be formed as a result of the reconnection of the preexisting potential magnetic lines of an arcade, as illustrated in Figure 1.8 (van Ballegooijen and Martens, 1989b; Amari et al., 2003, 2010; Aulanier et al., 2010; Green et al., 2011; Yardley et al., 2016; Panesar et al., 2017). Alternative in the other model, this process of the flux rope formation occurs during the eruption itself (Antiochos et al., 1999; Moore et al., 2001). One aspect which must also be considered in the debates about the filament formation and the overall evolution, concerns the magnetic configuration that can support this plasma in the solar atmosphere. Magnetic flux ropes with presence of dips are good candidates to suspend and support the dense filament plasma against gravity (Kuperus and Raadu, 1974; Rust and Kumar, 1994; Low and Hundhausen, 1995). Therefore, one can characterize the flux rope as a bundle of field lines that wraps around an axis, creating dips (Titov et al., 1993). The warped topology is not necessary to be highly twisted so it can be 1-1.5 turn or less than one turn (Mackay and van Ballegooijen, 2009).

The filaments are generally visible for days or even weeks in the atmosphere before fading or experiencing an eruption. Such appearance suggests that most of the time, the filaments are in equilibrium with the

surrounding before an external factor disrupts their equilibrium and drives possible cause of failed or ejective eruptions. The most widely accepted interpretation is that the stored free magnetic energy in the highly sheared or the twisted magnetic fields prior to the eruption, are stabilized by the ambient coronal potential fields (Forbes, 2000; Mackay and van Ballegooijen, 2006). In this magnetic configuration, the overlying arcade field which provides the downward tension force, is balanced by the upward magnetic pressure force in the flux rope.

The next argument is about how the magnetic energy which is stored in the coronal magnetic field of the flux rope, increases and then decreases, converting mostly to kinetic energy to power the eruption. This conversion requires the magnetic field to be highly non potential, containing strong electric current densities prior to the eruption. "Storage-and-release" (MHD) models present the roots of this argument. The potential (current free) magnetic fields represent the minimum magnetic energy for a given photospheric flux distribution.

The evolution of the dense photoshpere is slow, therefore the currents which are injected into the corona must also slowly accumulate, such that the magnetic energy of the coronal field increases quasi-statically, as a sequence of force-free equilibria. Once this equilibrium is broken, the magnetic energy in the sheared/twisted magnetic field decreases. This reduction results often from the expansion of the magnetic field, as well as the magnetic reconnection in the current layer.

The triggering of any eruption requires this equilibrium to be destroyed by reaching some threshold where the regime of the magnetic pressure force dominates. It is conceivable that what initiates and triggers such magnetic topologies to become unstable and liberate this stored energy might be due to: kink or/and torus instability. The average twist of the flux rope is the main controlled condition in the kink instability. The twisted flux rope can erupt and become susceptible to the helical kink instability (Török et al., 2004; Fan and Gibson, 2004; Török and Kliem, 2005; Hassanin and Kliem, 2016; Hassanin et al., 2016), when the average twist of its magnetic field lines exceeds the critical value of about 1.75 turns (Hood and Priest, 1981; Einaudi and van Hoven, 1983). The torus instability takes place when the magnetic field of the overlying arcade falls off sufficiently rapidly with height (van Tend and Kuperus, 1978; Démoulin and Aulanier, 2010). A critical point in the torus instability, is given by the so-called decay index, $n = \frac{\delta lnB}{\delta lnz} = \frac{3}{2}$ Bateman (1978), which qualifies how the potential magnetic field declines along the vertical direction (z-axis). Above this value, $n > \frac{3}{2}$, the unstable flux rope can produce a successful eruption (CME) (Török and Kliem, 2007).

However, the Sun also produces homologous eruptions. The flare Eruptions that occur repetitively at the same location, i.e. in the same active region and specifically at the same PIL, having many similarities in structure and morphology within a certain period of time are called a homologous eruptions. Recurrent homologous flares can gradually destabilize the filament system and in turn lead to the ejective flare and a

CME. A series of homologous confined eruptions may occur, followed by a final eruption as a CME (Panesar et al., 2015; Liu et al., 2016b). During 2011 June 16-17 a series of at least eight homologous confined eruptions occurred and followed by a final eruption as a CME (Panesar et al., 2015). These confined eruptions could prepare the system for a CME. Virtually all existing models show the successive eruptions as only CMEs or only as confined eruptions due to the sustained emergence of twisted flux ropes or some boundary-driven (DeVore and Antiochos, 2008; Soenen et al., 2009; MacTaggart and Hood, 2009; Chatterjee and Fan, 2013; Archontis et al., 2014).

The converging motions of the opposite polarity flux patches toward the (PIL), along which the filament initially resides, can be easily driven by the development of super-granular cells. These converging motions in the sheared overlying magnetic fields might lead to the mutual collision, merging and mostly canceling of magnetic fragments of the opposite polarity. The gradual decline of the flux in this area of active region in vicinity of PIL (Martin et al., 1985) in events known as the *flux cancellation*, resulting in internal reconnection in the erupting field and leading up to a filament eruption (explained in more details at *section 1.6.2*).

5.2 Numerical Simulation

All the basic assumptions, MHD equations and the other numerical settings are kept the same as in *chapter 3, section 3.3*. We use in this chapter a stretched Cartesian grid of size $|x| \leq 16$, $|y| \leq 16$, $0 \leq z \leq 32$ with resolution 0.02 in the flux rope area. To obtain sequence of CMEs after the confined eruption, we omit the line current which exerts the external toroidal field in this study (Török et al., 2011a). We use the normalized geometrical parameters as HK16, excepting for L, resulting $h_0 = 1$, $R \approx 1.8$, $L = 3.3$ and $a \approx 0.45$. For the further numerical details we refer to Titov and Démoulin (1999), *chapter 3 and chapter 4* (Hassanin and Kliem, 2016; Hassanin et al., 2016).

In this study, we relax the resulting configuration after the first eruption until it shows no dynamic behavior and then reset the time to zero. We impose a localized flow pattern in the x-y plane of area $|x| \leq 2.8$, $|y| \leq 1.49$ at z=0. This flow consists of a prescribed velocity $u_x(x, y, t)$ inside each of two rectangular areas (which have the sides extended with semi-circles to avoid sharp corners) centered at the distance $d = \pm 1.4$ from the PIL which points nearly perpendicularly and symmetrically towards the PIL, and zero elsewhere. The flow velocity peaks in the rectangular core areas at distance d from the PIL and falls smoothly to zero toward the boundaries of the area using a cosine profile, $\boldsymbol{u_x} = \pm 0.03 \quad V_{aomax} \quad cos((\frac{\pi}{2})\frac{\delta}{w})$, where δ is the distance from the center line of the rectangle, $|x| = d$, and the width of the profile is adjusted to the size of the area, i.e., $w = d$. The inflow velocity is linearly ramped up and down, each during $2\tau_A$, and kept

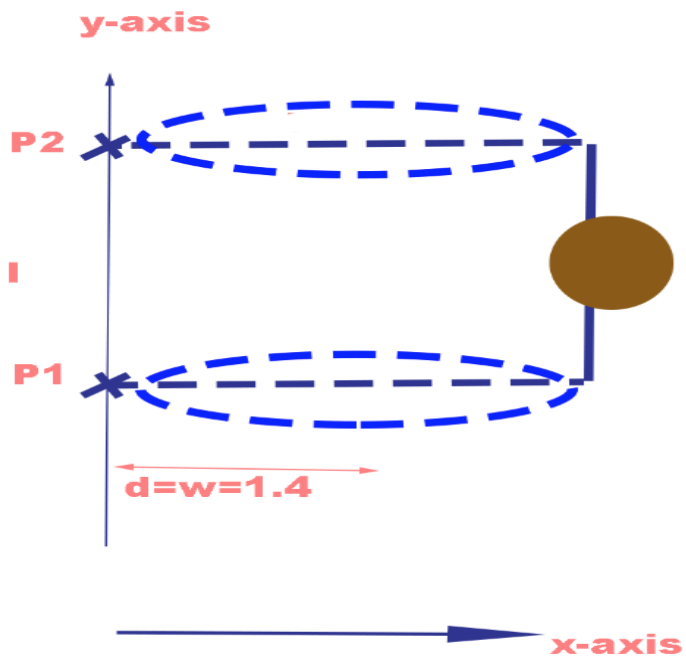

Figure 5.1: The figure shows the area of the prescribed converging flows in the bottom boundary to the right of the line through P1 and P2. I represents the section between P1 and P2, where P1(x,y) and P2(x,y) define the new location of the PIL under the influence of the flow. The sunspot id indicated as a shaded circle.

constant at the maximum value of $0.03V_{aomax}$ in between as shown in Figure 5.1 .

These converging flows bring a part of the flux from both polarities toward the PIL. The numerical magnetic diffusion is introduced in a strip around the inversion line in the bottom plane by using the artificial smoothing (eq.(2.6)) for $\boldsymbol{B}$. The magnitude of this diffusion is set by the level of $\sigma = 0.02$ at $z = 0$ and at $\sigma = 0.04$ for $z > 0.5$ (adjusted in the course of the run), with a gradual transition at intermediate height. So the accumulation of opposite flux polarities gets gradually canceled.

5.3 Analysis and results

5.3.1 The First Eruption as a Confined Eruption

The helical kink instability occurs for a line-tied and uniformly twisted tube, when the twist of the flux rope exceeds the threshold of the critical value of about 1.75 turns (Hood and Priest, 1981; Einaudi and van Hoven, 1983). Therefore, the performed simulation in this section is started with a helical kink unstable and arched TD flux rope with an average twist $\phi = 4\pi$ and without any influence of an external toroidal field B_{et}, (i.e., the line current in the TD model is $I_0 = 0$). Our strategy here is to track the scenario of a transition

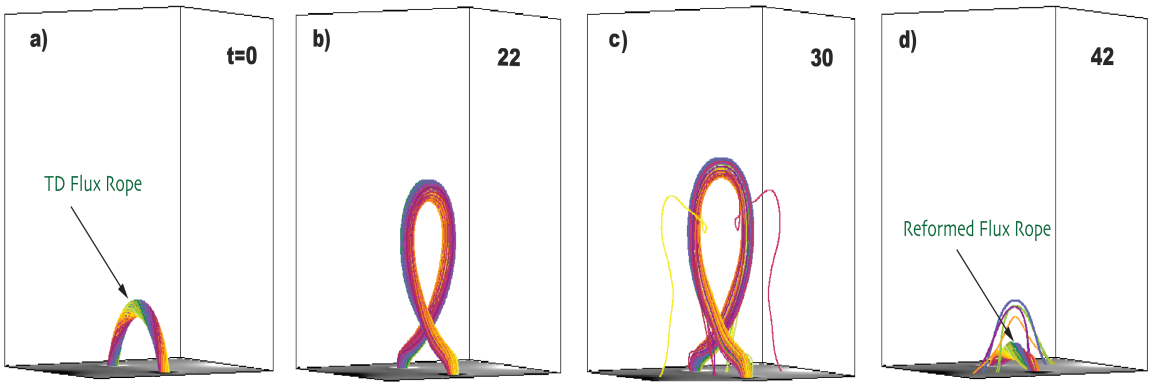

Figure 5.2: a) Magnetic field lines outlining the core of the kink-unstable flux rope (with start points in the bottom plane at circles of radius $(a_o/3)$ at $t = 0\tau_A$. The central part of the box (a volume of size 4X4X6 is shown, and the magnetogram,$B_z(x, y, 0, t)$, is included.

from a confined eruption to ejective eruptions in the same homologous process. Consequently, we set a large value for $L = 3.3$ to have a strong external poloidal field B_{ep}, so we can produce a confined eruption firstly. Figure 5.2(a) shows a flux rope at $t = 0\tau_A$ with the initial parameters as described previously. The erupting flux rope develops at $t = 21\tau_A$ a clear helical shape (i.e., *inverse gamma shape*) which yields the conversion of the twisting in the flux rope into writhe of the flux rope's axis (Török et al., 2010). The flux rope starts with an exponential ascent as shown in Figure 5.3, due to the helical kink instability. The external poloidal field B_{ep} which represents one component of the overlying field, plays the role in this phase to resist the accelerating ascent of the erupting filament and to confine it where the instability becomes saturated and the flux tube's apex stop at $h_\infty \approx 5.6h_o$ at $t \approx 30\tau_A$ as is shown in Figure 5.2(c) and Figure 5.3. Therefore, a reconnection phase between the ambient field lines and the flux rope lines takes place, due to the existence of a helical current sheet. Two linked flux bundles are formed as a result from the *first reconnection process* and later they reconnect again. The lower part of linked flux bundles reconnects to reform a new flux rope and the upper part reconnects to reform a new ambient overlying field lines as in Figure 5.2(d). After the two reconnection phases, the instability saturates at $t \approx 40\tau_A$ and the flux rope reaches its terminal height, producing a reformed flux rope and loop arcade as illustrates in Figure 5.3. For more details, we refer to HK16 and HKS16.

The flux rope evolves a stable and less coherent reformed flux rope configuration, with average twist less than unity as shown in Hassanin and Kliem (2016) (HK16). This reformed flux rope is stable with respect to the helical kink mode because $\phi < \phi_{cr}$ and with respect to the torus mode also because at its low height the decay index is subcritical, $n < n_{cr}$. In this case the reformed flux rope no longer contains sufficient free energy in order to trigger subsequent eruptions, so the suggested scenario is to energize it.

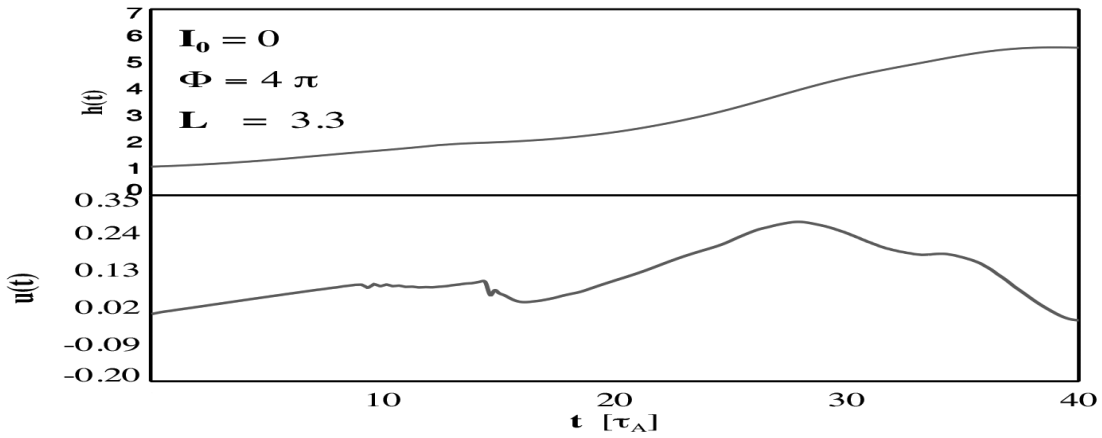

Figure 5.3: The height and velocity profiles of the fluid element initially at the apex of the flux rope's magnetic axis. The simulation quantities are normalized by the initial apex height, h_0, Alfvén velocity at the rope's magnetic axis, V_{A0}, and the resulting Alfvén time $\tau_A = h_0/V_{A0}$. a)

5.3.2 Toward the Ejective Eruption

Cancellation Flux Process to Erupt the Reformed Flux Rope

As we explained in *chapter 1, section 1.6.2*, many investigations show surprisingly that many recurrent flares were found to be clearly homologous eruptions, occurring at the same location, due to the flux cancellation. The continues flux cancellation can destabilize the fields holding the filament material and cause sequence outward eruptions. Some homologous eruptions display multiple or four homologous jets eruptions at the same PIL (Green et al., 2011; Panesar et al., 2016, 2017). Similarly, Sterling et al. (2017) found that as long as the flux cancellation continues in the same active regions, the eruptions of the the jets would be still occurring.

Figure 5.4 shows the cancellation process in our simulation. Figure 5.4 (c.1) illustrates how the reformed flux rope initially resides over the magnetic PIL between the opposite-polarities of magnetic flux of sunspots. The positive and negative clumps converge and mostly cancel each other, as illustrated in Figure 5.4 (c.2, c.2.1, c.2.2 and c.2.3). Figure 5.4 shows that the total flux continuously decreases with time, which is a clear evidence of flux cancellation at PIL of the flux rope. The continuous flux cancellation builds up energy slowly in the magnetic configuration of the reformed flux rope, depending on the amount of converging flux, and finally destabilizes the field and then the eruption ensues. The eruption of a flux rope by flux cancellation occurs only when a critical threshold is passed. Depending on the initial configuration considered in these simulations with pre-exciting of reformed flux rope, 6% of flux cancellation would be sufficient to trigger a failed or an ejective eruption.

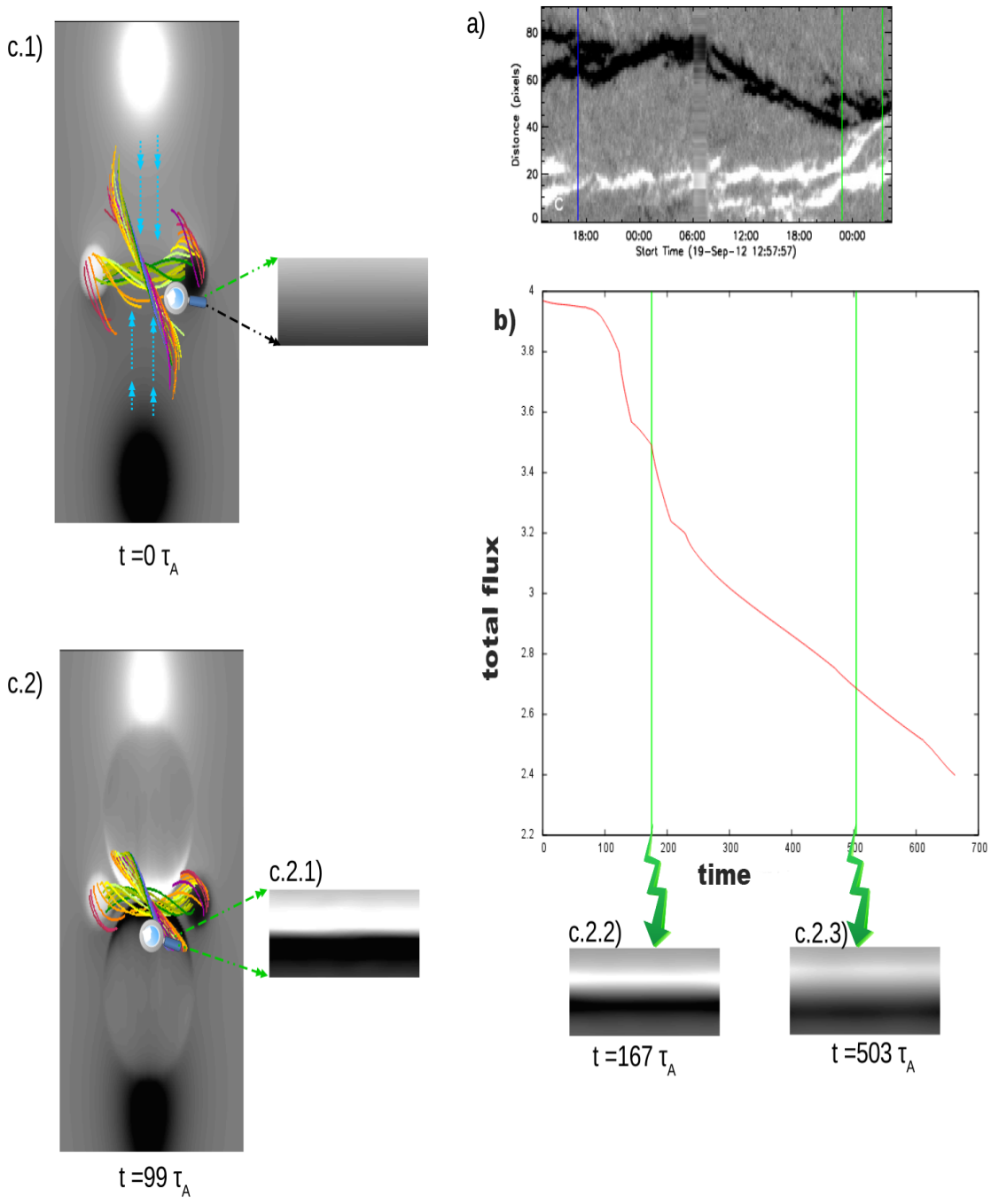

Figure 5.4: a)The Magnetic Imager(HMI) time-distance from Panesar et al. 2017, with permission. The blue line indicates the time of the minifilament formation and the two green lines indicate the eruption times on 20th and 21st September 2012. b) This plot shows the flux reduction rate for the whole simulation and the two green lines indicate the two eruptions in this run. c.1) Top view of the reformed flux rope at the beginning of the simulation before applying converging motions at $t = 0\tau_A$, with a maximum velocity of $0.01V_{aomax}$. c.2) Top view after imposing the converging motion at the bottom boundary at $t = 99\tau_A$. c.1.1, c.2.1, c2.2 and c2.3) Zoom picture for the cancellation of opposite-polarities converging flux at the neural line for time $t = 99\tau_A$, $t = 167\tau_A$ and $t = 503\tau_A$, respectively.

Many numerical simulations of eruptions driven by flux cancellation have obtained similar values for the reduction rate of the flux at the onset of eruption, lying in the range 6-10% (Amari et al., 2010; Aulanier et al., 2010). In this run of L=3.3, 6% amount of flux cancellation needs for the first eruption to be trigger. The reformed flux rope erupts totally to form a CME, and then a new flux rope reforms at the same location and later is erupted again to form a second eruption after a reduction of 25% amount of the converging flux. Eventually, the flux cancellation terminates when all the converging flux patch vanishes and consequently the eruption ceases. This synchronization happens only for fast enough cancellation rate (Yardley et al., 2016).

Building up a Free Magnetic Energy in the Reformed Flux Rope

Not all of the magnetic field lines of the flux rope reconnect together to form the reformed flux rope after the confined eruption as shown in Figure 5.5(a). In particular, to approach the state of a lower energy, some of the reconnected flux rope bundles evolve less sheared and potential loops rather than to reconnect together to contribute to the reformation of a less twisted flux rope. Therefore, we track the quasi-static building up of axial and helical fluxes in the reformed flux rope which occurs as a product of the reconnection low in the bottom plane as illustrated in Figure 5.5. In light of this, imposing converging motion of opposite magnetic fluxes in the photosphere accumulates the highly sheared loops in the vicinity of the PIL. These short and sheared loops experience reconnection due to the flux cancellation to develop more twisted and long field lines with dips. In the later stage, parts of the sheared field lines evolve and merge into characterized J-shape that cross the PIL as shown in Figure 5.5(d), top view.

The proposed reconnection weakens largely the magnetic tension force of the overlying field lines and feeds the reformed flux rope with an additional magnetic flux, increasing the magnetic pressure force of the reformed flux rope. The continuous accumulation of the poloidal flux increases the twisted of the reformed flux rope, and expands the lines to a higher height and consequently leads up later to the eruptions. Reconnection episodes may occur at one or both ends of the sheared field lines at the PIL and flux cancellation events can be recognized here as the main source of building up the current and the free magnetic energy in the reformed flux rope.

It is also perhaps interesting to view the evolution of the system in terms of the energy of the corresponding magnetic energy and its conversion mostly to kinetic energy. The pre-eruptive energy storage phase represents the long buildup and increasing quasi-exponential of the magnetic energy in the magnetic reformed flux rope for around $t \approx 140\tau_A$. Over the time of this building up and prior to the eruption, the kinetic energy remains negligible. As a result of the eruption, the decline of the magnetic energy, which is illustrated

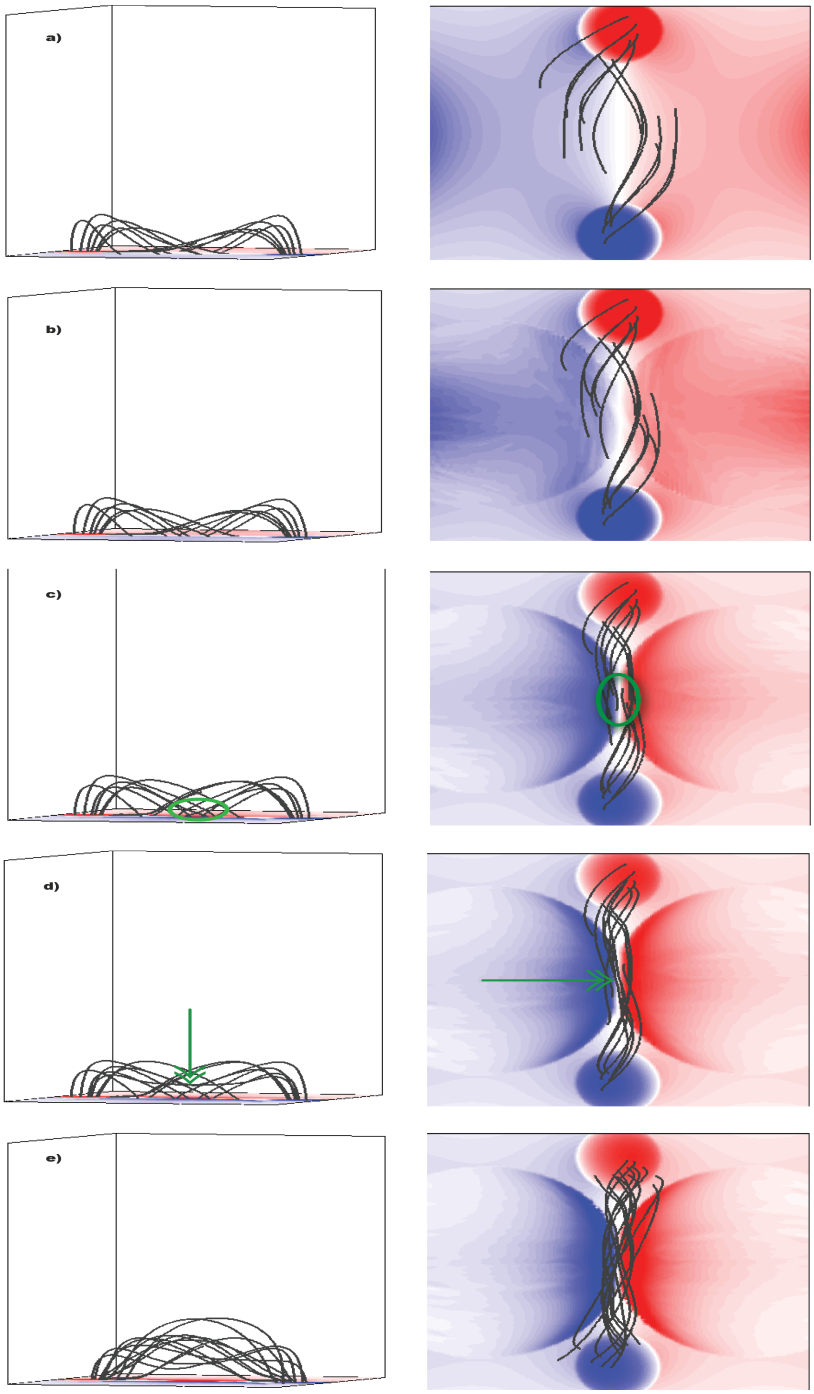

Figure 5.5: The flux cancellation in a sheared magnetic field of the reformed flux rope. Selected field lines are chosen to show how a formation of the twisted field lines from the sheared field lines occurs after applying converging motions. The left panels represent the side view, and the right panels represent the top view. Both the left and right panels are for the same magnetic field lines for the same simulation. a) shows the sheared field lines of the flux rope at t=0 τ_A, b) - c) show the influence of applying converging motions at t= 15 τ_A and t=58 τ_A, respectively, d) illustrates the reconnection event between the sheared field lines from opposite polarities at t=67 τ_A, and e) shows the formation of the flux rope at t=72 τ_A.

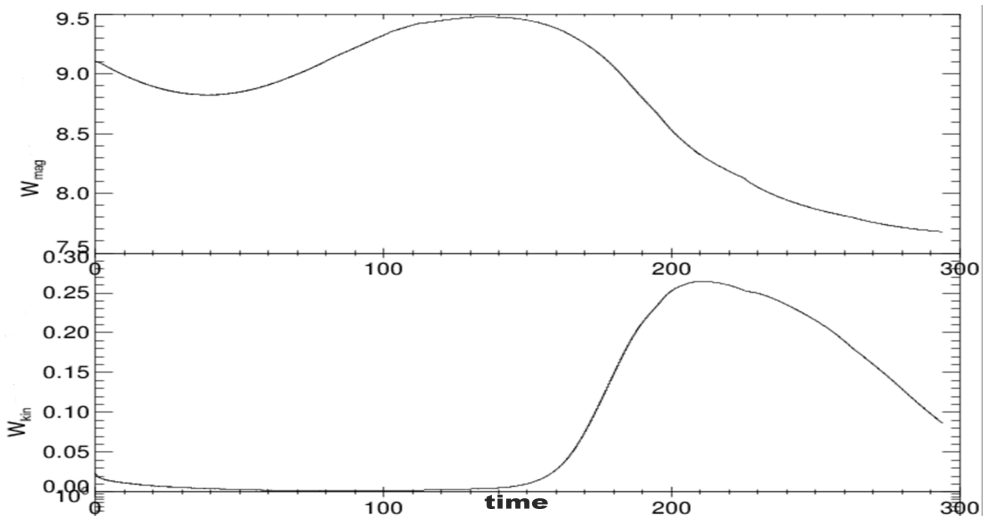

Figure 5.6: The time variations of the magnetic and the kinetic energy during the simulation after applying converging motions in the bottom plane.

in Figure 5.6, leaving the kinetic energy its plateau at the onset of the eruption and later the corresponding increase of the kinetic energy.

5.3.3 The Second and the Third Eruptions as two CMEs

A stability of the reformed flux rope can be reached when the magnetic pressure force in the flux rope is balanced by the magnetic tension forces in the external ambient arcade. The magnetic pressure force tends to expand the magnetic configuration of the twisted reformed flux rope while the tension forces suppress this expansion. Therefore, the building up of an axial and helical fluxes in the reformed flux rope via reconnection increases its magnetic pressure and hoops forces and removes the stabilizing overlying fields until the magnetic field configuration can no longer maintain an equilibrium. To obtain this goal, when the reformed flux rope settles down to an equilibrium state, we build up a free magnetic energy by imposing converging motion with a maximum velocity of $0.03V_{aomax}$ for $t \approx 140\tau_A$ at the bottom boundary, as used in Török et al. (2011b). Consequently, a small part of the sunspots is transported toward the PIL. The opposite-polarity magnetic flux accumulates at the PIL, ensuing cancellation. The flux cancellation builds up the free energy into the magnetic field of the flux rope. With sustained flux cancellation and progressive weakening of the magnetic tension, the reformed flux rope is destabilized and slowly rises. In our case here, the reformed flux rope is stable against the torus instability, $h_{cr} \approx 2.5$, at the onset of kink instability with average twist $\Phi \approx 3.76\pi$. Therefore, the reformed flux rope begins to kink and move rapidly upward at height lower than the required height for torus instability's condition to be fulfilled. Once the reformed flux rope reaches the critical height of torus instability at which $n_{cr} \sim 1.5$ (Fan and Gibson, 2007; Török and Kliem,

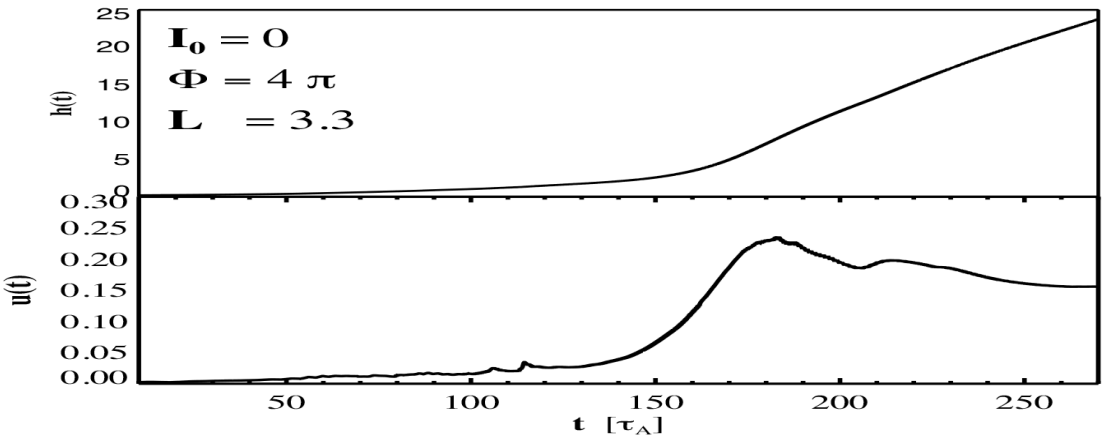

Figure 5.7: The height and velocity profiles of the rise curve of the flux rope's apex after imposing a localized flow pattern in the x-y plane, leading to the first ejective eruption.

2007; Aulanier et al., 2010), it accelerates rapidly. We estimate the decay index is $n \sim 1.9$ at the height of the rope apex when it starts to face instability and accelerate upward. However, the kink instability boosts the reformed flux rope to the height at which the torus instability regime dominates, producing a second eruption as a CME. Figure 5.7 shows the slower-rise phase from the beginning of the simulation to $t \approx 140\tau_A$, followed by a faster-rise phase from $t \approx 140\tau_A$ in the course of this ejective eruption. Figure 5.8(a) shows the left-direction rotation of the reformed flux rope about its ascent's direction, by cause of the conversion of reformed flux rope twist into a writhe of its axis (Török et al., 2010). We refer also in HK16 to show how the toroidal external field may have an influence on the inverse gamma shape.

The cancellation is enabled by reconnection (van Ballegooijen and Martens, 1989b). Therefore, the amount of canceled flux is potentially available to transform into the flux rope as mostly axial and poloidal fluxes (Amari et al., 2010; Aulanier et al., 2010; Green et al., 2011; Savcheva et al., 2012; Yardley et al., 2016). The eruptive phase normally occurs via reconnection in two stages (van Ballegooijen and Martens, 1989b). The first stage represents the accumulation of the highly sheared bundles from the overlying arcade topology to build up axial flux. Theoretical studies, (i.e. Amari et al. (2003); Aulanier et al. (2010)) support such a scenario. However, in our simulation, the axial flux above the PIL contains already the main contribution from reformed flux rope, so this does not apply in our scenario. Furthermore, we note that the reconnection does not commence a long time period until the instability to erupt the reformed flux rope sets in, as is shown in Figure 5.8(a). It is sufficient if hoop forces increase and subsequently lead to the slowly rising reformed flux rope to reach the critical twist for the kink instability onset and then has been accelerated by reaching the critical height for torus instability. The diverging flows contribute to create more coherent flux rope shape. These sheared loops may be resulted from the converging motion and not from the reconnection

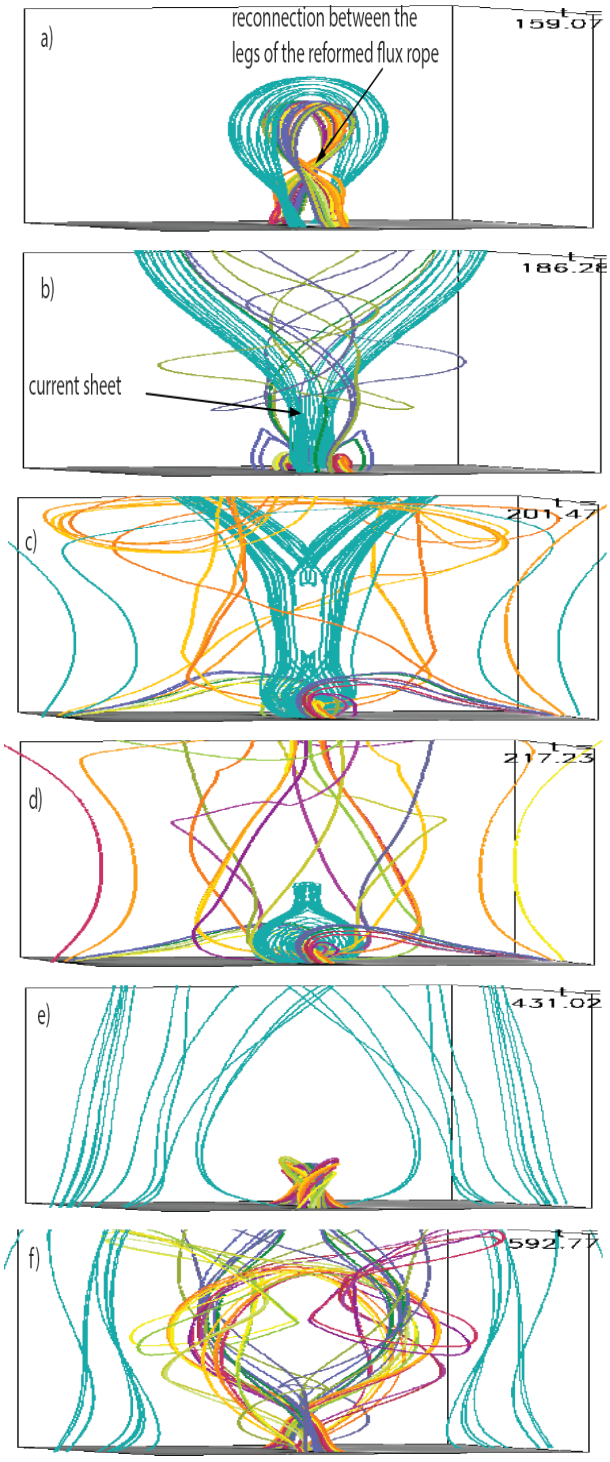

Figure 5.8: An overview of the reconnection phases and the characteristic stages of the reformed flux rope's eruption as two ejective eruptions. (a) The rising of the reformed flux rope due to helical kink instability and reconnection of its legs, (b) the beginning of the current sheet to be formed, (c) reconnection phase at the current sheet to trigger a CME, (d) reformed flux rope and overlying cups resulting from the reconnection, (e) a second unstable reformed flux rope starts to rise, and (f) forming of the second ejective eruption. All the field lines (except for d) are traced from start points in the same fluid elements (mostly fixed in the bottom plane; the others moving with the top part of the unstable flux rope).

due to flux cancellation.

The dips in such a magnetic configuration are capable of supporting more filament dense material. The helical shape detached to the flux rope first begins to forms at $t = 60\tau_A$ and continues to build more and more twist, creating a reformed flux rope with dips and turns and leading up later to the first eruption as explained previously.

The legs of the reformed flux rope reconnect firstly to form a second reformed flux rope before the formation of the vertical current sheet between the overlying magnetic field lines themselves, as is shown in Figure 5.8(a). Later, the converging motion brings the overlying field lines closer to each others to form the current sheet and reconnect to eject a CME, as is illustrated in Figure 5.8(b) and (c).

As the reformed flux rope and the overlying magnetic field eject upward rapidly and pinch off, leaving their products of a CME, a roughly twisted second reformed flux rope at the same PIL and cusp loops. The cusp-shaped loops behaves as a new overlaying magnetic arcade, enveloping the second reformed flux rope. The flux cancellation is not yet ceased. It is worth emphasizing again that the occurrence of sustained flux cancellation of converging different polarities patches, adds shear or/and twist to the filament field and may lead later to further eruptions (Yardley et al., 2016; Panesar et al., 2017). The flux cancellation continues progressively building up a free energy into the magnetic field of the second reformed flux rope. It is not surprising that the third eruption consumes more canceled flux to build up a flux rope and later to experience an instability. The reduction rate is of the order of 25% at the time when the second reformed flux rope shows an instability and eventually the eruption starts again. Figure 5.8(e) and (f) show in the course of flux accumulation and reduction, sufficient fluxes have been added to the second reformed flux rope to cause the instability, initiate its rising and later trigger the second ejective eruption of the reformed flux rope, emphasizing the importance of sustained flux cancellation.

5.4 Comparison between Different Types of Homologous Eruptions

A confined eruption is a case in which the flux undergoes instability and rises to reach a terminal height where the erupting flux rope halts and then the filament material slides back to the solar surface (e.g. Ji et al. (2003)) without showing any evidence of a CME. Possible suggestions for the causes of failed eruption are: insufficient free magnetic energy to energize the flux rope to be erupted as a successful eruption (Shen et al., 2011) or to be confined by the overlying magnetic field, as in HK16 and HKS16. Therefore, proceeding to more quantitative analysis, we attempt to compare between different homologous eruptions. Table 5.1

Table 5.1: Table showing different types of sequence eruptions due to varying the initial parameters of TD flux rope.

Type of eruption	$I = 0$ **and** $L = 3.3$	$I = 0$ **and** $L = 2.3$	$I * 0.7I_o$ **and** $L = 2.3$
1st eruption	confined	ejective	confined
2nd eruption	ejective	ejective	confined
3rd eruption	ejective	ejective	confined

provides an overview of the different external overlying strengths and the fates and types of the sequence of eruptions.

Similar to the previous section, we use here the reformed flux rope which produced from a pre-existing kink unstable flux rope as in HK16. We choose the best case of the initial parameters of $\Phi = 4\pi$, $B_{et}/B_{ep} \approx 1$, and $L = 2.3$ Mm from HK16 (*chapter 3*) to be our candidate in this section. In that respect, we employ the stable reformed flux rope, which experiences the influence of the toroidal overlying field, as a new initial condition to investigate whether homologous eruptions can be produced when the configuration is driven by photospheric motions and also which type of eruption will be resulted. Subsequently, we impose the converging flows of the opposite-polarities of magnetic flux of sunspots towards the PIL along where the stable reformed flux rope resides. The patches from the sunspots approach each other to start the flux cancellation process beneath the reformed flux rope. The initiation of the second confined eruption commences with with an exponential ascent at $t \approx 115\tau_A$. Once the instability saturates, the erupting reformed flux rope halts by reaching its terminal height of $\approx 7.5h_0$ which is higher than the terminal height at where the flux rope halts in the first confined eruption of $\approx 3.5h_0$.

Figure 5.9 shows the triggering of a confined eruption due to a flux cancellation. The confined eruption has only one reconnection phase, unlike two reconnection phases as in HK16 and HKS16. The reconnection proceeds at X-lines under the apex of the rising reformed flux rope between its legs and the converging overlying field lines, leading to a confined eruption and two flux ropes . The amount of the flux reduction prior to the second confined eruption is 4%. This result indicates that in addition to the overlying external field confining the newly reform flux ropes, the free magnetic energy stored in this configuration is insufficient to drive an ejective eruption.

5.5 Summary and Conclusions

In the context of triggering homologous eruptions, we have presented a three-dimensional magnetohydrodynamic model, employing a reformed flux rope as a new initial condition, in which the evolution of subsequent homologous eruptions are driven by imposed boundary converging motions, leading to flux cancellation. In

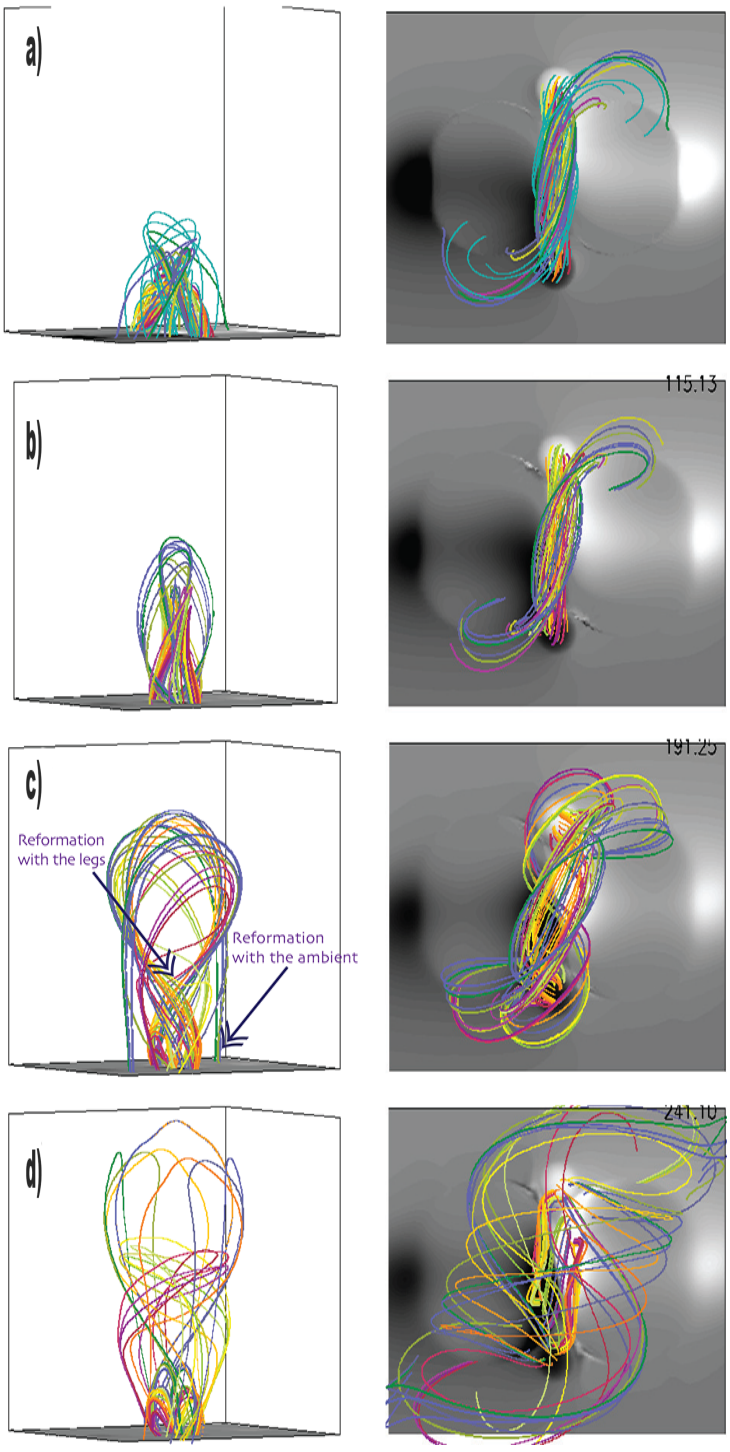

Figure 5.9: Overview of the characteristic stages of the second confined eruption due to the flux cancellation. (a) Imposing converging motions at the bottom plane, (b)shows the rising of the reformed flux rope, (c) reconnection phase between the legs of the flux rope and the flux rope and the overlying field lines, (d) formation of two flux ropes after the reconnection phase.

contrast to other simulations, where such flows have been used to create a flux rope from a sheared arcade (e.g. Amari et al. (2000)), the flows in this study abandoned this step instead to form more helical magnetic fields around the reformed flux rope which leads to several eruptions.

The simulation shows a transition from a confined eruption to an ejective eruption when 6% of the converging fluxes are canceled. This is followed by a second reformed flux rope which experience another ejective eruption.

Following the building of axial and helical fluxes in the reformed flux rope, we showed that the sheared loops move in the vicinity of the PIL and experience further reconnection and this is accompanied by storage of the free magnetic energy in the flux rope body and leads to a second eruption. This second eruption is accompanied by increasing the kinetic energy at the expense of the magnetic energy. By modeling the simulation with influence of a toroidal overlying field magnetic strength, we showed that a confined eruption can be followed by another confined eruption.

To conclude, the reconnection driven by flux-cancellation contributes in building a new free magnetic flux in the reformed flux rope and therefore to gradually lift it up in altitude. The erupting flux rope can lead to a variety of homologous eruptions such as series of CME or confined eruptions or transition from a confined to a CME depending on the amount of the flux reduction in addition to the magnetic strength of toroidal or poloidal overlying field.

CHAPTER 6

Conclusions and Future Work

Solar eruptions such as coronal mass ejections (CMEs), flares and filament (or prominence) eruptions are magnetically driven. This energy is stored in the coronal magnetic field before the eruption takes place. The key question here is how the eruptions are triggered and driven. We use the Titov–Démoulin (TD) model of a force-free flux rope equilibrium in a bipolar ambient field (Titov and Démoulin 1999) as the initial condition to extend the parametric study of Török and Kliem 2005 by varying the strength of $\boldsymbol{B_{et}}$ (i.e., the line current $\boldsymbol{I_0}$), the verage twist Φ(i.e., the minor radius a), and the spatial scale of $\boldsymbol{B_{ep}}$(i.e., the source distance L) to achieve good agreement with the essential properties of the confined filament eruption in AR 9957 on 2002 May 27, as observed by the *TRACE* satellite in the EUV. Next, to obtain a more realistic inclusion of the photospheric line tying, the initial flux rope equilibrium is chosen to possess a small apex height identical to the observed initial filament height. Thus, the model for strongly writhing confined solar eruptions, which assumes that a kink-unstable flux rope in the stability domain of the torus instability exists at the onset of the eruption's main acceleration phase, is further substantiated. In particular, overlying flux and a far less twisted flux rope are reformed as a result of two distinct phases of reconnection during the confined eruption. The reformed twisted flux rope offers a pathway to homologous eruptions which we obtain in this study by imposing driving horizontal motions in the photospheric boundary. A summary of each of these studies' conclusions is presented below.

6.1 Helical Kink Instability in a Confined Solar Eruption

We performed a parametric study, extending the work of TK05, to obtain the full picture of the event of a confined eruption on 2002 May 27. Our results are in a good agreement with the main features of the event, starting from the the confined nature of the eruption, the writhing of the erupting flux rope's axis, followed by reaching the terminal height, the distortion of the top bundle of the flux rope field lines and finally the formation of the unusual (slightly twisted) flare loops. This agreement is an additional support for the TK05 model, which assumed that the flux rope is kink-unstable and torus-stable at the onset of the confined eruption.

Employing quantitative comparisons with the observation in this study, we find very good agreement for the case $\frac{B_{et}}{B_{ep}} \approx 1$ and average twist of the erupting flux rope $\Phi \approx 4\pi$. This is in a better agreement with estimated twist values in the recent literature than that the estimated of $\Phi \approx 5\pi$ in TK05. Two strong reconnection phases have been found through the confined eruption triggered by the helical kink. The first reconnection phase, which is with the ambient field lines, takes place in the helical current sheet formed by the writhing flux rope and destroys the top part of the rope. Subsequently, this, in turn, leads to anther strong reconnection phase, which takes place in the vertical current sheet between the legs of the original flux rope, forming a stable, less twisted and less coherent flux rope. This reconnection proceeds in the center of the system and also restores the overlying loops, forming the flare loops of the event.

A weakness in our numerical model HK16 and also in TK05 is in the relatively poor matching of the initial filament height which implies a weaker effect of the photospheric line tying compared to reality. So, to obtain more realistic inclusion of the photospheric line tying of the assumed initial flux rope, we use a flatter initial rope, also with an average twist $\Phi \approx 4\pi$, whose apex height agrees exactly with the estimated filament height. A good matching of the observational data is found, equivalent to the previous modeling in the overall quantitative agreement. By decreasing the depth of the submerged flux tube (i.e. to obtain a flatter flux rope), the results from Hassanin & Kliem 2016 are improved; now the lower part of the height-time profile of the flux rope is better matched, and L gets closer to the observed value. At the same time the other results continue to positively agree with the key features of the observed event, and also the formation of a less twisted flux rope after two reconnection phases is found. A kink-unstable and flatter coronal flux rope yields the best match with the characteristic properties of the confined eruption in AR 9957 2002 May 27 so far obtained.

6.2 Homologous Eruption

Employing the reformed flux rope from the first part in this study as a new initial condition, we present a three-dimensional magnetohydrodynamic model to study the triggering of homologous eruptions. The evolution of subsequent homologous eruptions which consists of a transition from a confined eruption to two ejective eruptions, is driven by imposed converging motions in the photospheric boundary, leading to flux cancellation. The flux from the sunspots with different polarities is transported toward the polarity inversion and cancels each other. A Sequence of ejective or confined eruptions could be triggered, depending on the fulfillment of the onset criterion of the kink or torus instability, which in turn, depends on the mechanisms that produce the reformed flux rope.

Following the approach of van Ballegooijen and Martens (1989b); Green et al. (2011); Savcheva et al. (2012), the amount of canceled flux is available to be transfered into the magnetic configuration and builds up free magnetic energy. The essential point here is to build up enough free magnetic energy available to trigger a sequence of eruptions. When the flux cancellation reaches more than 6%, an ejective eruption is triggered. Subsequently, another ejective eruption happens when a further flux reduction of 22% occurs. This model is supported by observations examined in Panesar et al. (2017). In particular, sustained photospheric flux cancellation plays the role of a "flux-feeding" process into the reformed coronal flux rope configuration, which can drive the reformed flux rope to experience the kink instability or the torus instability. The eruptions are accompanied by increasing kinetic energy at the expense of magnetic energy, which is released in the two ejective cases.

To conclude, flux-cancellation-driven photospheric reconnection contributes in building a new free magnetic flux in the reformed flux rope and to gradually lift it up in altitude. The erupting flux rope can lead to a variety of homologous eruptions such as a series of CMEs or confined eruptions or a transition from confined eruptions to CMEs, depending on the amount of flux reduction and on the strenght of overlying toroidal and poloidal field.

6.3 Future Work

A missing piece of this puzzle of homologous eruptions' simulations is to include different values of an initial shear field component in the coronal field, which is often observed. It would therefore be useful to generalize the results of the last chapter of this work to obtain different types of homologous eruptions, transitions from confined to ejective eruptions, sequences of confined eruptions or sequences of ejective eruptions. Thus a first

step of the future work should be directed to the extension of my PhD work to set a comprehensive analysis of the homologous process with different underlying pre-eruption physics. The amount of transported fluxes may also control the type of the eruption. By implementing a model for homologous eruptions, it shall be investigated the influence of imposed motions in the photospheric boundary and included an initial shear field, to produce different types of several eruptions.

Models of the eruptions, which are triggered by photospheric vortex motions, remain recently one of the foci of solar physics research since launching the Solar Dynamics Observatory (SDO) mission and its capability to observe such events. Photospheric vortex motions may also play a role to build free magnetic energy in the flux rope, leading to an eruption. Dhara et al (2014) examine ten erupting filaments from different eight active regions at different times during the solar cycle 24. In all of these events of filament eruptions, vortex motions have been observed before or during the initial fast rise phase. Such rotational motions could play the role in destabilizing the filament by building more axial flux into the erupting filament and subsequently increasing the outward pressure force Dhara et al. (2014). Furthermore, the photospheric vortex motions plays a role in transition magnetic twist between the solar interior and the corona Brown et al. (2003). Bi et al. (2017) analyze the vortex flows in active region 12371 during the flare eruption 2015 June 22. They suggest that such motions may be induced the expansion of the erupting flux rope as observed in SDO images Bi et al. (2017). Therefore, as one of the key arguments in this study is how a solar homologous eruption are triggered and driven, vortex motions aspect should be included in the future work. Imposed motions in the simulations as vortex motions at the footpoints of the flux rope should be investigated whether homologous eruptions can be produced when the configuration is driven by vortex motions where the reformed flux rope will be used as a new initial condition.

CHAPTER 7

Bibliography

Alexander, D., R. Liu, and H. R. Gilbert
2006. Hard X-Ray Production in a Failed Filament Eruption. *Astrophys. J.*, 653:719–724.

Amari, T., J.-J. Aly, Z. Mikic, and J. Linker
2010. Coronal Mass Ejection Initiation: On the Nature of the Flux Cancellation Model. *Astrophys. J. Letter*, 717:L26–L30.

Amari, T. and J. F. Luciani
1999. Confined Disruption of a Three-dimensional Twisted Magnetic Flux Tube. *Astrophys. J. Letter*, 515:L81–L84.

Amari, T., J. F. Luciani, J. J. Aly, Z. Mikic, and J. Linker
2003. Coronal Mass Ejection: Initiation, Magnetic Helicity, and Flux Ropes. I. Boundary Motion-driven Evolution. *Astrophys. J.*, 585:1073–1086.

Amari, T., J. F. Luciani, Z. Mikic, and J. Linker
1999. Three-dimensional Solutions of Magnetohydrodynamic Equationsfor Prominence Magnetic Support: Twisted Magnetic Flux Rope. *Astrophys. J. Letter*, 518:L57–L60.

Amari, T., J. F. Luciani, Z. Mikic, and J. Linker
2000. A Twisted Flux Rope Model for Coronal Mass Ejections and Two-Ribbon Flares. *Astrophys. J. Letter*, 529:L49–L52.

Antiochos, S. K.
1998. The Magnetic Topology of Solar Eruptions. *Astrophys. J. Letter*, 502:L181–L184.

Antiochos, S. K., C. R. DeVore, and J. A. Klimchuk
1999. A Model for Solar Coronal Mass Ejections. *Astrophys. J.*, 510:485–493.

Archontis, V., A. W. Hood, and K. Tsinganos
2014. Recurrent Explosive Eruptions and the "Sigmoid-to-arcade" Transformation in the Sun Driven by Dynamical Magnetic Flux Emergence. *Astrophys. J. Letter*, 786:L21.

Archontis, V. and T. Török
2008. Eruption of magnetic flux ropes during flux emergence. *Astron. & Astrophys. J.*, 492:L35–L38.

Aulanier, G., T. Török, P. Démoulin, and E. E. DeLuca
2010. Formation of Torus-Unstable Flux Ropes and Electric Currents in Erupting Sigmoids. *Astrophys. J.*, 708:314–333.

Bateman, G.
1978. *MHD instabilities*.

Bein, B. M., S. Berkebile-Stoiser, A. M. Veronig, M. Temmer, and B. Vršnak
2012. Impulsive Acceleration of Coronal Mass Ejections. II. Relation to Soft X-Ray Flares and Filament Eruptions. *Astrophys. J.*, 755:44.

Bi, Y., J. Yang, Y. Jiang, J. Hong, Z. Xu, Z. Qu, and K. Ji
2017. The Photospheric Vortex Flows during a Solar Flare. *Astrophys. J. Letter*, 849:L35.

Bobra, M. G., A. A. van Ballegooijen, and E. E. DeLuca
2008. Modeling Nonpotential Magnetic Fields in Solar Active Regions. *Astrophys. J.*, 672:1209–1220.

Brown, D. S., R. W. Nightingale, D. Alexander, C. J. Schrijver, T. R. Metcalf, R. A. Shine, A. M. Title, and C. J. Wolfson
2003. Observations of Rotating Sunspots from TRACE. *Solar. Phys.*, 216:79–108.

Brueckner, G. E., R. A. Howard, M. J. Koomen, C. M. Korendyke, D. J. Michels, J. D. Moses, D. G. Socker, K. P. Dere, P. L. Lamy, A. Llebaria, M. V. Bout, R. Schwenn, G. M. Simnett, D. K. Bedford, and C. J. Eyles
1995. The Large Angle Spectroscopic Coronagraph (LASCO). *Solar. Phys.*, 162:357–402.

Chandra, R., E. Pariat, B. Schmieder, C. H. Mandrini, and W. Uddin
2010. How Can a Negative Magnetic Helicity Active Region Generate a Positive Helicity Magnetic Cloud? *Solar. Phys.*, 261:127–148.

Chatterjee, P. and Y. Fan
2013. Simulation of Homologous and Cannibalistic Coronal Mass Ejections produced by the Emergence of a Twisted Flux Rope into the Solar Corona. *Astrophys. J. Letter*, 778:L8.

Chen, H., S. Ma, and J. Zhang
2013. Overlying Extreme-ultraviolet Arcades Preventing Eruption of a Filament Observed by AIA/SDO. *Astrophys. J.*, 778:70.

Chen, H., J. Zhang, S. Ma, S. Yang, L. Li, X. Huang, and J. Xiao
2015. Confined Flares in Solar Active Region 12192 from 2014 October 18 to 29. *Astrophys. J. Letter*, 808:L24.

Cheng, X., M. D. Ding, Y. Guo, J. Zhang, A. Vourlidas, Y. D. Liu, O. Olmedo, J. Q. Sun, and C. Li
2014. Tracking the Evolution of a Coherent Magnetic Flux Rope Continuously from the Inner to the Outer Corona. *Astrophys. J.*, 780:28.

Cheng, X., Q. Hao, M. D. Ding, K. Liu, P. F. Chen, C. Fang, and Y. D. Liu
2015. A Two-ribbon White-light Flare Associated with a Failed Solar Eruption Observed by ONSET, SDO, and IRIS. *Astrophys. J.*, 809:46.

Cheng, X., J. Zhang, M. D. Ding, Y. Guo, and J. T. Su
2011. A Comparative Study of Confined and Eruptive Flares in NOAA AR 10720. *Astrophys. J.*, 732:87.

Démoulin, P. and G. Aulanier
2010. Criteria for Flux Rope Eruption: Non-equilibrium Versus Torus Instability. *Astrophys. J.*, 718:1388–1399.

Deng, N., A. Tritschler, J. Jing, X. Chen, C. Liu, K. Reardon, C. Denker, Y. Xu, and H. Wang
2013. High-cadence and High-resolution Hα Imaging Spectroscopy of a Circular Flare's Remote Ribbon with IBIS. *Astrophys. J.*, 769:112.

Dere, K. P., G. E. Brueckner, R. A. Howard, D. J. Michels, and J. P. Delaboudiniere
1999. LASCO and EIT Observations of Helical Structure in Coronal Mass Ejections. *Astrophys. J.*, 516:465–474.

DeVore, C. R. and S. K. Antiochos
2000. Dynamical Formation and Stability of Helical Prominence Magnetic Fields. *Astrophys. J.*, 539:954–963.

DeVore, C. R. and S. K. Antiochos
2005. Magnetic Free Energies of Breakout Coronal Mass Ejections. *Astrophys. J.*, 628:1031–1045.

DeVore, C. R. and S. K. Antiochos
2008. Homologous Confined Filament Eruptions via Magnetic Breakout. *Astrophys. J.*, 680:740–756.

Dhara, S. K., B. Ravindra, and R. K. Banyal
2014. Observations of Photospheric Vortical Motions During the Early Stage of Filament Eruption. *Solar. Phys.*, 289:4481–4500.

Dulk, G. A. and D. J. McLean
1978. Coronal magnetic fields. *Solar. Phys.*, 57:279–295.

Einaudi, G. and G. van Hoven
1983. The stability of coronal loops - Finite-length and pressure-profile limits. *Solar. Phys.*, 88:163–177.

Fan, Y. and S. E. Gibson
2003. The Emergence of a Twisted Magnetic Flux Tube into a Preexisting Coronal Arcade. *Astrophys. J. Letter*, 589:L105–L108.

Fan, Y. and S. E. Gibson
2004. Numerical Simulations of Three-dimensional Coronal Magnetic Fields Resulting from the Emergence of Twisted Magnetic Flux Tubes. *Astrophys. J.*, 609:1123–1133.

Fan, Y. and S. E. Gibson
2007. Onset of Coronal Mass Ejections Due to Loss of Confinement of Coronal Flux Ropes. *Astrophys. J.*, 668:1232–1245.

Forbes, T. G.
2000. A review on the genesis of coronal mass ejections. *Journal of Geophysical Research*, 105:23153–23166.

Forbes, T. G. and P. A. Isenberg
1991. A catastrophe mechanism for coronal mass ejections. *Astrophys. J.*, 373:294–307.

Gaizauskas, V.
1993. The birth and evolution of solar active regions. *Advances in Space Research*, 13:5–14.

Gaizauskas, V., J. B. Zirker, C. Sweetland, and A. Kovacs
1997. Formation of a Solar Filament Channel. *Astrophys. J.*, 479:448.

Gary, G. A.
2001. Plasma Beta above a Solar Active Region: Rethinking the Paradigm. *Solar. Phys.*, 203:71–86.

Gerrard, C. L., T. D. Arber, A. W. Hood, and R. A. M. Van der Linden
2001. Numerical simulations of kink instability in line-tied coronal Loops. *Astron. & Astrophys. J.*, 373:1089–1098.

Gilbert, H. R., D. Alexander, and R. Liu
2007. Filament Kinking and Its Implications for Eruption and Re-formation. *Solar. Phys.*, 245:287–309.

Gopalswamy, N., M. Shimojo, W. Lu, S. Yashiro, K. Shibasaki, and R. A. Howard
2003. Prominence Eruptions and Coronal Mass Ejection: A Statistical Study Using Microwave Observations. *Astrophys. J.*, 586:562–578.

Gosling, J. T.
1993. Coronal mass ejections - The link between solar and geomagnetic activity. *Physics of Fluids B*, 5:2638–2645.

Green, L. M. and B. Kliem
2009. Flux Rope Formation Preceding Coronal Mass Ejection Onset. *Astrophys. J. Letter*, 700:L83–L87.

Green, L. M., B. Kliem, T. Török, L. van Driel-Gesztelyi, and G. D. R. Attrill
2007. Transient Coronal Sigmoids and Rotating Erupting Flux Ropes. *Solar. Phys.*, 246:365–391.

Green, L. M., B. Kliem, and A. J. Wallace
2011. Photospheric flux cancellation and associated flux rope formation and eruption. *Astron. & Astrophys. J.*, 526:A2.

Green, L. M., S. A. Matthews, L. van Driel-Gesztelyi, L. K. Harra, and J. L. Culhane
2002. Multi-wavelength observations of an X-class flare without a coronal mass ejection. *Solar. Phys.*, 205:325–339.

Guo, Y., M. D. Ding, X. Cheng, J. Zhao, and E. Pariat
2013. Twist Accumulation and Topology Structure of a Solar Magnetic Flux Rope. *Astrophys. J.*, 779:157.

Guo, Y., M. D. Ding, B. Schmieder, H. Li, T. Török, and T. Wiegelmann
2010. Driving Mechanism and Onset Condition of a Confined Eruption. *Astrophys. J. Letter*, 725:L38–L42.

Hanaoka, Y.
1997. Double-Loop Configuration of Solar Flares. *Solar. Phys.*, 173:319–346.

Handy, B. N., L. W. Acton, C. C. Kankelborg, C. J. Wolfson, D. J. Akin, M. E. Bruner, R. Caravalho, R. C. Catura, R. Chevalier, D. W. Duncan, C. G. Edwards, C. N. Feinstein, S. L. Freeland, F. M. Friedlaender, C. H. Hoffmann, N. E. Hurlburt, B. K. Jurcevich, N. L. Katz, G. A. Kelly, J. R. Lemen, M. Levay, R. W. Lindgren, D. P. Mathur, S. B. Meyer, S. J. Morrison, M. D. Morrison, R. W. Nightingale, T. P. Pope, R. A. Rehse, C. J. Schrijver, R. A. Shine, L. Shing, K. T. Strong, T. D. Tarbell, A. M. Title, D. D. Torgerson, L. Golub, J. A. Bookbinder, D. Caldwell, P. N. Cheimets, W. N. Davis, E. E. Deluca, R. A. McMullen, H. P. Warren, D. Amato, R. Fisher, H. Maldonado, and C. Parkinson
1999. The transition region and coronal explorer. *Solar. Phys.*, 187:229–260.

Hassanin, A. and B. Kliem
2016. Helical Kink Instability in a Confined Solar Eruption. *Astrophys. J.*, 832:106.

Hassanin, A., B. Kliem, and N. Seehafer
2016. Helical kink instability in the confined solar eruption on 2002 May 27. *Astronomische Nachrichten*, 337:1082.

Hood, A. W. and E. R. Priest
1981. Critical conditions for magnetic instabilities in force-free coronal loops. *Geophysical & Astrophysical Fluid Dynamics*, 17:297–318.

Hori, K. and J. L. Culhane
2002. Trajectories of microwave prominence eruptions. *Astron. & Astrophys. J.*, 382:666–677.

Houdek, G. and D. O. Gough
2011. On the seismic age and heavy-element abundance of the Sun. *Mon. Not. R. Astron. Soc.*, 418:1217–1230.

House, L. L., W. J. Wagner, E. Hildner, C. Sawyer, and H. U. Schmidt
1981. Studies of the corona with the Solar Maximum Mission coronagraph/polarimeter. *Astrophys. J. Letter*, 244:L117–L121.

Howe, R.
2009. Solar Interior Rotation and its Variation. *Living Reviews in Solar Physics*, 6:1.

Hsu, S. C. and P. M. Bellan
2005. On the jets, kinks, and spheromaks formed by a planar magnetized coaxial gun. *Physics of Plasmas*, 12(3):032103.

Illing, R. M. E. and A. J. Hundhausen
1985. Observation of a coronal transient from 1.2 to 6 solar radii. *Journal of Geophysical Research*, 90:275–282.

Innes, D. E., D. E. McKenzie, and T. Wang
2003. Observations of 1000 km s^{-1} Doppler shifts in 10^7 K solar flare supra-arcade. *Solar. Phys.*, 217:267–279.

Inoue, S., K. Hayashi, and K. Kusano
2016. Structure and Stability of Magnetic Fields in Solar Active Region 12192 Based on the Nonlinear Force-free Field Modeling. *Astrophys. J.*, 818:168.

Inoue, S. and K. Kusano
2006. Three-dimensional Simulation Study of Flux Rope Dynamics in the Solar Corona. *Astrophys. J.*, 645:742–756.

Isenberg, P. A. and T. G. Forbes
2007. A Three-dimensional Line-tied Magnetic Field Model for Solar Eruptions. *Astrophys. J.*, 670:1453–1466.

Janvier, M., G. Aulanier, V. Bommier, B. Schmieder, P. Démoulin, and E. Pariat
2014. Electric Currents in Flare Ribbons: Observations and Three-dimensional Standard Model. *Astrophys. J.*, 788:60.

Ji, H., H. Wang, E. J. Schmahl, Y.-J. Moon, and Y. Jiang
2003. Observations of the Failed Eruption of a Filament. *Astrophys. J. Letter*, 595:L135–L138.

Jiang, C., S. T. Wu, X. Feng, and Q. Hu
2014a. Formation and Eruption of an Active Region Sigmoid. I. A Study by Nonlinear Force-free Field Modeling. *Astrophys. J.*, 780:55.

Jiang, Y., J. Hong, J. Yang, Y. Bi, R. Zheng, B. Yang, H. Li, and D. Yang
2013. Partial Slingshot Reconnection between Two Filaments. *Astrophys. J.*, 764:68.

Jiang, Y., J. Yang, H. Wang, H. Ji, Y. Liu, H. Li, and J. Li
2014b. Interaction and Merging of two Sinistral Filaments. *Astrophys. J.*, 793:14.

Jing, J., Y. Xu, J. Lee, N. V. Nitta, C. Liu, S.-H. Park, T. Wiegelmann, and H. Wang
2015. Comparison between the eruptive X2.2 flare on 2011 February 15 and confined X3.1 flare on 2014 October 24. *Research in Astro. & Astrophy.*, 15:1537.

Jing, J., V. B. Yurchyshyn, G. Yang, Y. Xu, and H. Wang
2004. On the Relation between Filament Eruptions, Flares, and Coronal Mass Ejections. *Astrophys. J.*, 614:1054–1062.

Joshi, N. C., C. Liu, X. Sun, H. Wang, T. Magara, and Y.-J. Moon
2015. The Role of Erupting Sigmoid in Triggering a Flare with Parallel and Large-scale Quasi-circular Ribbons. *Astrophys. J.*, 812:50.

Joshi, N. C., T. Magara, and S. Inoue
2014a. Formation of a Compound Flux Rope by the Merging of Two Filament Channels, the Associated Dynamics, and its Stability. *Astrophys. J.*, 795:4.

Joshi, N. C., A. K. Srivastava, B. Filippov, P. Kayshap, W. Uddin, R. Chandra, D. Prasad Choudhary, and B. N. Dwivedi
2014b. Confined Partial Filament Eruption and its Reformation within a Stable Magnetic Flux Rope. *Astrophys. J.*, 787:11.

Karlický, M. and B. Kliem
2010. Reconnection of a Kinking Flux Rope Triggering the Ejection of a Microwave and Hard X-ray Source I. Observations and Interpretation. *Solar. Phys.*, 266:71–89.

Karpen, J. T., S. K. Antiochos, and C. R. DeVore
2012. The Mechanisms for the Onset and Explosive Eruption of Coronal Mass Ejections and Eruptive Flares. *Astrophys. J.*, 760:81.

Kippenhahn, R. and A. Schlüter
1957. Eine Theorie der solaren Filamente. Mit 7 Textabbildungen. *Zeitschrift für Astrophysik*, 43:36.

Kliem, B., J. Lin, T. G. Forbes, E. R. Priest, and T. Török
2014. Catastrophe versus Instability for the Eruption of a Toroidal Solar Magnetic Flux Rope. *Astrophys. J.*, 789:46.

Kliem, B., M. G. Linton, T. Török, and M. Karlický
2010. Reconnection of a Kinking Flux Rope Triggering the Ejection of a Microwave and Hard X-Ray Source II. Numerical Modeling. *Solar. Phys.*, 266:91–107.

Kliem, B. and T. Török
2006. Torus Instability. *Physical Review Letters*, 96(25):255002.

Kliem, B., T. Török, and W. T. Thompson
2012. A Parametric Study of Erupting Flux Rope Rotation. Modeling the "Cartwheel CME" on 9 April 2008. *Solar. Phys.*, 281:137–166.

Koleva, K., M. S. Madjarska, P. Duchlev, C. J. Schrijver, J.-C. Vial, E. Buchlin, and M. Dechev
2012. Kinematics and helicity evolution of a loop-like eruptive prominence. *Astron. & Astrophys. J.*, 540:A127.

Kumar, P. and K.-S. Cho
2014. Multiwavelength observation of a large-scale flux rope eruption above a kinked small filament. *Astron. & Astrophys. J.*, 572:A83.

Kumar, P., V. M. Nakariakov, and K.-S. Cho
2015. X-Ray and EUV Observations of Simultaneous Short and Long Period Oscillations in Hot Coronal Arcade Loops. *Astrophys. J.*, 804:4.

Kuperus, M. and M. A. Raadu
1974. The Support of Prominences Formed in Neutral Sheets. *Astron. & Astrophys. J.*, 31:189.

Kuridze, D., M. Mathioudakis, A. F. Kowalski, P. H. Keys, D. B. Jess, K. S. Balasubramaniam, and F. P. Keenan
2013. Failed filament eruption inside a coronal mass ejection in active region 11121. *Astron. & Astrophys. J.*, 552:A55.

Kushwaha, U., B. Joshi, K.-S. Cho, A. Veronig, S. K. Tiwari, and S. K. Mathew
2014. Impulsive Energy Release and Non-thermal Emission in a Confined M4.0 Flare Triggered by Rapidly Evolving Magnetic Structures. *Astrophys. J.*, 791:23.

Kushwaha, U., B. Joshi, A. M. Veronig, and Y.-J. Moon
2015. Large-scale Contraction and Subsequent Disruption of Coronal Loops During Various Phases of the M6.2 Flare Associated with the Confined Flux Rope Eruption. *Astrophys. J.*, 807:101.

Li, T. and J. Zhang
2015. High-Resolution Observations of a Flux Rope with the Interface Region Imaging Spectrograph. *Solar. Phys.*, 290:2857–2870.

Lin, J. and T. G. Forbes
2000. Effects of reconnection on the coronal mass ejection process. *Journal of Geophysical Research*, 105:2375–2392.

Lin, R. P., B. R. Dennis, G. J. Hurford, D. M. Smith, A. Zehnder, P. R. Harvey, D. W. Curtis, D. Pankow, P. Turin, M. Bester, A. Csillaghy, M. Lewis, N. Madden, H. F. van Beek, M. Appleby, T. Raudorf, J. McTiernan, R. Ramaty, E. Schmahl, R. Schwartz, S. Krucker, R. Abiad, T. Quinn, P. Berg, M. Hashii, R. Sterling, R. Jackson, R. Pratt, R. D. Campbell, D. Malone, D. Landis, C. P. Barrington-Leigh, S. Slassi-Sennou, C. Cork, D. Clark, D. Amato, L. Orwig, R. Boyle, I. S. Banks, K. Shirey, A. K. Tolbert, D. Zarro, F. Snow, K. Thomsen, R. Henneck, A. McHedlishvili, P. Ming, M. Fivian, J. Jordan, R. Wanner, J. Crubb, J. Preble, M. Matranga, A. Benz, H. Hudson, R. C. Canfield, G. D. Holman, C. Crannell, T. Kosugi, A. G. Emslie, N. Vilmer, J. C. Brown, C. Johns-Krull, M. Aschwanden, T. Metcalf, and A. Conway
2002. The Reuven Ramaty High-Energy Solar Spectroscopic Imager (RHESSI). *Solar. Phys.*, 210:3–32.

Linker, J. A., R. Lionello, Z. Mikić, and T. Amari
2001. Magnetohydrodynamic modeling of prominence formation within a helmet streamer. *Journal of Geophysical Research*, 106:25165–25176.

Lionello, R., Z. Mikić, J. A. Linker, and T. Amari
2002. Magnetic Field Topology in Prominences. *Astrophys. J.*, 581:718–725.

Lites, B. W., B. C. Low, V. Martinez Pillet, P. Seagraves, A. Skumanich, Z. A. Frank, R. A. Shine, and S. Tsuneta
1995. The Possible Ascent of a Closed Magnetic System through the Photosphere. *Astrophys. J.*, 446:877.

Litvinenko, Y. E. and S. F. Martin
1999. Magnetic reconnection as the cause of a photospheric canceling feature and mass flows in a filament. *Solar. Phys.*, 190:45–58.

Liu, C., N. Deng, R. Liu, J. Lee, É. Pariat, T. Wiegelmann, Y. Liu, L. Kleint, and H. Wang
2015. A Circular-ribbon Solar Flare Following an Asymmetric Filament Eruption. *Astrophys. J. Letter*, 812:L19.

Liu, K., Y. Wang, C. Shen, and S. Wang
2012. Critical Height for the Destabilization of Solar Prominences: Statistical Results from STEREO Observations. *Astrophys. J.*, 744:168.

Liu, L., Y. Wang, J. Wang, C. Shen, P. Ye, R. Liu, J. Chen, Q. Zhang, and S. Wang
2016a. Why is a Flare-rich Active Region CME-poor? *Astrophys. J.*, 826:119.

Liu, L., Y. Wang, J. Wang, C. Shen, P. Ye, R. Liu, J. Chen, Q. Zhang, and S. Wang
2016b. Why is a Flare-rich Active Region CME-poor? *Astrophys. J.*, 826:119.

Liu, R. and D. Alexander
2009. Hard X-ray Emission in Kinking Filaments. *Astrophys. J.*, 697:999–1009.

Liu, R., D. Alexander, and H. R. Gilbert
2007. Kink-induced Catastrophe in a Coronal Eruption. *Astrophys. J.*, 661:1260–1271.

Liu, R., B. Kliem, V. S. Titov, J. Chen, Y. Wang, H. Wang, C. Liu, Y. Xu, and T. Wiegelmann
2016c. Structure, Stability, and Evolution of Magnetic Flux Ropes from the Perspective of Magnetic Twist. *Astrophys. J.*, 818:148.

Liu, R., C. Liu, S. Wang, N. Deng, and H. Wang
2010. Sigmoid-to-flux-rope Transition Leading to a Loop-like Coronal Mass Ejection. *Astrophys. J. Letter*, 725:L84–L90.

Liu, R., V. S. Titov, T. Gou, Y. Wang, K. Liu, and H. Wang
2014. An Unorthodox X-Class Long-duration Confined Flare. *Astrophys. J.*, 790:8.

Liu, Y., J. Su, Z. Xu, H. Lin, K. Shibata, and H. Kurokawa
2009. New Observation of Failed Filament Eruptions: The Influence of Asymmetric Coronal Background Fields on Solar Eruptions. *Astrophys. J. Letter*, 696:L70–L73.

Livi, S. H. B., J. Wang, and S. F. Martin
1985. The cancellation of magnetic flux. I - On the quiet sun. *Australian Journal of Physics*, 38:855–873.

Low, B. C.
1996. Solar Activity and the Corona. *Solar. Phys.*, 167:217–265.

Low, B. C. and J. R. Hundhausen
1995. Magnetostatic structures of the solar corona. 2: The magnetic topology of quiescent prominences. *Astrophys. J.*, 443:818–836.

Lynch, B. J., S. K. Antiochos, P. J. MacNeice, T. H. Zurbuchen, and L. A. Fisk
2004. Observable Properties of the Breakout Model for Coronal Mass Ejections. *Astrophys. J.*, 617:589–599.

Mackay, D. H., E. R. Priest, V. Gaizauskas, and A. A. van Ballegooijen
1998. Role of Helicity in the Formation of Intermediate Filaments. *Solar. Phys.*, 180:299–312.

Mackay, D. H. and A. A. van Ballegooijen
2006. Models of the Large-Scale Corona. I. Formation, Evolution, and Liftoff of Magnetic Flux Ropes. *Astrophys. J.*, 641:577–589.

Mackay, D. H. and A. A. van Ballegooijen
2009. A Non-Linear Force-Free Field Model for the Evolving Magnetic Structure of Solar Filaments. *Solar. Phys.*, 260:321–346.

MacNeice, P., S. K. Antiochos, A. Phillips, D. S. Spicer, C. R. DeVore, and K. Olson
2004. A Numerical Study of the Breakout Model for Coronal Mass Ejection Initiation. *Astrophys. J.*, 614:1028–1041.

MacTaggart, D. and A. W. Hood
2009. Multiple eruptions from magnetic flux emergence. *Astron. & Astrophys. J.*, 508:445–449.

Manchester, IV, W., T. Gombosi, D. DeZeeuw, and Y. Fan
2004. Eruption of a Buoyantly Emerging Magnetic Flux Rope. *Astrophys. J.*, 610:588–596.

Martens, P. C. and C. Zwaan
2001. Origin and Evolution of Filament-Prominence Systems. *Astrophys. J.*, 558:872–887.

Martin, S. F.
1998. Conditions for the Formation and Maintenance of Filaments (Invited Review). *Solar. Phys.*, 182:107–137.

Martin, S. F., S. H. B. Livi, and J. Wang
1985. The cancellation of magnetic flux. II - In a decaying active region. *Australian Journal of Physics*, 38:929–959.

Masson, S., E. Pariat, G. Aulanier, and C. J. Schrijver
2009. The Nature of Flare Ribbons in Coronal Null-Point Topology. *Astrophys. J.*, 700:559–578.

Moore, R. L. and B. J. Labonte
1980. The filament eruption in the 3B flare of July 29, 1973 - Onset and magnetic field configuration. In *Solar and Interplanetary Dynamics*, M. Dryer and E. Tandberg-Hanssen, eds., volume 91 of *IAU Symposium*, Pp. 207–210.

Moore, R. L., A. C. Sterling, H. S. Hudson, and J. R. Lemen
2001. Onset of the Magnetic Explosion in Solar Flares and Coronal Mass Ejections. *Astrophys. J.*, 552:833–848.

Mullan, D. J.
2010. *Physics of the Sun: A First Course*.

Myers, C. E., M. Yamada, H. Ji, J. Yoo, W. Fox, J. Jara-Almonte, A. Savcheva, and E. E. Deluca
2015. A dynamic magnetic tension force as the cause of failed solar eruptions. *Nature*, 528:526–529.

Netzel, A., T. Mrozek, S. Kołomański, and S. Gburek
2012. Extreme-ultraviolet and hard X-ray signatures of electron acceleration during the failed eruption of a filament. *Astron. & Astrophys. J.*, 548:A89.

Nishio, M., K. Yaji, T. Kosugi, H. Nakajima, and T. Sakurai
1997. Magnetic Field Configuration in Impulsive Solar Flares Inferred from Coaligned Microwave/X-Ray Images. *Astrophys. J.*, 489:976–991.

Ouyang, Y., K. Yang, and P. F. Chen
2015. Is Flux Rope a Necessary Condition for the Progenitor of Coronal Mass Ejections? *Astrophys. J.*, 815:72.

Panesar, N. K., A. C. Sterling, D. E. Innes, and R. L. Moore
2015. Destabilization of a Solar Prominence/Filament Field System by a Series of Eight Homologous Eruptive Flares Leading to a CME. *Astrophys. J.*, 811:5.

Panesar, N. K., A. C. Sterling, and R. L. Moore
2017. Magnetic Flux Cancellation as the Origin of Solar Quiet-region Pre-jet Minifilaments. *Astrophys. J.*, 844:131.

Panesar, N. K., A. C. Sterling, R. L. Moore, and P. Chakrapani
2016. Magnetic Flux Cancelation as the Trigger of Solar Quiet-region Coronal Jets. *Astrophys. J. Letter*, 832:L7.

Pneuman, G. W.
1983. The formation of solar prominences by magnetic reconnection and condensation. *Solar. Phys.*, 88:219–239.

Priest, E. R.
1984. *Solar magneto-hydrodynamics*.

Qiu, J., Q. Hu, T. A. Howard, and V. B. Yurchyshyn
2007. On the Magnetic Flux Budget in Low-Corona Magnetic Reconnection and Interplanetary Coronal Mass Ejections. *Astrophys. J.*, 659:758–772.

Qiu, J., H. Wang, C. Z. Cheng, and D. E. Gary
2004. Magnetic Reconnection and Mass Acceleration in Flare-Coronal Mass Ejection Events. *Astrophys. J.*, 604:900–905.

Régnier, S., E. R. Priest, and A. W. Hood
2008. Coronal Alfvén speeds in an isothermal atmosphere. I. Global properties. *Astron. & Astrophys. J.*, 491:297–309.

Richtmyer, R. D. and K. W. Morton
1967. *Difference methods for initial-value problems.*

Romano, P., L. Contarino, and F. Zuccarello
2003. Eruption of a helically twisted prominence. *Solar. Phys.*, 214:313–323.

Romano, P., F. P. Zuccarello, S. L. Guglielmino, and F. Zuccarello
2014. Evolution of the Magnetic Helicity Flux during the Formation and Eruption of Flux Ropes. *Astrophys. J.*, 794:118.

Roussev, I. I., T. G. Forbes, T. I. Gombosi, I. V. Sokolov, D. L. DeZeeuw, and J. Birn
2003. A Three-dimensional Flux Rope Model for Coronal Mass Ejections Based on a Loss of Equilibrium. *Astrophys. J. Letter*, 588:L45–L48.

Rust, D. M. and A. Kumar
1994. Helical magnetic fields in filaments. *Solar. Phys.*, 155:69–97.

Sato, T. and T. Hayashi
1979. Externally driven magnetic reconnection and a powerful magnetic energy converter. *Physics of Fluids*, 22:1189–1202.

Savcheva, A. S., L. M. Green, A. A. van Ballegooijen, and E. E. DeLuca
2012. Photospheric Flux Cancellation and the Build-up of Sigmoidal Flux Ropes on the Sun. *Astrophys. J.*, 759:105.

Scherrer, P. H., R. S. Bogart, R. I. Bush, J. T. Hoeksema, A. G. Kosovichev, J. Schou, W. Rosenberg, L. Springer, T. D. Tarbell, A. Title, C. J. Wolfson, I. Zayer, and MDI Engineering Team
1995. The Solar Oscillations Investigation - Michelson Doppler Imager. *Solar. Phys.*, 162:129–188.

Shafranov, V. D.
1966. Plasma Equilibrium in a Magnetic Field. *Rev. Plasma Phys.*, 2:103–+.

Shen, Y., Y. Liu, and J. Su
2012. Sympathetic Partial and Full Filament Eruptions Observed in One Solar Breakout Event. *Astrophys. J.*, 750:12.

Shen, Y.-D., Y. Liu, and R. Liu
2011. A time series of filament eruptions observed by three eyes from space: from failed to successful eruptions. *Research in Astro. & Astrophy.*, 11:594–606.

Soenen, A., F. P. Zuccarello, C. Jacobs, S. Poedts, R. Keppens, and B. van der Holst
2009. Numerical simulations of homologous coronal mass ejections in the solar wind. *Astron. & Astrophys. J.*, 501:1123–1130.

Song, H. Q., J. Zhang, X. Cheng, Y. Chen, R. Liu, Y. M. Wang, and B. Li
2014. Temperature Evolution of a Magnetic Flux Rope in a Failed Solar Eruption. *Astrophys. J.*, 784:48.

Sterling, A. C. and R. L. Moore
2005. Slow-Rise and Fast-Rise Phases of an Erupting Solar Filament, and Flare Emission Onset. *Astrophys. J.*, 630:1148–1159.

Sterling, A. C., R. L. Moore, D. A. Falconer, and M. Adams
2015. Small-scale filament eruptions as the driver of X-ray jets in solar coronal holes. *Nature*, 523:437–440.

Stix, M.
2002. *The Sun: An Introduction.*

Sturrock, P. A., M. Weber, M. S. Wheatland, and R. Wolfson
2001. Metastable Magnetic Configurations and Their Significance for Solar Eruptive Events. *Astrophys. J.*, 548:492–496.

Subramanian, P. and K. P. Dere
2001. Source Regions of Coronal Mass Ejections. *Astrophys. J.*, 561:372–395.

Sun, X., M. G. Bobra, J. T. Hoeksema, Y. Liu, Y. Li, C. Shen, S. Couvidat, A. A. Norton, and G. H. Fisher
2015. Why Is the Great Solar Active Region 12192 Flare-rich but CME-poor? *Astrophys. J. Letter*, 804:L28.

Sun, X., J. T. Hoeksema, Y. Liu, G. Aulanier, Y. Su, I. G. Hannah, and R. A. Hock
2013. Hot Spine Loops and the Nature of a Late-phase Solar Flare. *Astrophys. J.*, 778:139.

Syrovatskii, S. I.
1982. Model for flare loops, fast motions, and opening of magnetic field in the corona. *Solar. Phys.*, 76:3–20.

Thalmann, J. K., Y. Su, M. Temmer, and A. M. Veronig
2015. The Confined X-class Flares of Solar Active Region 2192. *Astrophys. J. Letter*, 801:L23.

Titov, V. S. and P. Démoulin
1999. Basic topology of twisted magnetic configurations in solar flares. *Astron. & Astrophys. J.*, 351:707–720.

Titov, V. S., E. R. Priest, and P. Demoulin
1993. Conditions for the appearance of "bald patches" at the solar surface. *Astron. & Astrophys. J.*, 276:564.

Török, T., M. A. Berger, and B. Kliem
2010. The writhe of helical structures in the solar corona. *Astron. & Astrophys. J.*, 516:A49.

Török, T., R. Chandra, E. Pariat, P. Démoulin, B. Schmieder, G. Aulanier, M. G. Linton, and C. H. Mandrini
2011a. Filament Interaction Modeled by Flux Rope Reconnection. *Astrophys. J.*, 728:65.

Török, T. and B. Kliem
2003. The evolution of twisting coronal magnetic flux tubes. *Astron. & Astrophys. J.*, 406:1043–1059.

Török, T. and B. Kliem
2005. Confined and Ejective Eruptions of Kink-unstable Flux Ropes. *Astrophys. J.*, 630:L97–L100.

Török, T. and B. Kliem
2007. Numerical simulations of fast and slow coronal mass ejections. *Astronomische Nachrichten*, 328:743.

Török, T., B. Kliem, and V. S. Titov
2004. Ideal kink instability of a magnetic loop equilibrium. *Astron. & Astrophys. J.*, 413:L27–L30.

Török, T., O. Panasenco, V. S. Titov, Z. Mikić, K. K. Reeves, M. Velli, J. A. Linker, and G. De Toma
2011b. A Model for Magnetically Coupled Sympathetic Eruptions. *Astrophys. J. Letter*, 739:L63.

Ugai, M. and T. Tsuda
1977. Magnetic field-line reconnexion by localized enhancement of resistivity. I - Evolution in a compressible MHD fluid. *Journal of Plasma Physics*, 17:337–356.

van Ballegooijen, A. A. and P. C. H. Martens
1989a. Formation and eruption of solar prominences. *Astrophys. J.*, 343:971–984.

van Ballegooijen, A. A. and P. C. H. Martens
1989b. Formation and eruption of solar prominences. *Astrophys. J.*, 343:971–984.

van Ballegooijen, A. A. and P. C. H. Martens
1990. Magnetic fields in quiescent prominences. *Astrophys. J.*, 361:283–289.

van Ballegooijen, A. A., E. R. Priest, and D. H. Mackay
2000. Mean Field Model for the Formation of Filament Channels on the Sun. *Astrophys. J.*, 539:983–994.

van der Linden, R. A. M. and A. W. Hood
1999. A complete coronal loop stability analysis in ideal magnetohydrodynamics. II. Force-free cylindrical equilibria. *Astron. & Astrophys. J.*, 346:303–312.

van Tend, W. and M. Kuperus
1978. The development of coronal electric current systems in active regions and their relation to filaments and flares. *Solar. Phys.*, 59:115–127.

Vemareddy, P. and T. Wiegelmann
2014. Quasi-static Three-dimensional Magnetic Field Evolution in Solar Active Region NOAA 11166 Associated with an X1.5 Flare. *Astrophys. J.*, 792:40.

Vršnak, B.
2008. Processes and mechanisms governing the initiation and propagation of CMEs. *Annales Geophysicae*, 26:3089–3101.

Vršnak, B., J. Magdalenić, H. Aurass, and G. Mann
2002. Band-splitting of coronal and interplanetary type II bursts. II. Coronal magnetic field and Alfvén velocity. *Astron. & Astrophys. J.*, 396:673–682.

Wang, D., R. Liu, Y. Wang, K. Liu, J. Chen, J. Liu, Z. Zhou, and M. Zhang
2017. Critical Height of the Torus Instability in Two-ribbon Solar Flares. *Astrophys. J. Letter*, 843:L9.

Wang, H. and C. Liu
2012. Circular Ribbon Flares and Homologous Jets. *Astrophys. J.*, 760:101.

Wang, R., Y. D. Liu, I. Zimovets, H. Hu, X. Dai, and Z. Yang
2016. Sympathetic Solar Filament Eruptions. *Astrophys. J. Letter*, 827:L12.

Wang, T., L. Sui, and J. Qiu
2007. Direct Observation of High-Speed Plasma Outflows Produced by Magnetic Reconnection in Solar Impulsive Events. *Astrophys. J. Letter*, 661:L207–L210.

Wang, Y. and J. Zhang
2007. A Comparative Study between Eruptive X-Class Flares Associated with Coronal Mass Ejections and Confined X-Class Flares. *Astrophys. J.*, 665:1428–1438.

Webb, D. F., E. W. Cliver, N. U. Crooker, O. C. S. Cry, and B. J. Thompson
2000. Relationship of halo coronal mass ejections, magnetic clouds, and magnetic storms. *Journal of Geophysical Research*, 105:7491–7508.

Xue, Z., X. Yan, L. Zhao, Y. Xiang, L. Yang, and Y. Guo
2016. Failed eruptions of two intertwining small-scale filaments. *Publications of the Astronomical Society of Japan*, 68:7.

Yang, S., J. Zhang, and Y. Xiang
2014. Fine Structures and Overlying Loops of Confined Solar Flares. *Astrophys. J. Letter*, 793:L28.

Yardley, S. L., L. M. Green, D. R. Williams, L. van Driel-Gesztelyi, G. Valori, and S. Dacie
2016. Flux Cancellation and the Evolution of the Eruptive Filament of 2011 June 7. *Astrophys. J.*, 827:151.

Zhang, J. and K. P. Dere
2006. A Statistical Study of Main and Residual Accelerations of Coronal Mass Ejections. *Astrophys. J.*, 649:1100–1109.

Zuccarello, F. P., G. Aulanier, and S. A. Gilchrist
2015. Critical Decay Index at the Onset of Solar Eruptions. *Astrophys. J.*, 814:126.

Zuccarello, F. P., G. Aulanier, and S. A. Gilchrist
2016. The Apparent Critical Decay Index at the Onset of Solar Prominence Eruptions. *Astrophys. J. Letter*, 821:L23.

Zwaan, C.
1987. Elements and patterns in the solar magnetic field. *Ann. Rev. Astron. Astrophys.*, 25:83–111.

Zwaan, C.
1996. A Dynamo Scenario|Observational Constraints on Dynamo Theory. *Solar. Phys.*, 169:265–276.